

USDAO TECHNICAL LIBRARY



5 0712 01016543 8

# Program to Investigate Advanced Laser Processing of Materials

AD A100 302

E.M. Breinan  
D.B. Snow  
C.O. Brown

TECHNICAL  
LIBRARY

## Final Report

**Summary of Work Performed:**  
**1 June 1978 — 30 November 1980**

**January 1981**

**Prepared under Contract N00014-78-C-0387**

Approved for internal agency use and sale; its  
distribution is unlimited.

**Sponsored by**

**Defense Advanced Research Projects Agency  
ARPA Order No.3542**

**Prepared for**

**Office of Naval Research**



**UNITED  
TECHNOLOGIES  
RESEARCH  
CENTER**

East Hartford, Connecticut 06108

JUN 17 1981

A

The views and conclusions contained in this document are those of the authors and should not be interpreted as necessarily representing the official policies, either expressed or implied, of the Defense Advanced Research Projects Agency or the U.S. Government.

Reproduction in whole or in part is permitted for any purpose of the United States Government.

815 18 088

**UNCLASSIFIED**

SECURITY CLASSIFICATION OF THIS PAGE (When Data Entered)

DD FORM 1473 EDITION OF 1 NOV 65 IS OBSOLETE  
1 JAN 73

UNCLASSIFIED

SECURITY CLASSIFICATION OF THIS PAGE (When Data Entered)

UNCLASSIFIED

SECURITY CLASSIFICATION OF THIS PAGE(When Data Entered)

#19. Cont'd

Electron Microscopy  
Microstructural Characterization  
Strengthening Mechanisms

#20 Cont'd

sizable or serious fabrication flaws provided that the alloy has adequate "weldability" at high cooling rates.

In a second major area, design of a LAYERGLAZE-processable superalloy was undertaken. Within the system Ni-Al-Mo + X, numerous processable compositions were found, however, these compositions were characterized by embrittling phase transformations in the 600-800°C temperature range. The research efforts in the alloy design area aimed at understanding and controlling this instability produced several alloys in the Ni-Al-Mo + X family which appeared to demonstrate the necessary characteristics of processability and phase stability. The mechanical properties of these alloys are being evaluated under an additional program. In addition to alloys from the above system, a number of additional alloys with high strength potentials have been developed based on other systems. The strengthening mechanism of the Ni-Al-Mo + X family of LAYERGLAZE processable alloys involves fine  $\gamma'$  precipitates and a very fine dispersion of metastable D0<sub>22</sub> structure Ni<sub>3</sub>Mo or D1<sub>a</sub> structure Ni<sub>4</sub>Mo particles.

UNCLASSIFIED

SECURITY CLASSIFICATION OF THIS PAGE(When Data Entered)

UNITED TECHNOLOGIES CORPORATION  
RESEARCH CENTER  
East Hartford, Connecticut

R81-914346-8

FINAL REPORT  
Contract N00014-78-C-0387  
Summary of Work Performed for the Period  
1 June 1978 - 30 November 1980

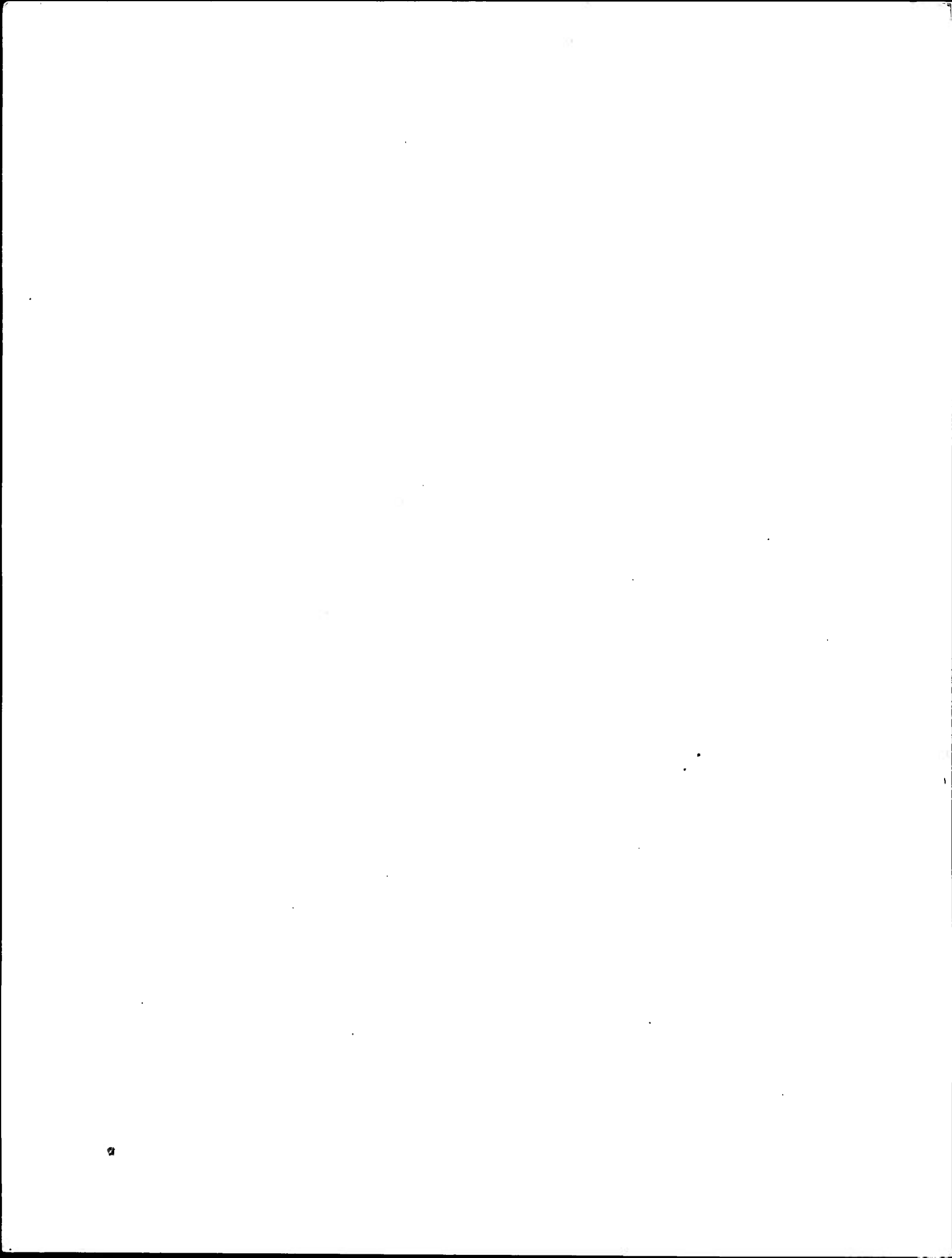
ARPA Order No:	3542
Program Code No.:	000008D10K71
Contractor:	United Technologies Research Center
Contract Date:	1 June 1978
Contract Amount:	\$740,000
Contract No.	N00014-78-C-0387
Contract Expiration Date:	29 January 1981
Short Title of Work:	Laser Materials Processing
Principal Investigator:	Dr. E. M. Breinan (203) 727-7396
Scientific Officer:	Dr. Bruce A. MacDonald
Reported by:	E. M. Breinan, C. O. Brown, D.B. Snow

Sponsored by Defense Advanced Research Projects Agency

Program to Investigate Advanced Laser  
Processing of Materials

TABLE OF CONTENTS

SUMMARY . . . . .	1
INTRODUCTION AND BACKGROUND . . . . .	3
A. Major Conclusions . . . . .	4
B. Additional Results and Conclusions . . . . .	5
EXPERIMENTAL PROCESSING OF LAYERGLAZED MATERIALS . . . . .	9
A. Apparatus . . . . .	9
B. Determination of Process Criticality . . . . .	10
C. Wire Feed Development . . . . .	11
D. Powder Feed Development . . . . .	13
E. Fabrication of Samples for Mechanical Test . . . . .	15
F. Fabrication of Full Size Disk Preform . . . . .	16
ALLOY DEVELOPMENT FOR LAYERGLAZE FABRICATION . . . . .	18
A. Introduction . . . . .	18
B. Experimental Procedure . . . . .	18
C. Results . . . . .	20
DISCUSSION . . . . .	32
A. Cracking During Laser Processing . . . . .	32
RESULTS AND CONCLUSIONS . . . . .	33
A. Processing . . . . .	33
B. Alloy Design and Development . . . . .	34
C. Spin Test Design . . . . .	36
REFERENCES . . . . .	37
TABLES I - XI . . . . .	41
FIGURES 1 - 86	
APPENDIX A and B	



Program to Investigate Advanced Laser Processing of Materials

SUMMARY

During the course of this program to produce and spin test a 12.7 cm diameter turbine disk using the LAYERGLAZE™ process, major accomplishments have been recorded in both the processing and alloy-design areas. In the processing area, following preliminary experiments utilizing metal tapes as feedstock, along with a series of experiments using wire feedstock, a final LAYERGLAZE apparatus utilizing a powder feed was developed and used to produce LAYERGLAZE parts for mechanical test. In addition, a 13.2 cm diameter, 3 cm thick scale model disk preform was produced in order to demonstrate the capability of the LAYERGLAZE apparatus constructed as part of this program to produce actual parts of that size. Mechanical testing and microstructural analysis of LAYERGLAZED material produced within the scope of this program has indicated that LAYERGLAZED parts possess good structural integrity, and that there are no serious or sizable fabrication flaws inherent in the process, provided that the alloys deposited have adequate "weldability" at intermediate to high cooling rates. Although the process, as evaluated, appeared to be capable of producing test disks which would be of sufficient quality for meaningful spin testing, the spin test was not conducted due to a change in program emphasis.

In the alloy design area, initial program efforts were directed toward the development of a superalloy which possessed sufficient weldability so as to be LAYERGLAZE processable. Numerous such compositions were found within the general system Ni-Al-Mo + X; however, it was soon discovered that such alloys often exhibited embrittling cellular phase transformations when annealed at 600-800°C for  $\geq 30$  hrs. Considerable effort was expended both in order to understand and control this instability. Within the program were developed a series of Ni-Al-Mo + X alloys which, by the program's end, appeared to demonstrate the necessary characteristics of processability and phase stability. The mechanical properties of these alloys are being characterized in detail in a follow-on program under NASC sponsorship. In addition to alloys in the original Ni-Al-Mo + X family, a significant number of additional alloy candidates with high strength potentials have been evolved, some as major modifications of state-of-the-art superalloys. Through this procedure, a number of general rules for making LAYERGLAZE-processable alloys have been evolved.

The strengthening mechanism of the Ni-Al-Mo + X family of LAYERGLAZE processed alloys has been studied within the program. These alloys are strengthened at temperatures at or below 800°C by a combination of small (<300Å)  $\gamma'$  precipitates and a very fine dispersion of metastable D0<sub>22</sub> structure Ni<sub>3</sub>Mo or D1<sub>a</sub> structure Ni<sub>4</sub>Mo particles. Overall, significant progress has been made in understanding both the alloy design aspects and the strengthening mechanisms of LAYERGLAZE processed alloys.

## INTRODUCTION AND BACKGROUND

This report summarizes the results of a program which was designed to translate the results of rapid solidification surface processing to improvement of bulk materials. Research on this program was initiated in August 1978, and spanned nearly two and one-half years through December 1980. All phases of the program were completed, with the exception of the spin testing of a piece of model hardware (a turbine disk shape). This final phase was omitted due to a re-direction of program effort by the contracting agency.

Rapid solidification processing is of interest in that it is a technique which is inherently capable of producing homogeneous or uniform metallurgical microstructures. Given the fact that materials often fail as a result of inhomogeneities in the structure, improvement of homogeneity should allow more complete utilization of material strength; that is, improved material performance. Homogeneity is normally at its greatest in the liquid state. Upon normal solidification and subsequent slow cooling in the solid state, phase separation and segregation may occur. Once inhomogeneities are created in the solid, it is difficult to rehomogenize the material without remelting it. Although various materials processing operations (such as rolling, swaging, forging and heat treatment) will improve the homogeneity while still in the solid state, they will not usually be capable of producing optimal structures once the material has segregated.

Rapid solidification processing makes use of the high degree of liquid phase homogeneity. By sufficiently rapid solidification and subsequent rapid cooling through the highest temperature regions in the solid state, uniform structures with a high degree of homogeneity can be maintained to sufficiently low temperatures that they become stable. These structures can often be generated by controlling the solidification and cooling rates, and desirable structures tailored to performance requirements can be selected. By using rapid solidification techniques to select and control material structures, the technology promises to raise material performance levels in the future. The rapid solidification laser processing research on which the program was largely based is summarized in Refs. 1-12.

Laser melting, while just one of several techniques for rapid solidification processing, appears to offer numerous advantages, the most prominent of which is in-situ consolidation. Although rapid solidification still must be accomplished in thin sections, when fabricated by laser, the sections are consolidated together as they are added, obviating the need for further consolidation or exposure to elevated temperature. This is the main difference from the "powder metallurgy" or "ribbon" approaches to rapid solidification, and may ultimately be significant in the technology.

The LASERGLAZE Process was rapidly recognized as having obvious potential for treatment of metal and alloy surfaces and alteration of properties through structural selection and control. Material property areas where surfaces are important include erosion resistance, wear resistance, corrosion resistance, and, to the extent that fatigue crack initiation occurs at surfaces, fatigue resistance. Analysis of the heat flow considerations involved with LASERGLAZE revealed that, as with any other rapid solidification and quenching technique, high cooling rates could be achieved only in thin sections, with the maximum cooling rates increasing as the section thickness decreased. Figures 3 and 4 of Ref. 4 summarize these heat flow calculations. The conclusion was that the effects of LASERGLAZE on material properties were limited to what could be accomplished by structural modification and control of thin surface layers. This restriction was considered to be the most severe limitation of the new technology.

A logical, though not immediately obvious extension of the LASERGLAZE technology was the concept of sequential deposition of rapidly solidified and cooled thin layers to build up a bulk, rapidly-solidified material with a homogeneous, controlled microstructure. The evolution of this concept, eventually termed the LAYERGLAZE Process made possible for the first time the fabrication of bulk, rapidly solidified materials which, in contrast to the powder metallurgical approach, could be fabricated to full density without the need for a post-fabrication consolidation or densification step.

The initial LAYERGLAZE concept was evaluated under DARPA sponsorship between March and September 1977, and the results of this Performance and Cost Benefit Analysis are reported in detail in Ref. 13. This program was conducted to assess the potential performance and cost benefits which could be realized if the LAYERGLAZE Process could be developed to fabricate gas turbine engine disks, and also to establish and demonstrate the technical feasibility of the physical process for LAYERGLAZE buildup. The results and conclusions of this preliminary evaluation are summarized below.

#### A. Major Conclusions

##### 1. Performance

A 50% reduction in the live (load carrying profile) disk weights of the JT10D-4 can be realized for the high pressure compressor, high pressure turbine and low pressure turbine rotors, when designed using LAYERGLAZED alloys with assumed properties. This amounts to a minimum of 400 lbs (181.8 kg)/engine.

## 2. Cost

The total estimated Life Cycle Cost (LCC) reduction due to the use of LAYERGLAZED alloys in the F-100(3) engine for the F-15 aircraft, when designed for optimum LCC in the high pressure compressor and maximum weight savings in the remaining components, is \$222.4 million.

## 3. Process Feasibility

The LAYERGLAZE process for sequential, in-situ buildup of dense, high cooling rate structures appears to be feasible at rates of 0.5 cu in/min (8.2 cc/min) at the 6.0 kW laser power level, with deposition rates of 1.0 cu in/min (16.4 cc/min) anticipated in the 10.0-15.0 kW power range. Thermal calculations indicate that the part can be cooled and rapid cooling rates can be maintained in large parts.

## 4. Alloy Design Concept

High yield strength alloys were produced from eutectic starting materials; the results from the NiMoAl alloy which displayed a yield strength of 1755 MPa at 760°C suggest a fruitful path for further alloy optimization.

## B. Additional Results and Conclusions

### Task 1 - Performance and Cost Benefits/F-100(3)

1.1 Design evaluations of the F-100(3) and FEAT engines indicated that yield strength was less important than LCF and fracture toughness, pointing the way for emphasis in the areas of microstructural perfection and in-situ inspec-tability during future process development work.

1.2 A composite engine layout depicting the present B/M F-100(3) as com-pared to the redesigned engine using LAYERGLAZE processing was shown.

1.3 The total expected weight savings from using LAYERGLAZE processed PDS alloys in the F-100(3) is 111.3 lbs (51.4 kg).

1.4 A manufacturing cost reduction of \$27,900/unit (17% of cost of parts studied) is projected for the F-100(3) engine by using LAYERGLAZE processed PDS alloys.

Task 2 - Performance and Cost Benefits/FEAT

2.1 A composite engine layout depicting the present B/M FEAT as compared to the redesigned engine using LAYERGLAZE Processing was shown.

2.2 The total expected weight savings from using LAYERGLAZE processed PDS alloys in the FEAT is 71.8 lbs (32.6 kg).

2.3 A manufacturing cost reduction of \$9,600/unit (16% of cost of parts studied) is projected for the FEAT engine by using LAYERGLAZE processed PDS alloys.

Task 3 - Performance and Cost Benefits/JT10D-4

3.1 Although strengths of 200,000 psi (1380 MPa) and 300,000 psi (2070 MPa) were assumed for Ti and Ni base alloys respectively, substantial fractions of the total predicted weight savings can still be realized at much lower strength levels, i.e. ~80% of weight savings could be realized with alloy strengths as much as 30% below those sought.

3.2 Total weight savings for the engine parts analyzed is predicted to be no less than 400 lbs (181.8 kg) which is equivalent to a reduction of 0.40% in Direct Operating Cost + Interest. By optimizing the way in which improved material properties are utilized, weight savings could potentially be increased by approximately 100 additional pounds (45.4 kg) (equivalent to 0.478% DOC + INT).

3.3 Because the rotor weights can be reduced with LAYERGLAZE process it is possible to also save weight at the bearing supports. Maneuver loads will be reduced due to smaller rotor weight thus possibly reducing case thicknesses. However, where static structures are limited for deflection requirements, no weight savings would be realized.

3.4 Cases fabricated by the LAYERGLAZE process could result in some weight savings where the design is limited by containment or LCF. Wall thickness could be reduced with a high ultimate and fatigue strength material.

3.5 Manufacturing cost estimates indicated that there would be no predictable difference in the manufacturing costs for commercial engines with LAYERGLAZED parts, so that predicted performance/weight/DOC+INT gains would be obtained without initial cost increases.

Task 4 - Life Cycle Cost Studies/F-100(3), FEAT

4.1 Maximum impact on life cycle cost savings was not coincident with maximum weight reduction in all cases. Extension of part life to the cycle limit, and acquisition cost reduction are the most potent factors.

4.2 According to design personnel, the ability to tailor structures for added life with LAYERGLAZE processing is potentially the most important benefit of the technology. The flexibility to adjust the structure, and to opt for specific properties is not available to the same degree in presently utilized materials systems.

4.3 The total estimated Life Cycle Cost reduction due to the use of LAYERGLAZE/PDS alloys for the F-100(3) engine in the F-15 aircraft, when redesigned for maximum weight savings, is \$141.7 million. When optimized from the LCC standpoint, rather than weight savings, the total estimated Life Cycle Cost reduction was \$222.4 million.

4.4 The total estimated Life Cycle reduction due to use of LAYERGLAZE/PDS alloys for the FEAT engine in the ATS aircraft due to initial cost and weight reduction is \$103.4 million. (Since the FEAT is designed based on presently unobtainable advanced material properties, should its construction be made possible by LAYERGLAZE technology, this technology should "get credit" for the much larger performance and cost benefits inherent in the FEAT design.)

Task 6 - Technical Feasibility Demonstration

6.1 Cooling rates of  $10^5$ - $10^6$ °C/sec can be produced at power densities in the range of  $10^4$ - $10^5$  watts/sq cm, a level comfortably within the equipment capability. (It has been shown under Task 7 that alloys produced at these cooling rates have exhibited significant properties.)

6.2 Process efficiency increases with increased cooling rate, with less specific energy being required for unit deposition of new material. Increased power densities and higher processing speeds (shorter dwell times) are required to obtain higher cooling rates.

6.3 Thermal analysis modeling the LAYERGLAZING process indicated that a 1 in. wide, 0.001 in. strip on the surface of a disk could achieve a cooling rate in excess of  $10^6$ °C/sec.

6.4 Observations of the deposition process to date indicate that substantial progress in LAYERGLAZE processing will result from further development effort.

6.5 A 0.200 in. (0.508 cm) deep flange of type 304 stainless steel was fabricated using a small scale LAYERGLAZE apparatus which applied material by a wire feed technique. Flange material was fully dense and free of flaws as inspected by radiography.

Task 7 - Alloy Design and Evaluation

7.1 In order to obtain high strength coupled with ductility, the best approach appears to be through the preparation of metastable, single phase alloys which are hardened by phase decomposition in the solid state.

The potential of the LAYERGLAZE Process having thus been established, the present program was proposed, eventually procured, and was begun officially in August 1978. This program for Fabrication and Testing of a Scale Model LAYERGLAZE Turbine Disk originally involved six tasks, including:

Task 1 - Definition of a suitable method of LAYERGLAZE disk fabrication for a 5 in. (12.7 cm) diameter test part.

Task 2 - Identification of an alloy suitable for LAYERGLAZE model disk fabrication and testing.

Task 3 - Design and construction of the apparatus necessary to fabricate a 5 in. (12.7 cm) diameter test part.

Task 4 - Design of a suitable model disk part and a suitable spin test.

Task 5 - Fabrication and test of one 5 in. (12.7 cm) diameter model turbine disk, according to results of Task 4.

Task 6 - Fabrication of additional demonstration disks within the scope of available funding.

This program has been underway for the past two and one-half years. During this period, tasks 1 through 4 above have been substantially completed. Some problems of unanticipated difficulty were encountered in the alloy design area, primarily related to the phase stability of the as-layerglazed material following elevated-temperature exposure after deposition. The alloy design section of this report details the extensive investigation which was conducted in an attempt to identify compositions which would benefit from the effects of LAYERGLAZE Processing, and where phase stability would not be a problem. As of the end of the program several candidate compositions had been identified, and the mechanical properties of these are slated to be evaluated under an alloy characterization program at UTRC which has been sponsored by NASC. The sections which follow, report, in detail, the progress made in this Program to Investigate Advanced Laser Processing of Materials.

## EXPERIMENTAL PROCESSING OF LAYERGLAZED MATERIALS

## A. Apparatus

The LAYERGLAZE Process requires the use of a high power optical beam at a power density of between  $0.15\text{--}1 \times 10^5$  watts per square centimeter. As a consequence, an environmental control chamber must be used so that an acceptable shield gas such as He can be controlled around the interaction region. Introduction of the gas provides protection for the interaction region and prevents optical breakdown from occurring. This chamber, along with other essential components to the process, is shown in Fig. 1. The optical beam from the laser is first turned by an optical flat mirror,  $M_1$ , and redirected to the focusing mirror,  $M_2$ . The focusing beam is then transmitted into the environmental chamber through a small diameter aperture. Interaction with the workpiece takes place approximately 5 cm below the aperture. The wire feed nozzle is attached to the chamber and directs the wire in space to the interaction region on the arbor. A different nozzle in the same position is substituted when powder is fed to the interaction zone. The arbor, which in all cases was a 304 stainless steel cylinder 5 cm long by 3.7 cm diameter with a 3.2 mm wall thickness, is water cooled through a specially fabricated mandrel. This mandrel is attached to a variable speed motor in order to vary the rotational speed. The complete assembly is attached to a numerically controlled X,Y,Z table which allows for full motion of the arbor to allow for the LAYERGLAZE buildup.

Figure 2 shows a larger environmental chamber fabricated under a UTRC program and used in conjunction with a numerical controlled vertical miller. The numerical-controlled system is capable of linear speeds up to 7.62 cm/sec and has linear interpolation so that motion is essentially uniform in all planes. With this new system, it is possible to completely automate the LAYERGLAZE Process.

The wire feed system is shown in both Figs. 1 and 2 and is a commercially available dual-drive unit capable of delivering wire from a fraction of a centimeter per minute to over 100 centimeters per minute. Wire size can be varied between 0.051 to 0.127 cm diameter.

When powder is being used as the working fluid, the wire feed system is replaced with a powder feed system, see Fig. 2. A vibrator is used to provide mechanical shaking which excites the gravity powder flow process. Figure 3 shows the stream of powder being emitted from the nozzle under typical run conditions. It should be noted that the nozzle-to-workpiece distance is typically 6.3 mm (1/4 in.) for both the wire and powder. Within this range, the powder stream approximates a straight line.

## B. Determination of Process Criticality

The initial phase of this program was devoted to determining the critical parameters which are required to achieve a uniform homogeneous, nonporous, LAYERGLAZED part. The data and the LAYERGLAZED parts reported in the final report, Assessment of Advanced Laser Materials Processing Technology (Ref. 13), were achieved with an optical system that generated a Gaussian-shaped beam. Table I gives the typical operating conditions used to obtain this information. Data taken from a high speed movie of the process were used to generate some of the numbers listed, column 1. In the present program, the laser system was changed because it was felt that a Gaussian beam was not necessary for the process and at UTRC a crossflow laser was available with a suitable, high quality unstable resonator beam. As such, the parameters were then adjusted to give an approximately equal power per unit area, column 2. A comparison of the results showed that even though the prior reported results were at best only poor to good in comparison, the new results could only be judged as poor. Examination of the results at this time indicated that one possible problem could be explained by high-power densities which caused optical breakdown and spiking in the fusion zones that were being produced. The result was to decrease the power density by decreasing the power and by increasing the laser beam spot size. Once this was achieved, column 3, the optical breakdown problem disappeared.

With the breakdown problem under control, the process of achieving uniform deposition of the 308 stainless steel wire on the stainless steel mandrel was faced. One of the first problems encountered was droplet transfer onto the mandrel, Fig. 4a. This drop transfer was detrimental to the process, because large droplets, as shown in Fig. 4a, were transferring to the arbor in a periodic fashion. It was noticed early that the drop transfer was neither consistent in size nor in its periodicity and that under certain conditions, the drop transfer was nearly nonexistent and that the material transfer was very smooth. Many samples were produced under varied experimental parameters until the most optimum condition was achieved. Figure 4b shows such a condition. Figure 4c shows the effect of drop transfers after several layers of buildup. Once the pattern is set on the first pass, as the process goes over the perturbation represented by an already transferred droplet, the droplet acts as a "rake" and removes all of the molten pool from the wire causing the perturbation to grow. This, of course, was unacceptable.

The final near-optimum relationship between the optical beam, the arbor, and the wire are depicted in the isometric drawing of Fig. 5. With the arbor rotating in a counter-clockwise direction at a rotational speed of  $\omega$ , a teardrop shaped molten zone is obtained on the arbor at steady state when the impinging optical beam is circular, as shown. The teardrop is typically twice as long as the beam diameter. The spatial location of the wire is at this point, probably the most critical of all parameters. The angle of the wire

relative to the plane at the interaction point was held to 30° and the extended length of the wire beyond the nozzle tip was held to 6.3 mm (1/4 in.). If the wire extension is longer, it cannot be precisely located at its tip, and if it is too short, the nozzle interferes in the interaction zone. It was found that the wire had to touch just in front of the molten pool, as shown, in order to give proper material transfer. If the wire wanders from one side to the other, it would be split by the laser resulting in incomplete melting. If the wire is displaced in the plane of rotation then conditions could allow drop transfer or wire instabilities, Fig. 6. If the wire is allowed to pass over the beam and touch inside the molten pool area, then melting of the wire occurs at some height above the arbor, allowing a large droplet to form until it drops onto the surface because of its weight. Likewise, an unstable condition is also achieved if the wire is allowed to touch the arbor  $\geq 2$  wire diameters in front of the molten pool. In this case, the wire becomes too long and moves around randomly causing instabilities. The only stable condition is shown in the figure with a displacement of the wire of up to 2 wire diameters allowed for stability. It should also be noted that the interaction zone is substantially below the focal plane as indicated in Fig. 6. The photographs of Fig. 7 show what effect power distribution has on the shape of the fusion zone. In this case, a 61 cm focal length mirror was used. The beam from this mirror impinged upon the test sample that was set up as an inclined plane. Thus, the fusion profiles above and below the focal plane could be determined. At the focal plane, using a 6 kW optical beam, the power density is approximately  $0.418 \times 10^6 \text{ w/cm}^2$ , whereas at 64.8 cm, the power density is  $\sim 0.78 \times 10^5 \text{ w/cm}^2$ . The graph of Fig. 8 depicts in another way how the beam diameter varies as a function of position. As the number of test specimens increased it was determined experimentally that a power density of approximately  $0.78 \times 10^5 \text{ watts/cm}^2$  gave the best appearing deposition.

### C. Wire Feed Development

The initial stages of the program were devoted to determining what parameters were required to deposit stainless steel wire on a stainless steel arbor. The decision to use this procedure was based on the philosophy of allowing model tests to be run in such a way that the process itself could be understood without being complicated by materials effects. The wire feed system was described previously along with the experimental procedure required to deposit material on the arbor. In all cases, the wire diameter was 0.089 cm. These tests were designed to allow for smooth deposition of wire on the arbor. Once the proper parameters were obtained tests were initiated to determine the requirements for deposition of multiple-layers of wire on an arbor.

The first parameter changed was the cross-feed rate which in turn would determine what, if any, was the effect of laying the wire adjacent to or overlapping the previous pass. Figure 9 shows a closing up of the single pass spiral as the cross-feed rate is decreased from 0.085 cm/sec down to 0.051 cm/sec, the lower limit of the x-y table. A similar series of tests, Fig. 10, was then run with 5 layers of wire being LAYERGLAZED onto the arbor to determine what if any effect the overlay had on the process and how it affected the metallurgy of the sample. The macroetched cross sections for the five layer cases are also shown in Fig. 10 and it is obvious that the slower cross-feeds result in superior deposition both in uniformity of the matrix and of the surface. Thus a cross-feed rate of 0.051 cm/sec was chosen for the remainder of the tests.

The test was then extended to determine whether or not any problems would be encountered with a very large number of layers deposited. An arbor was prepared with a total of 58 layers. A direct comparison of the surface condition for 1, 5 and 58 layers is seen in Fig. 11. As the number of layers is increased the surface becomes substantially rougher. The cause for this occurrence is most probably the enhancement of small imperfections or instabilities deposited at the earlier stages.

The 58 layer sample was then subjected to several tests. The first one was the machining of the outer surface to see if any imperfections could be found below the rough surface. A direct comparison between the as-deposited state and the machined surface is seen in Fig. 12. The machined surface was determined to be quite smooth with only a few minor imperfections being uncovered.

The sample was then cut along the axis on one side with a 0.330 cm width cutting wheel. When the cut was completed, the arbor sprung open 0.190 cm. This was considerably less than half of the normal springback for the mandrel tube, indicating that very high compressive forces on the arbor were present as a result of the deposited material in the process. (See Appendix A). A wedge along the length of the arbor was then removed so that the sample could be examined metallurgically. Three different macroetched photographs of the 58 layer deposit, Fig. 13, show the quality of the structure. The upper surface in Fig. 13a is the surface that was machined. The lower surface is the 304 stainless steel arbor. Two major concerns can be noted when examining the macrophotograph, Fig. 13a. One is the deep penetration type spiking that occurs throughout the deposit and the other is the voids associated with the spiking. These are shown more clearly in Figs. 13b and 13c. The deep penetration spikes were unexpected because it is known that deep penetration occurs at power densities in the range in excess of  $10^6$  w/cm<sup>2</sup>. The conditions under which this sample were generated, involved a power density of only  $0.62 \times 10^5$  w/cm<sup>2</sup>, far below that normally required for deep penetration. A melt cross section obtained

under similar conditions is shown in Fig. 7 at 64.8 cm and there is an obvious lack of deep penetration. Several possible causes of the spikes were examined and the only plausible one deals with the rough surface of the arbor which is present after the wire is deposited. The rough surface is formed when two adjacent passes that overlap are deposited onto the arbor, Fig. 9. The high freezing rates associated with the process along with surface tension forces combine so as not to allow the material to flow into a flat, uniform surface. As a consequence, a well or "v" groove is formed on the surface of the first and subsequent layers. As the process is reversed and the wire is deposited with an opposite spiral, a cavity is formed at the intersection of the top layer and the layer on which it is deposited. This cavity becomes a steep-walled radiation trap for the  $10.6\mu$  radiation. Under these conditions it is very reasonable to expect that the power density at the base of the cavity could exceed  $10^6$  w/cm<sup>2</sup>, thus causing the deep penetration type spiking and the associated voids. The voids are normally formed at the root of the spike because of the rapid solidification rates that the materials experience at this location.

#### D. Powder Feed Development

The program was reevaluated following initial wire-feed studies, and different options were considered in an effort to alleviate the problems of the deep penetration type spiking that were associated with the wire feed. Two primary options included either the reduction of wire size or the use of powder in order to reduce the scale of surface irregularities. Both of these options initially presented problems because smaller wire diameters were difficult both to obtain and to handle, while severe difficulties had been associated with all previous attempts to feed powder directly into the laser beam. Some preliminary tests with a simplified powder-feed setup (see Fig. 3), however, indicated that there was a possibility that the process could be made viable, and, based on the first deposits made during preliminary tests, decisions were made to develop a powder process and to convert a representative alloy ("8-12-3" was chosen, see alloy design section) into powder for fabrication tests. The primary motivation for this decision was that obtaining LAYERGLAZE alloy powders was far easier and faster than obtaining the same alloys in wire form. If the powder deposition could be made to work, it would facilitate rapid progress to the point of being able to obtain mechanical test data on actual LAYERGLAZE-fabricated material.

A powder delivery mechanism was fabricated employing the simple technique described above. The powder delivery rate from the 8-12-3 mixture was experimentally determined to be 0.14 gm/sec, Fig. 14. One problem encountered with the powder feed was the inability to deliver constant mass flows for long periods of time. Using a 0.089 cm diameter nozzle, the range of mesh sizes was found to be most critical. The optimum powder size was found to be from -170 mesh to +500 mesh. If only finer powder size fractions were used the

powder feed would clog. Conversely, if the large powder sizes were used free flow would be achieved, but the powder flow rate could not adequately be controlled. It should be noted that use of as wide a range of mesh sizes as possible was desirable because of the yield factor.

An additional factor found to contribute to the clogging of the nozzle was moisture. As a result, the powders were dried in a vacuum oven and then stored under an argon environment. Powder transfer to the nozzle assembly was accomplished by transferring the powder in a dry box to a small container and then transferring this powder in the atmosphere to the nozzle. This keeps the powder dry enough to allow for uniform flow. A more desirable approach would be to keep the powder away from the atmosphere at all times during the transfer process. This would require a more sophisticated design beyond the scope of this program.

Upon receipt of the 8-12-3 powder a series of tests was designed to determine what operating parameters would yield the best deposits. The first of these was the criticality of alignment in the interaction zone between the optical beam, the arbor, and the powder. It was found that the criticality of this parameter was identical to that determined for wire feed with the arrangement being the same as depicted in Figs. 5 and 6. The location of the stable region was for all practical purposes the same. In the unstable region, the appearance of the surface changed appreciably from that of the wire deposition. The powder when injected into the beam volume would melt and spatter. Also, it caused optical breakdown because the beam was being seeded with the powder. When operating in the stable region the surface of the deposited material was very smooth, Fig. 15. For the samples shown in Fig. 15 approximately 1/3 cm of the 8-12-3 powder was LAYERGLAZED on the standard water-cooled, stainless steel arbor. The deposit was made almost 2.5 cms wide so that end effects could be distinguished from the bulk of the deposited material. From the onset of the powder tests, it was obvious that, under optimum conditions, both the ease of deposition and quality of the deposit were potentially superior to those characteristic of wire deposition. This was evident just by looking at the surface appearance. Figure 15 contains a comparison of the surface in the as-deposited condition and after reglazing. The glazed portion was achieved by turning off the powder feed and allowing the laser to remelt and smooth out the surface. The small spherical type "spatter" deposits located on the as-deposited section are remelted into the deposit on the glaze pass leaving an almost mirror smooth surface. A major additional advantage of the powder feed over the wire feed is that the laser coupling efficiency is much higher with the powder, leading to a much higher energy deposition efficiency, and, as a result of the facilitated coupling, enhanced process stability is achieved in the interaction zone.

It was felt that the quality of the deposit was also affected by such items as the optical power and the mass flow rate. A test was then run with the optical power at 3 kW, 4 kW, and 5 kW, Fig. 16. Obviously the 3 kW test

did not allow for complete melting and flowing of the deposited powder, whereas at 5 kW complete melting and flowing did occur. This would be expected if the total energy and power density were allowed to decrease which it did. The 4 kW test was almost as good as the 5 kW test, however, there was evidence of slightly more spatter.

The mass flow rate of the 8-12-3 powder was increased by increasing the diameter of the nozzle from 0.089 cm to 0.114 cm. This is an increase in cross sectional area of 65 percent. If the flow rate increase is in direct proportion to the area, it would be expected that the mass flow would be increased by 65 percent. This in fact did not happen (Fig. 17) because the deposit per layer increased from 0.025 cm to 0.081 cm with the larger nozzle area. This is most likely due to the change in the friction or flow coefficient of the nozzle. Obviously from the difference in surface condition, Fig. 17, the slower flow rates are desirable with this energy input. The effect of increasing the mass flow is equivalent to a decrease in the energy per unit volume. The result is a very rough surface deposit which is not desirable.

#### E. Fabrication of Samples for Mechanical Test

Successful glazing of thin section deposits from the 8-12-3 powder was followed by attempts to build up heavy sections for mechanical testing of the alloy on the 3.8 cm diameter arbor. The acquisition of the numerical controlled vertical miller (Fig. 2) led to the simplification of the process. The computer was taped to control both the horizontal and vertical motion of the arbor while the LAYERGLAZE process was taking place. The data used to generate the tape came from experience in the deposition of the powder. It was found that under optimum conditions on the average 0.010 cm of material was added to the arbor on each layer.

The first glazed powder test sample (#1-8) generated using the new system is shown in Fig. 18. The overall diameter of the test sample was 6.45 cm. The initial surface speed was 8.47 cm/sec and the final speed was 14.2 cm/sec. The speed varied because of the outside diameter buildup with a constant rotational speed. The top surface is quite smooth except for a minor rounding off at the edges. This rounding off is due to the roll off of the powder at the edge. Along each side of the arbor, rough and porous spatter deposits are seen. This is due to powder loss over the edges into a region of low power density or low energy density where it is only partially fused to the substrate. Cleanup of the side surfaces was achieved by machining away these surface deposits, as shown in Fig. 19, and it should be noted that no pores or other imperfections were observed on either surface.

Metallurgical examination of sample 1-8 was very encouraging. Initially, the sample was cut in half, with the intention of sacrificing one-half for mechanical test specimens and saving the other half for display, or to use for additional test specimens as needed. The eventual sectioning and testing of sample 1-8 is described later, and detailed in Figs. 25 and 26.

The sample, as cut in half and macroetched, is shown in Fig. 20. The integrity of the deposited material, as well as the uniform layered structure, are obvious in this transverse section. It can also be seen that there is considerable compression on the central mandrel from the way it is deformed.

In Fig. 21, an end-view of the sample is shown. Of interest here is the strong tendency for epitaxial growth from layer to layer, resulting in what is essentially a radially directionally-solidified, layered growth pattern.

Structural analysis and mechanical testing of sample 1-8, as discussed in the following section, revealed that the material was sound, free of major flaws, had good structural integrity, reasonable strength, and excellent ductility.

#### F. Fabrication of Full Size Disk Preform

Based on the satisfactory characteristics of sample 1-8, a full size 13.2 cm diameter turbine disk preform was made as a fabrication exercise, primarily to demonstrate that a part of the full size could be made without encountering unforeseen problems such as excessive stress buildup during fabrication of larger diameters. This part is shown in the as-fabricated condition in Fig. 22, and machined to a typical turbine disk shape in Fig. 23. Its thickness varied from 3.2 cm adjacent to the mandrel to 2.3 cm at the outer diameter. The part was fabricated on a standard, 3.8 cm diameter, water-cooled stainless steel mandrel. Although initial intent was to fabricate the part from our alloy 8-12-3, which at the time of fabrication was our first program-generated disk alloy, we did not have a sufficient supply of 8-12-3 powder to complete the fabrication of a full-size part. The part was thus initially fabricated out to a diameter of 8.4 cm from the 8-12-3 alloy. To complete the fabrication, IN-718 alloy was used, as it was believed that this would serve to generate a full size part and thus allow us to demonstrate the feasibility of full size fabrication. Also, the change of material would demonstrate ability to alter composition. Since our experience with conventional superalloys had not shown any to be suitable for LAYERGLAZE fabrication, there was some question as to the fabricability of IN-718 by this process.

Fabrication was completed with both materials appearing to fabricate satisfactorily. A problem was encountered with curving of the outer surface, which in this test was solved with manual buildup, but which will require some future processing improvements for optimum disk fabrication.

Upon machining, although both alloys machined to smooth surfaces and appeared to have good structural integrity, some important differences in behavior were noted. Firstly, the 8-12-3 was much harder to machine, but produced a better surface finish. Only by using a finish grinding operation was it possible to fully smooth out the IN-718, indicating the possible presence of fine cracking. The final machined part in Fig. 23 is also shown with part of the surface macroetched, revealing the radial growth structure.

Eventually, this sample disk was cross sectioned, and is shown in Fig. 24. It should be noted that only one face had been machined, so that the sample possessed both an as-fabricated and as-machined face. As expected, the structure and the structural integrity of the 8-12-3 deposit was excellent. The IN-718, however, showed a type of microcracking in the plane of the disk which we call axial or Type II cracking. This observation is not considered as problematic in this program because alloy IN-718 is not intended to be a part of the program. The observed microcracking confirms our belief that few, if any, conventional superalloys can be satisfactorily fabricated by the LAYERGLAZE process. The program-developed alloy, 8-12-3, however, has proved to be adequately fabricable, and, it is noted in the alloy design section that there are several additional program-developed alloys which appear fabricable by LAYERGLAZE and possess improved properties.

The cross section in Fig. 24 shows that the compressive deformation in the inner mandrel is no greater than in the smaller diameter buildup in part #1-8. This confirms our calculations that compressive stress is maximized and that, eventually, the LAYERGLAZED material begins to support the material added above it. The ability to generate a compressive stress at the bore of the disk may eventually be exploited to the advantage of this type of fabrication. Appendix A is a summary of stress analysis calculations conducted under this program.

The total fabrication experience to date has indicated that a powder fed LAYERGLAZE system of the type described above is capable of fabricating parts of the size necessary to meet program goals, with good structural integrity.

## ALLOY DEVELOPMENT FOR LAYERGLAZE FABRICATION

## A. Introduction

The development of nickel base superalloys for use as turbine disks fabricated by the LAYERGLAZE process was dictated by three requirements: (1) an absence of cracking after LAYERGLAZE deposition, (2) beneficial response to solidification rates of  $\sim 10^4$ °C/s, and (3) strength and low-cycle fatigue properties which exceed those presently obtainable. The primary consideration in the evaluation of each alloy was that it should not crack when laser welded with bead-on-plate overlapping passes. Preliminary testing revealed that no conventional nickel base superalloy of adequate strength was able to meet this specification. Consequently, the main effort in alloy development was directed toward new compositions which would be ductile just after solidification, but strong and phase stable at temperatures of  $\leq 760$ °C (1300°F).

Research within United Technologies by Lemkey (Ref. 14), Pearson (Ref. 15), and Aigeltinger, et al. (Ref. 16) had suggested that alloys based on the nickel-aluminum-molybdenum system might be expected to exhibit this type of response when LAYERGLAZE processed. The rationale for choosing this group of alloys was based on their observed resistance to laser weld cracking, lower  $\gamma'$  volume fraction for ductility during post-solidification cooling, and potential of age hardening by the precipitation of finely dispersed  $Ni_3Mo$  and/or  $Ni_4Mo$  intermetallic compounds in the  $\gamma$  solid solution. Concurrently, a more extensive evaluation of conventional nickel base superalloys was conducted in an attempt to determine what (if any) compositional modifications would improve their laser fabricability.

## B. Experimental Procedure

## 1. Laser Weld Cracking Evaluation

All alloys chosen for evaluation were first tested for resistance to laser-weld cracking. The selected alloys were made up from elements of  $>99.99\%$  purity, melted together under argon in alumina crucibles, and chill cast into  $0.8 \times 5.7 \times 17.8$  cm slabs. Square blanks of approximately  $0.8 \times 2.8 \times 2.8$  cm size were cut from these slabs, ground smooth with a random scratch pattern on one face with 240-grit silicon carbide paper, and cleaned in acetone. These as-cast specimens were bead-on-plate deep penetration laser welded, ground face uppermost, with a continuous, carbon dioxide laser operated in the unstable resonator mode. As many as 16 specimens at one time were mounted near the rim of a 45.7 cm diameter, horizontal, rotating wheel (Fig. 25), similar to that previously utilized for the LASERGLAZE process (Refs. 11,17). The upper surface of each specimen was positioned so as to lie in the focal plane of the 45.8 cm focusing

mirror. The wheel was rotated beneath the fixed point of beam impingement so that the effective beam traverse speed was 5.08 cm/s. The laser was operated at a power setting of 6 kW; thus the beam power delivered after window and mirror interface losses was ~4.7 kW, or ~1.0 MW/cm<sup>2</sup> beam intensity at the specimen surface. Most of the upper surface of each specimen was converted to a continuous layer of bead-on-plate welds with overlapping fusion zones by translating the rotating wheel on which they were mounted sideways by 0.38-0.76 mm per revolution. The specimens were protected from oxidation during welding by covering the wheel with an aluminum shield and introducing 100% helium flowing at 1.4 m<sup>3</sup>/hr.

The entire welded surface of each specimen was examined for cracks at 30X with a stereoscopic microscope. In addition, its post-weld microstructure was observed on a plane cut perpendicular to the welded surface and to the welding direction. If no cracks were observed in the fusion zone by either technique, the alloy was selected for further evaluation. Metallographic observations were made on this same transverse section to determine fusion zone profiles and depth, microporosity and/or microfissuring, if any. Some as-chill cast and as-laser welded specimens were examined by transmission electron microscopy (TEM) with a JEOL JEM-120 or a Philips EM 400T, both operated at 120 kV.

## 2. Differential Thermal Analyses

The phase transformation temperatures of most of the experimental alloys were determined by differential thermal analysis (DTA). Pure nickel was used as the standard in all cases. Both the heating and cooling rates were held constant at 5°C/min. Data from each specimen was recorded for at least two thermal cycles. In some cases the precipitation or dissolution of Ni<sub>3</sub>Mo could not be detected by DTA. In this case, apparatus designed and built at UTRC was used to attempt to determine this particular phase transformation temperature by differential thermal expansion (DTE) (Ref. 18), again using a pure nickel standard.

## 3. Atomization

Some experimental alloys based on the nickel-aluminum-molybdenum system which exhibited crack-free laser weldability and relatively high as-welded microhardness were made up from pure metals and cast into single 22.7 kg ingots. These were converted to powder by the standard commercial argon atomization process by Homogeneous Metals, Inc. They were delivered to UTRC, packed in argon and sieved to -90 mesh. Each lot of alloy powder was then sieved further into specific powder size ranges to improve its flow characteristics.

#### 4. Evaluation of Specimens Fabricated by the LAYERGLAZE Process

Specimens fabricated from laser-melted powder by the LAYERGLAZE process were characterized by light microscopy, TEM, DTA, DTE, and tensile testing. The small annular disks of each alloy were sectioned into parallel-sided pieces (Fig. 26), then cut and machined by grinding into small tensile specimens (Fig. 27). In the case of disk 1-8 (alloy 8-12-3), these pieces were examined for porosity by radiography prior to machining. The tensile specimens were oriented so that the load axis of each was parallel to either the disk radius or the disk rotational axis.

Selected Layerglazed alloys were annealed at various temperatures as follows: (a) 1100-1290°C for 4 hrs in evacuated quartz capsules for homogenization and recrystallization studies, and/or (b) 538-760°C in air for 32-500 hrs to examine phase stability and age hardening characteristics.

#### 5. Identification Coding of Experimental Alloys

Experimental nickel base superalloy compositions which were developed in the course of this program were identified by a numerical code derived from the quantity of their elemental constituents in atomic percent. The number sequence of the code corresponds to the elements Al, Mo, Ta, Ti, Cr, and Hf, in that order. Thus, the alloy identified as alloy 8-12-3 had the composition 8 a/o Al, 12 a/o Mo, 3 a/o Ta, balance Ni. Alloy 11-12-0-0-5 was composed of 11 a/o Al, 12 a/o Mo, 5 a/o Cr, balance Ni. Any alloys composed of additional elements added to any alloy composition later in the research program were identified by an added number and chemical symbol. Alloy 8-12-3 + 1 V was composed of 8 a/o Al, 12 a/o Mo, 3 a/o Ta, 1 a/o V, balance Ni.

### C. Results

#### 1. Laser Weld Cracking Evaluation

The alloys selected for cracking evaluation can be conveniently categorized into two groups: experimental alloys based on the Ni-Al-Mo system, and conventional alloys (or modifications thereof), based on nickel and nickel-iron base superalloys currently in use or in advanced development. As described in the Introduction, the Ni-Al-Mo system had exhibited the potential for fabrication by laser processing. Consequently, a large number of such alloys were evaluated for laser weld cracking susceptibility as described previously. The test results are presented in Tables II-V. These alloys were not evaluated all at one time, but are rather the aggregate of several sequential groups of compositions chosen by an iterative process which involved an attempt to achieve a balance between crack-free fabricability, high strength and phase stability.

As illustrated by Figs. 28 and 29, the laser weld cracking susceptibility of these alloys was strongly dependent upon molybdenum content; so much so that a variation of  $\pm 1$  a/o Mo was critical. This effect was consistently reproducible and did not appear to be influenced by random fluctuations in carbon content or in the amount of other interstitial impurities (Table VIII). As might be anticipated from studies of conventional weldability in nickel base superalloys (Refs. 19-21), these alloys also began to crack when the quantity of  $\gamma'$ -forming elements (Al,Ti,Ta), and thus the  $\gamma'$  volume fraction, became too large. This effect was not investigated quantitatively, but was observed to be dependent of the Mo or Mo + Cr content of the alloy(s) involved. A third and somewhat surprising compositional effect was the detrimental influence of nominal amounts of hafnium, boron and/or zirconium, elements normally added to conventional nickel base superalloys to improve high temperature ductility (Table V). In the case of alloy 12-13, one of the most laser-weldable of the Ni-Al-Mo alloys investigated here, the addition of small quantities of Hf, B, and Zr, alone or in combination, induced varying degrees of cracking where none had been observed in their absence.

A number of strong nickel base superalloys were evaluated (Table VI) on the chance that they might prove to be laser weldable, although they were known to crack when conventionally welded (Ref. 19). In addition, the compositions of many of these alloys were extensively modified (AF2-1DA, modifications A-D; Astroloy, modifications A-G; Table VI) in an attempt to determine whether cracking could be eliminated at all without completely sacrificing strength or 760°C phase stability. Some of these modified alloy compositions appeared attractive, but their subsequent evaluation was not completed due to budgetary restrictions. Some lower strength superalloys such as IN 718 and IN 903 (Table VI) were laser weld crack tested to determine the suitability for concurrent LAYERGLAZE process development, but they were insufficiently strong for aircraft turbine disk applications.

The as-laser welded surfaces of several different weld crack test specimens are shown in Fig. 30. When cracks were visible on the upper specimen surface, they tended to be oriented transverse to the welding direction and to extend across many overlapping weld beads (Figs. 30b and 30c). Transverse cracks in the fusion zone were also observed during preliminary experiments in which a single welding pass was made in crack-prone alloys, and thus are not a unique characteristic of overlapping fusion zones. In a few instances, cracking along the center line of a single fusion zone was also observed (Fig. 30d). The cause of this difference in crack orientation was not apparent, although examinations of the fusion zones in transverse section indicated that cracks of all orientations were predominantly intergranular.

Observation of the as-welded surface structure at higher magnification revealed features which were common to all specimens: striations marking the successive location of the solid-liquid interface, and slip lines on the fusion zone surface caused by plastic accommodation of solid state contraction during cooling (Fig. 31).

The fusion zone of all alloys (Figs. 32-35) exhibited a much finer dendritic structure than that of the unwelded chill casting below it, indicative of the higher solidification rate inherent in laser welding. When cracks were intersected by a transverse plane of observation (Fig. 33), they displayed more of a center line orientation than suggested by observation of the top surface of most welds. In general, the microstructure in the fusion zone of the welded superalloys was assumed to be a close approximation of that produced by the LAYERGLAZE process. Support for this assumption can be derived from a comparison of as-laser welded microstructure of alloy 8-12-3 (Fig. 35) and photomicrographs of disk 1-8 (subsequently discussed). All alloys which were LAYERGLAZE processed after a positive laser weld crack test continued to exhibit crack-free behavior.

Previous investigators (Refs. 19,20) have reported that the weldability of nickel-base superalloys, particularly Rene 41, can be improved by softening them as much as possible prior to welding. To determine whether this procedure would reduce the weld cracking tendency of the experimental alloys used in this program, 20 previously evaluated chill-cast alloys based on Ni-Al-Mo were annealed in evacuated quartz for 4 hrs at 1290°C, then furnace cooled. They were subjected to the standard weld cracking test described previously. The degree of weld cracking observed was not reduced in comparison with the as-chill cast specimens for any alloy. In two cases, alloys 10-12-3 and 10-10.5-3, the amount of weld cracking was markedly increased as a result of the prior high temperature anneal.

## 2. Phase Transformation Temperatures

It was assumed that the tendency of nickel base superalloys to crack when welded might be lowered by reducing the melting range and/or lowering the  $\gamma'$  solvus temperature. In the former case, the persistence of interdendritic or intergranular regions of liquid which might contribute to crack initiation in welded areas which were cooling to near the solidus temperature would be reduced. In the latter case, the alloy would remain free of  $\gamma'$  for a relatively longer time during cooling in the solid state, and thus be more able to accommodate solidification shrinkage stresses by plastic deformation without fracturing. To determine whether these mechanisms might be operative in the case of the Ni-Al-Mo base alloys, their phase transformation temperatures were determined by differential thermal analysis (DTA), as shown by Table VII. Examples of the DTA traces for two such alloys are shown in Figs. 36 and 37. The peaks indicative of the melting and freezing of an alloy of eutectic composition shown in

Fig. 33 were not observed in all cases. It is not clear at this time whether or not failure to observe eutectic peaks on the DTA trace of a particular alloy might be due to insufficient sensitivity of the apparatus in some cases. The temperature at which  $D0_{22}$ -structure  $Ni_3Mo$  began to precipitate or dissolve was usually detectable by DTA, in which case the shape of the trace was similar to that obtained for the  $\gamma'$  solvus. In some instances, such as alloy 8-12-3, this transformation temperature could only be detected by differential thermal expansion (DTE). Nevertheless, all evidence to date indicates that intermetallic phases of the  $Ni_xMo$  group ( $x = 2, 3$ , or  $4$ ) will be present in the  $\gamma$  phase at temperatures below  $\sim 800^\circ C$  in any of the Ni-Al-Mo base alloys investigated here.

The  $\gamma'$  solvus and melting range data (Table VII) do not suggest an obvious correlation between these parameters alone and the dependence of weld cracking upon alloy composition. The sensitivity of laser weld cracking to small changes in Mo content (Tables II-VI, Figs. 28 and 29) precludes simplistic explanation. Even in the case of conventional alloys for which there exists extensive welding data (Refs. 19, 20), those mechanisms which are proposed to explain various types of weld cracking are in the form of reasonable explanations, unverified by direct cause and effect observations. Development of detailed explanations for the possible mechanism(s) which control fusion zone laser weld cracking in the Ni-Al-Mo base alloys investigated here remain speculative.

### 3. Chemical Analysis

The composition of five as-Layerglazed disks and several chill-cast and laser welded specimens were checked by wet chemical and Leco analysis (Table VIII). In most cases, the results are close to the nominal composition. The carbon content of all specimens was lower than that usually observed in commercial nickel base superalloys, and was not sufficient to allow one to assume that all of the interdendritic precipitates observed in various as-Layerglazed disks were carbides.

### 4. Mechanical Testing of LAYERGLAZE Fabricated Materials

#### a. Mechanical Testing of Disk 1-8 (Alloy 8-12-3)

The most extensive evaluation of the mechanical properties of LAYERGLAZE materials was conducted on disk 1-8. Fabrication of this disk was described in detail above and the macrostructure was shown in detail by Figs. 18-21. Radiographs of slabs cut from disk 1-8 (Fig. 26) indicated only one limited area of voids near the outer edge of one piece, and no detectable porosity in the other pieces. These radiographs are shown in Figs. 38 and 39. Absence of porosity of similar size was confirmed by sectioning (Figs. 44-53) where only extremely small ( $<0.001$  in. ( $25\mu m$ )) porosity was found. The density of LAYERGLAZE-fabricated 8-12-3 was found to be  $9.146 \text{ gm/cm}^3$  ( $0.330 \text{ lb/in}^3$ ).

The sections of disk 1-8 shown in Fig. 26 were fabricated into 19 mechanical test specimens of four different geometries as shown in Fig. 27. The strength and ductility measurements from these specimens, made at ambient temperature, 538°C and 704°C are presented in detail in Table IX. The engineering stress-strain curves for the ambient temperature tests appeared quite normal, and a typical example is illustrated in Fig. 40. No detectable variation in mechanical properties with tensile specimen size was found over the size range investigated. Also, no statistically significant variation was found between the strength of the radial and axial specimens at ambient temperature, despite the marked elongation of the grains in the radial direction. This is believed to be due to the fact that both the  $\gamma'$  precipitate in this alloy is so finely dispersed that the influence of the grain shape is not significant at ambient temperature.

The strength and ductility of the specimens tested at 538°C and 704°C (1000°F and 1300°F) were found to be highly dependent upon the direction of loading with respect to the disk microstructure. The specimens designated as axial were oriented so that the direction of loading was perpendicular to the radial direction of the disk, which is also perpendicular to the direction of preferred grain orientation and dendritic growth. These specimens exhibited pronounced decreases in both strength and elongation with increasing temperature as a result of intergranular and/or interdendritic precipitation of a brittle phase at the test temperature. The radial specimens maintained excellent ductility and showed only minor strength decreases with increasing temperature. This observation was consistent with their orientation, which is much less sensitive to the potential for intergranular or interdendritic fracture. Although there is potential for improving the elevated temperature strength behavior through heat treatment, the requirement for improved elevated temperature phase stability of LAYERGLAZE alloys was clearly pointed out by the elevated temperature tensile testing of disk 1-8 (alloy 8-12-3).

#### b. Mechanical Testing of Other Alloys

Additional mechanical test investigations were performed on alloys 12-15, 11-12-0-0-5, and 11-12-0-0-10. These alloys were fabricated during the progression of alloy design work performed in pursuit of improved elevated temperature phase stability. Samples for these tests were fabricated in a manner similar to disk 1-8, except that the LAYERGLAZED deposit thickness produced was adequate only for the fabrication of specimens with axial orientations. These specimens were machined from wedge-shaped slices of LAYERGLAZED material which were cut from the deposits on the fabrication mandrels.

A summary of the mechanical test data collected on the additional alloys appears in Table X. Since these alloys were known to be development stages and not final alloys, the mechanical testing was limited to a small number of representative specimens. Whereas alloy 8-12-3 was tested in the radial direction, and elongation data for the radial direction are shown, the other developmental alloys were tested only in the more critical axial direction. This was a consequence not only of the fact that this orientation was prone to lower elongation, but also of the fact that only a small tubular sample could be fabricated for reasonable cost, and as a result, it was not possible to fabricate radial specimens.

Table X effectively summarizes the available strength and elongation data for the Ni-Al-Mo-Ta alloys fabricated within the present program along with comparison data on the best currently available conventional disk superalloys through August 1980. Since that time, extensive additional alloy development has been conducted, but the program termination date did not permit further fabrication and mechanical testing. This work will be continued under contract no. N62269-80-C-0722 for the mechanical and metallurgical characterization of LAYERGLAZE processed alloys under the cognizance of the Naval Air Development Center.

It can be seen in Table X that tensile and strength values for the Ni-Al-Mo-Ta alloys compare favorably with the best conventional superalloys at ambient temperatures, and, although elevated temperature strength falls off severely in alloy 8-12-3, alloy 12-15 exhibits excellent high temperature strength. The problem with the Ni-Al-Mo-Ta series is the poor ductility which results from the above-detailed phase instability.

A typical ambient temperature tensile fracture surface is shown in Fig. 41A. This fracture surface in alloy 11-12-0-0-5 indicates that although some plastic deformation occurs, the fracture, which occurred at a strain to failure of approximately 3.7%, is primarily planar, indicative of the inadequate ductility of these alloys in their present form. There is evidence of the layering involved in the fabrication process on the fracture surface, but what appears to be imaged are heat affected zones, and they do not seem to contribute specifically to premature fracture. Following elevated temperature aging, however, or testing at elevated temperatures, fracture surfaces such as that in Fig. 41B were obtained. These fracture surfaces exhibit severe intergranular behavior due to precipitation of the embrittling grain boundary phases discussed above.

Further alloy development has pursued a two-pronged approach. While one effort has been aimed at improving the phase stability of variants of Ni-Al-Mo + X, and much specific information has been gathered in this area and is detailed in the alloy design section, a second effort has branched out into

modification of a series of strong conventional alloys for LAYERGLAZE fabricability. These modifications are aimed at producing moderate strength improvements in these alloys, along with more significant improvements in low cycle fatigue resistance as a result of microstructural improvements through LAYERGLAZE processing.

### 5. Structure of As-Layerglaze Fabricated Alloys

The microstructure of the 6.45 cm (2.54 in.) diameter disk (disk 1-8, Figs. 18-21) fabricated from alloy 8-12-3 as described previously in this report were examined in some detail. For convenience, the nomenclature used to describe the orientation of the metallographic samples prepared from this disk are those of a cylindrical coordinate system, referred to the external disk geometry (Fig. 42). The microstructure of disk 1-8 was examined by sectioning it parallel to the r, z, and  $\theta$  faces (Figs. 43-52). This revealed that solidification occurred by dendritic growth in all areas, with little or no observable side branching (Fig. 44). Some interdendritic phase(s) could be observed at 1000X, which indicated a greater degree of segregation and a lower cooling rate than had been expected (Ref. 24). On the z and  $\theta$  faces, photomicrographs taken at positions of increasing radius did not reveal any change in grain shape or size from near the disk substrate to its outer surface. The grains were markedly elongated in a direction parallel to the disk radius due to successive epi-taxial solidification as each layer was deposited. The mean grain boundary spacing measured along a line perpendicular to the disk radius was 55  $\mu\text{m}$  (~0.002 in.) on both the  $\theta$  and z faces. The observed grain lengths in the radial direction ranges from 127 to 1020  $\mu\text{m}$  (0.005 to 0.040 in.) with a mean of 660  $\mu\text{m}$  (0.026 in.). Striations were visible on the z and  $\theta$  faces (Figs. 45-52) which marked the position of the solid-liquid interface when each successive layer of metal was deposited. The distance between striations (~70-113  $\mu\text{m}$ , 0.0028-0.0045 in., Table VIII) is the thickness of each deposit which was not remelted during the deposition of the next layer. The mean spacing of the secondary dendrite arms, both near the disk substrate and near its outer surface, was 1.9  $\mu\text{m}$  ( $7.5 \times 10^{-5}$  in.), while the mean primary dendrite spacing measured at these same locations was 3.8  $\mu\text{m}$  ( $1.5 \times 10^{-4}$  in.). Comparison of these data with published observations of dendrite secondary arm spacings in nickel base superalloys as a function of solidification rate (Ref. 24) suggest that disk 1-8 solidified at ~ $10^4$  °C/s throughout its fabrication.

The microstructures of the disks subsequently fabricated by the powder-feed LAYERGLAZE process under the conditions described in "Experimental Processing, Section D", was in all cases very similar to that of disk 1-8 (alloy 8-12-3). For example, the composition of disk 11-2 (alloy 11-12-0-0-5) involved an increase in aluminum and the substitution of chromium for tantalum with respect to disk 1-8. Nevertheless, no change in dendrite spacing or in

the size and shape of the grains was observed (Figs. 53-55). Disk 9-1 (alloy 12-15; 12 a/o Al, 15 a/o Mo, Bal Ni) had a grain structure which was virtually indistinguishable from that of disks 1-8 and 11-2 (Fig. 56), but displayed a dendritic structure which was finer by a factor of ~1.5; a mean dendrite secondary arm spacing of  $1.3\mu\text{m}$  ( $5.2 \times 10^{-5}$  in.) and a mean primary dendrite spacing of  $2.5\mu\text{m}$  ( $9.8 \times 10^{-5}$  in.) (Figs. 57,58). The processing parameters for disk 9-1 were those used for all disk fabrication. It appears probable that the finer dendrite spacing was caused by the difference in alloy composition, as has been observed in other rapidly solidified nickel base superalloys (Ref. 25), rather than by an increase in solidification rate.

Some widely-spaced porosity and inclusions were observed in the microstructure of the as-Layerglazed disks. In disk 1-8, electron microprobe examination revealed that these microstructural anomalies were usually inclusions, presumably spheroidized by partial or complete melting by the laser beam. None were observed to have a diameter greater than  $25\mu\text{m}$  (0.001 in.), or to be spaced more closely than 1.8 mm (0.07 in.). In disks 9-1 (alloy 12-15) and 11-12-0-0-10 (alloy 11-12-0-0-10), the powder appeared to contain ceramic inclusions of a larger size than encountered in disk 1-8. These were presumably introduced into the molten alloy as fragments of crucible prior to or during atomization. They were usually lenticular in shape when observed in the as-Layerglazed microstructure. Electron microprobe analysis of one such inclusion observed in disk 9-1 revealed that it was predominantly aluminum oxide, with some calcium present as well (Fig. 59). It is probable that the inclusion size and quantity in Layerglazed material can be substantially reduced by standard procedures to reduce the inclusion content of atomized nickel base superalloys, such as filtering as a liquid and sieving to fine powder sizes.

In order to obtain a more detailed characterization of the fine dendritic microstructure which resulted from LAYERGLAZE processing, several of the alloys which had been mechanically tested were also examined by transmission electron microscopy. The as-fabricated structure of disk 1-8 (alloy 8-12-3) shown in Fig. 60 contained several features which were found to be common to the other Layerglazed Ni-Al-Mo base alloys as well; (a) a dislocation network of relatively high density and uniform distribution, (b) sharply defined interdendritic subboundaries of  $<1^\circ$  misorientation, and (c) varying amounts of polycrystalline interdendritic precipitates. Figure 60 shows an area in disk 1-8 spanning three dendrites, through which extensive slip on {111} has occurred to accommodate the stresses imposed by thermal contraction during LAYERGLAZE processing. In some regions the dislocations are in poor contrast due to the change in lattice orientation across the interdendritic subboundaries. Qualitative analysis of several interdendritic precipitates in thin foils revealed that they were higher in molybdenum and tantalum relative to the center of the dendrites (Fig. 61). Similar segregation effects have been previously observed in rapidly-solidified powder particles of alloy MMT 143 (Ni-13 a/o Al-9 a/o Mo-2 a/o Ta)

when they possessed a dendritic structure (Ref. 26). Interdendritic phases similar to those shown here were identified in a chill cast specimen of alloy 8-12-3 to be predominantly  $(\text{Mo}, \text{Ta})_2\text{C}$  carbides. Attempts to achieve a similar determination for disk 1-8 (also alloy 8-12-3) both by X-ray diffraction analysis of the residue derived from electrolytic dissolution of the  $\gamma$  and  $\gamma'$  phases (Ref. 27), and by selected area and convergent beam diffraction from interdendritic precipitates in thin foils. However, the interplanar spacings thus determined could not be indexed as  $\text{M}_6\text{C}$ ,  $\text{Mo}_2\text{C}$ ,  $\text{NiMo}$ , or orthorhombic  $\text{Ni}_3\text{Mo}$ . Examination of the ratios of the interplanar spacing determined from such diffraction patterns could frequently be shown to have been produced by a lattice which was clearly not cubic and very unlikely to be HCP. This observation, together with the relatively low carbon content of disk 1-8 (Table VIII) strongly suggested that many of these interdendritic precipitates were not carbides.

The phase distributions across the width of the dendrites themselves was quite homogeneous. It consisted of a very fine dispersion of ordered FCC,  $\text{Ll}_2$ -structure  $\gamma'$  within a FCC,  $\gamma$  solid solution which was itself short range ordered (Fig. 62). The  $\gamma'$  morphology varied between "blocky" and cuboidal, which suggested a relatively high  $\gamma-\gamma'$  misfit and was consistent with the appearance of  $\gamma'$  in high-molybdenum nickel-base superalloys (Ref. 28). The [100]-zone axis selected area diffraction pattern obtained from the area shown in Fig. 62 contains, in addition to the intense  $\gamma$  and smaller, sharp  $\gamma'$  spots, relatively diffuse spots in the  $\{1\ 1/2\ 0\}$  positions produced by short range order (SRO) in the  $\gamma$  solid solution. Similar evidence of SRO has been frequently reported in rapidly-quenched Ni-Mo and Ni-Mo-Ta alloys (Refs. 29-32) and, in at least one instance, in a high-Mo, Ni-base superalloy (Ref. 33). The extremely small size of the  $\gamma'$  in this specimen was confirmed by forming a dark field image of the  $\gamma'$  (Fig. 63), which within the area shown was  $\leq 20$  nm in size. The still smaller areas of bright contrast in the dark field image formed by using an SRO spot probably represent a diffraction effect characteristic of a true SRO solid solution (Ref. 34), rather than the size in real space of LRO microdomains (Ref. 35). Nevertheless, they are indicative of the scale of the LRO  $\text{Ni}_x\text{Mo}$  ( $x = 2, 3$ , or  $4$ ) phases which will precipitate in the  $\gamma$  solid solution upon subsequent aging at temperatures between 600 and  $\sim 800^\circ\text{C}$ .

The as-fabricated microstructure of disk 9-4 (alloy 11-12-0-0-5, Ni-11 a/o Al-12 a/o Mo-5 a/o Cr) was, as stated previously, similar to that of disk 1-8 in its general characteristics (Fig. 64). Some differences were noted; for example, interdendritic subboundaries were less frequently observed. In addition, the intensity maxima at the  $1\ 1/2\ 0$  positions in [001]-zone-axis selected area diffraction patterns, indicative of short range order in the  $\gamma$  phase, were barely detectable in the as-Layerglazed specimens of this alloy, and were too weak to appear when printed (Fig. 64). However, there was a high density of uniformly distributed dislocations in all areas, as observed in disk 1-8, and extremely fine  $\gamma'$  was present throughout the dendritic structure (Fig. 65).

The TEM micrographs of disk 9-1 (alloy 12-15) (Figs. 66,67) reflected the smaller primary dendrite spacing previously observed by light microscopy (Figs. 57,58). A greater amount of fine polycrystalline interdendritic precipitation was also present, but not uniformly so throughout the microstructure. The short range order intensity maxima in [001] zone axis diffraction patterns were not as intense as those produced by disk 1-8 (Fig. 62). As in the other as-processed disks which were examined, very fine  $\gamma'$  ( $\leq 20$  nm in size) was homogeneously distributed throughout the specimens (Figs. 68,69).

## 6. Structure of Annealed Alloys

The low ductility of the axially-oriented tensile specimens from disk 1-8 (alloy 8-12-3) which were tested at  $704^{\circ}\text{C}$  ( $1300^{\circ}\text{F}$ ) suggested that the LAYERGLAZE-fabricable Ni-Al-Mo base alloys might be subject to an unforeseen and embrittling phase transformation at or near this temperature. Consequently, most of the alloys in this group which had been developed early in the program (Ref. 36) were annealed in the as-laser-processed condition at temperatures of from  $593\text{-}871^{\circ}\text{C}$  ( $1100\text{-}1600^{\circ}\text{F}$ ) and for times of from 32-500 hrs. Subsequent examination of these specimens revealed that all of the Ni-Al-Mo and Ni-Al-Mo-Ta alloys which could be LAYERGLAZE processed and which contained  $\geq 10$  a/o Mo were in fact embrittled by a cellular phase transformation. This nucleated only at grain boundaries and interdendritic subboundaries and grew rapidly into the grains. It appeared probable that at least one of the products of this transformation contained molybdenum, since the volume fraction of lamellar structure produced by it increased markedly as the % Mo in the alloys increased for a constant time and temperature of anneal. Representative microstructures characteristic of this cellular transformation are shown in Figs. 70 and 71. The variety of phases known to form by a cellular transformation in conventionally processed (Refs. 37-39) and in rapidly solidified and annealed (Ref. 40) nickel-base alloys made it very desirable to make a positive identification of the phases participating in this one. Examination of thin foils prepared from disk 1-8 (alloy 8-12-3) revealed that lamellar packets of cellular phase transformation products had nucleated on interdendritic boundaries with misorientations of  $\geq 5^{\circ}$  after an anneal of only 32 hrs at  $704^{\circ}\text{C}$  ( $1300^{\circ}\text{F}$ ) (Fig. 72). The amount of cellular phase transformation that had occurred in a particular region of observation varied considerably. Within the same thin foil, in some areas none could be observed within a region of  $\sim 100\mu\text{m}^2$ , while adjacent areas had been almost completely consumed (Fig. 73). Analysis of this predominantly lamellar microstructure by selected area diffraction and dark field imaging revealed that it consisted of alternating, single phase plates of  $\gamma'$  and orthorhombic  $\text{Ni}_3\text{Mo}$  (Figs. 74,76-80). The formation of  $\text{NiMo}$ , which might have been anticipated from the Ni-Mo binary phase diagram (Fig. 75), did not occur, presumably due to the rapid post-solidification cooling inherent in LAYERGLAZE processing. The interplanar spacings of these phases (Table XI) were measured from selected area diffraction patterns such as Fig. 76,

using the  $\gamma'$  spots of the untransformed areas ( $\gamma' a_0 = 3.62 \text{ \AA}$ ) to determine the camera constant for each pattern. The morphology (Figs. 78-80) and relative crystallographic orientation (Figs. 76-77) of the two phases which comprised the cellular transformation product was quite similar to the noncellular, untransformed  $\gamma$  + orthorhombic  $\text{Ni}_3\text{Mo}$  microstructures observed in Ni-25 a/o Mo alloys aged for extended times at 700-800°C (1292-1470°F) (Refs. 31,44). Determination of the chemical composition of these phases by analytical electron microscopy was incomplete at the time of this report, but the low solubility of aluminum in  $\text{Ni}_3\text{Mo}$  requires that the other (single) phase be  $\gamma'$  rather than  $\gamma$ .

Examination of the microstructure of disk 1-8 which had not transformed by a cellular reaction at 704 or 760°C showed that a homogeneous dispersion of fine precipitates had appeared throughout the  $\gamma$ . These were identified (Figs. 81,82) as the same  $\text{Ni}_x\text{Mo}$  intermetallic phases ( $x = 2, 3$ , or  $4$ ) observed in the  $\gamma$  phase of both Ni-Mo binary alloys and nickel-base superalloys with >3 a/o Mo (Refs. 16,33,45-47).  $\text{Ni}_2\text{Mo}$  (metastable,  $\text{Pt}_2\text{Mo}$ -structure) and  $\text{Ni}_3\text{Mo}$  (metastable,  $\text{DO}_{22}$ -structure) frequently occurred in the same area (Fig. 82), while  $\text{Ni}_4\text{Mo}$  (stable,  $\text{Dla}$ -structure) usually appeared alone (Fig. 81). Each of these  $\text{Ni}_x\text{Mo}$  phases were noticeably resistant to coarsening, in that they remained  $\leq 20 \text{ nm}$  in size after disk 1-8 (alloy 8-12-3) was annealed for 100 hrs at 760°C (1400°F).

Observations of extensive cellular phase transformation and of concurrent  $\text{Ni}_x\text{Mo}$  precipitation in the  $\gamma$  unaffected by it were also made in disk 9-1 (alloy 12-15), annealed for 200 hrs at 760°C (Fig. 83). The higher molybdenum content of this alloy, 3 a/o greater than disk 1-8, caused the cellular formation of platelike  $\gamma'$  and orthorhombic  $\text{Ni}_3\text{Mo}$  to proceed more rapidly and consume more of the specimen (Fig. 83). As in disk 1-8, a fine dispersion of  $\text{Ni}_2\text{Mo}$ ,  $\text{DO}_{22}$ -structure  $\text{Ni}_3\text{Mo}$ , and  $\text{Ni}_4\text{Mo}$  precipitated in all of the  $\gamma$  which had remained unaffected by this transformation (Fig. 83).

Several different elements were added to the Ni-Al-Mo and Ni-Al-Mo-X group of alloys in an attempt to prevent the embrittling cellular transformation previously described while preserving the capacity for crack-free LAYERGLAZE processing. The reported effectiveness of minor additions of hafnium, zirconium and/or boron in altering the grain boundary chemistry and phase morphology of nickel base superalloys (Ref. 48) did not extend to the elimination of cellular growth in any of the Ni-Al-Mo-X alloys to which they were added (Table V), as illustrated by the microstructure of alloy 10-12-3 + 0.1 a/o B after homogenization and aging (Fig. 85). Furthermore, the addition of these three elements, singly or in combination, often induced cracking during laser processing where none had been observed before (Table V).

Preliminary attempts to inhibit cellular transformations by the partial substitution of chromium for molybdenum in Ni-Al-Mo alloys proved successful. An extensive number of alloys of this type were laser weld crack tested (Table IV), and eventually three were found which could be LAYERGLAZE processed without cracking and which displayed no evidence of a cellular phase transformation after annealing at 760°C (1400°F) for 100 hrs. These contained 11 a/o Al; 12 a/o Mo; and 5, 10 or 12.5 a/o Cr. Unfortunately, both alloy 11-12-0-0-5 and alloy 11-12-0-0-10 exhibited unacceptably low strength at 704°C (1300°F) in the as-Layerglazed condition (Table X). Moreover, alloy 11-12-0-0-10 proved to be unstable with respect to the precipitation of sigma and a TCP phase tentatively identified as P within its grains when annealed at 760°C. These phases reduced the ductility to virtually zero in tensile tests. Consequently, further exploration of Ni-Al-Mo-Cr alloys was terminated.

The high dislocation density observed in all as-Layerglazed alloys suggested that they might recrystallize when annealed above the  $\gamma'$  solvus temperature. This proved to be the case, and provides the opportunity for grain structure refinement should this seem desirable. An example of recrystallized grain structure in disk 1-8 (alloy 8-12-3) annealed for 30 min at 1240°C (2264°F) is shown by Fig. 86. Unfortunately, in no case did the homogenization of a disk during a recrystallization anneal prevent its subsequent embrittlement by the previously-described cellular transformation upon subsequent annealing at 760°C (1400°F).

## DISCUSSION

## A. Cracking During Laser Processing

The predominantly intergranular fusion zone cracking observed in many of the laser welded nickel base superalloys investigated here (Tables II-VI) appears to be similar to the "microfissuring" phenomena observed and described previously (Refs. 19-21). Furthermore, the reduction in cracking observed in modified-conventional alloys after the removal of Ti, B, Hf, etc. (Table VI) suggests that these elements promote a reduction of the local solidus temperature at grain boundaries (Ref. 21), and thus reduce high-temperature ductility. If this mechanism is valid, it follows that the  $\sim 10^4$  °C/s cooling rates associated with the LAYER-GLAZE process do not suppress this local melting point depression. Molybdenum presumably exerts a powerful influence upon grain boundary composition in all of the alloys to which it was deliberately added, but the specific mechanism(s) by which it inhibits fusion zone cracking when present in an empirically determined range of composition remains unknown.

It did not prove possible to laser process any alloy which contained a  $\gamma'$  volume fraction greater than 25-30%. Consequently, additional precipitation strengthening was sought via the formation of Ni<sub>4</sub>Mo and D0<sub>22</sub>-structure Ni<sub>3</sub>Mo in the  $\gamma$ , as suggested by previous investigations (Refs. 49,50). This type of transformation did indeed occur and appeared to have good potential for significant additional strengthening. However, most alloys which contained sufficient molybdenum to prevent laser weld cracking also were embrittled by a cellular transformation to  $\gamma' +$  orthorhombic Ni<sub>3</sub>Mo. This problem was never successfully resolved during this investigation. If it proves true that molybdenum is essential for the simultaneous requirements of laser processability and very high strength, the answer may lie in the direction of Ni-Al-Mo-Ta alloys with lower Mo contents, or extensively modified conventional disk superalloys which are less prone to cellular transformations. Verification of these concepts will be sought under the sponsorship of the Naval Air Systems Command.

## RESULTS AND CONCLUSIONS

### A. Processing

1. A LAYERGLAZE processing apparatus capable of producing fabricated parts of sizes in excess of the contract goal of 12.7 cm diameter has been fabricated, tested, and utilized to produce such parts for mechanical test evaluation.
2. A commercially available wire feeder has been adapted for the production of LAYERGLAZE parts using wire as a feedstock.
3. A simple, vibration/gravity controlled powder feeder has been designed, fabricated, and successfully used in the production of LAYERGLAZE parts using powder as a feedstock.
4. Critical parameters have been defined for both wire fed and powder fed LAYERGLAZE processing. Important criteria are:
  - a. Beam energy distribution
  - b. Beam power density and power
  - c. Feedstock mass flow rate
  - d. Continuity (smoothness) of deposition
  - e. Spatial location of feedstock impingement point relative to beam
  - f. Angle of feedstock at interaction point.
5. "First Order" optimized parameters used for production of LAYERGLAZE test parts were:
  - a. An unstable resonator optical beam.
  - b.  $0.78 \times 10^5 \text{ W/cm}^2$  at the interaction zone (6.0 kW).
  - c. 0.10-0.20 gm/sec deposition rate was achieved using powder which corresponds to a volumetric deposition rate of 0.04-0.08 cu in/min. Using wire feed deposition rates of up to 0.180 cu in. per min were achieved at 6.0 kW.
  - d. Fine deposition increments preferred - establishing powder feed as being highly preferable to wire feed.
  - e. Feedstock must impact mandrel within two feedstock diameters of the edge of the beam impingement point.
  - f. Feedstock angle should approximate 30°.
6. The effects of power density on fusion zone shape were documented experimentally.
7. Specific geometrical operating parameters for both wire feed and powder feed, including rotation speed and crossfeed rate were determined.

8. Additional major advantages for powder feed were identified in terms of the program as follows:

- a. Powder feedstock is easier to manufacture and thus can be more rapidly obtained, facilitating program iterations
- b. Laser coupling efficiency with powder feed is substantially higher than with wire feed.

9. Powder size fractions between -170 and +500 mesh are required for the present fabrication process. Powder flow rate is not in direct proportion to nozzle cross sectional area due to flow friction and boundary layer effects.

10. A LAYERGLAZE buildup in the form of a ring with a cross section of approximately 1.9 x 2.5 cm and an inner diameter of 3.8 cm was LAYERGLAZE fabricated with powder feed from alloy 8-12-3 with good structure and excellent integrity, as demonstrated by mechanical tests. This sample showed a strong tendency for epitaxial growth, to the point of approximating a layered, radial directionally solidified structure.

11. A full size LAYERGLAZE disk preform 13.2 cm in diameter ~3 cm thick was successfully fabricated from alloy 8-12-3 and IN-718. The structural integrity of the 8-12-3 portion was good, while the IN-718 contained internal cracks. This successfully demonstrated the powder feed LAYERGLAZE process capability to produce a disk of such size as is needed to meet program goals.

#### B. Alloy Design and Development

12. The complete absence of cracking after bead-on-plate laser welding with overlapping fusion zones has proved to be a sufficient criterion for the compatibility of an alloy with the LAYERGLAZE Process.

13. Several superalloys based on the Ni-Al-Mo system have been shown to be both laser weldable and stronger than conventional, weldable nickel base superalloys.

14. Alloy 8-12-3, composed of Ni-8 a/o Al-12 a/o Mo-3 a/o Ta, has been used to fabricate a disk-shaped consolidated part by the LAYERGLAZE process using powder feed. This disk possessed a dendritic microstructure of elongated grains indicative of a radially uniform solidification rate of  $\sim 10^4$  °C/s. Disks with similar microstructures were LAYERGLAZE fabricated from alloys 12-15, 11-12-0-0-5 and 11-12-0-0-10.

15. The mean 0.2% offset yield strength and LAYERGLAZE fabricated 8-12-3 at room temperature was 1044 MPa (151,000 psi). The mean UTS was 1288 MPa (187,000 psi) and the mean percent elongation was 28.8%. At 704°C (1300°F), elongation was only 2.4% along the disk axis and the UTS was reduced to 722 MPa (105,000 psi). UTS in the radial direction at 704°C was 1124 MPa (163,000 psi) with 31.5% elongation. Somewhat higher strengths but unacceptably low ductility were obtained in as-LAYERGLAZED alloys 12-15 (Ni-12 a/o Al-15 a/o Mo), 11-12-0-0-5 (Ni-11 a/o Al-12 a/o Mo-5 a/o Cr), and 11-12-0-0-10 (Ni-11 a/o Al-12 a/o Mo-10 a/o Cr).

16. The small dendritic spacing, high dislocation density, and small inclusion content of all alloys consolidated by the LAYERGLAZE Process suggest that considerable potential exists for improved chemical homogeneity and beneficial grain refinement by means of a brief, high-temperature anneal. To demonstrate this, as-LAYERGLAZED alloy 8-12-3 was recrystallized by annealing at 1240°C (2264°F) for 30 min.

17. The strengthening mechanism of LAYERGLAZE Processed Ni-Al-Mo and Ni-Al-Mo-Ta alloys has been studied. These alloys are strengthened at temperatures at or below 800°C by a combination of small (<300Å) γ' precipitates and a very fine dispersion of Ni<sub>2</sub>Mo, metastable, D0<sub>22</sub>-structure Ni<sub>3</sub>Mo and/or D1a-structure Ni<sub>4</sub>Mo particles. The D0<sub>22</sub>-structure Ni<sub>3</sub>Mo is very resistant to coarsening and to transformation to equilibrium orthorhombic Ni<sub>3</sub>Mo. It is, however, consumed when the γ → γ' + Ni<sub>3</sub>Mo cellular reaction sweeps through the γ matrix in which it has precipitated. The existence of this latter group of Ni<sub>x</sub>Mo precipitates provides these alloys with significant post-fabrication age-hardening potential.

18. It was found that most of the alloys in the Ni-Al-Mo and Ni-Al-Mo-X systems which can be LAYERGLAZE Processed without cracking also undergo an embrittling cellular phase transformation when annealed at 600-800°C for >30 hrs. In alloy 8-12-3 (Ni-8 a/o Al-12 a/o Mo-3 a/o Ta), this transformation has been identified as: γ → γ' + Ni<sub>3</sub>Mo (orthorhombic).

19. Additions of 1-4 a/o Re or 1-4 a/o V to LAYERGLAZE processable Ni-Al-Mo alloys do not inhibit the cellular transformation described above.

20. Additions of 0.5 a/o Hf, 0.5 a/o Zr, and/or 0.1 a/o B, used to increase creep ductility in conventional nickel-base superalloys, do not inhibit intermediate temperature cellular transformations when added to LAYERGLAZE Processable Ni-Al-Mo alloys. In many cases, these additions induce cracking during laser processing when none was observed without them.

21. Simultaneous reduction of the Al and/or Mo contents of Ni-Al-Mo and Ni-Al-Mo-Ta alloys (e.g. 8-12-3 → 8-10-1) produces alloys which can typically be LAYERGLAZE processed without cracking. Investigation of the strength and phase stability of these alloys will be the subject of a future investigation. Adequate strength and ductility must be maintained after annealing at 704-760°C in order for the alloy to be suitable for turbine disk applications.

22. Conventional disk alloys such as Waspaloy, Astroloy, Rene 95 and AF 115 have undergone preliminary evaluation for suitability for rapid solidification laser processing. These alloys have shown very favorable resistance to weld cracking and good intermediate temperature phase stability when extensively modified in one or more of the following three ways:

- a. Elimination of Hf, B and Zr
- b. Increased Mo content or substitution of Mo for Cr
- c. Reduction of C to trace levels (no deliberate additions of C),
- d. Elimination of Ti.

23. It has been learned that at least two conventional, medium strength superalloys, Udiment 630 and IN 903 are laser processable and phase stable at 760°C without any modifications.

#### C. Spin Test Design

24. Design of a disk configuration for spin test was completed based on IN 100/PWA 1074 material properties. (A copy of the drawing is attached as part of Appendix B.)

25. A spin arbor (STF 95813) was detailed and assembly/balance layout STL 209 was prepared. Both drawings are attached in Appendix B.

26. Spin arbor material was ordered and received. A request has been made to store this material in anticipation of a future spin test in a follow-on program.

REFERENCES

1. Breinan, E. M., C. M. Banas and B. H. Kear: Laser Skin Melting ASM Conference on Laser Surface Treatment for Automotive Applications, Detroit, MI, Feb. 17, 1976.
2. Breinan, E. M. and B. H. Kear: Surface Treatment of Superalloys by Laser Skin Melting, Superalloys, Metallurgy and Manufacture, Proceedings Third International Symposium, Claitors Publishing Div., Baton Rouge, LA, p 434 (1976).
3. Breinan, E. M., B. H. Kear and C. M. Banas: Processing Materials with Lasers, Physics Today, p. 44, Nov. 1976.
4. Breinan, E. M., B. H. Kear, L. E. Greenwald and C. M. Banas: Laser Glazing--A New Process for Production and Control of Rapidly-Chilled Metallurgical Microstructures, Society of Manufacturing Engineers Paper #MR76-867, Society of Manufacturing Engineers, Dearborn, MI, Dec. 2, 1976.
5. Walsh, J. L., E. M. Breinan and P. Gumz: Suppression of  $\gamma'$  Precipitation in a Laser-Melted Nickel Base Alloy, Proceedings 8th International Conference on X-ray Optics and Microanalysis, and 35th Electron Microscopy Society of America, Boston, MA, Aug. 1977.
6. Kear, B. H. and E. M. Breinan: Laser Glazing, A New Process for Production and Control of Rapidly-Chilled Metallurgical Microstructures, Proceedings Sheffield International Conference on Solidification and Casting, Ranmoor House, Sheffield Univ., July 1977.
7. Breinan, E. M. and B. H. Kear: Welding With High Power Lasers: Proceedings, 25th Sagamore Army Materials Research Conference, Bolton Landing, NY, July 17-21, 1978.
8. Kear, B. H. and E. M. Breinan: Laser Processing of Materials, ibid.
9. Breinan, E. M.: Laser Materials Processing, McGraw-Hill Yearbook of Science and Technology, McGraw-Hill Book Co., New York, NY, 1978.
10. Breinan, E. M. and B. H. Kear: Rapid Solidification Laser Processing of Materials for Control of Microstructure and Properties: Proceedings Conference on Rapid Solidification Processing at Reston, VA, Claitors Publishing Div., Baton Rouge, LA, pp 87-103 (1978).

11. Kear, B. H., E. M. Breinan and L. E. Greenwald: Laser Glazing--A New Process for Production and Control of Rapidly Chilled Metallurgical Microstructures, The Metals Society, London, England, Publication #192 Solidification and Casting.
12. Greenwald, L. E., E. M. Breinan and B. H. Kear: Heat Transfer Properties and Microstructure of Laser Melted Alloys, Proceedings of the 1978 Annual Meeting of the Materials Research Society Symposium H - Laser Solid Interactions, Boston, MA, Nov. 15, 1978.
13. Breinan, E. M., E. R. Thompson, C. M. Banas and B. H. Kear: Assessment of Advanced Laser Materials Processing Technology, Report No. R77-912887-3, Final Report, Contract N00014-77-C-0418, UTRC, East Hartford, CT 06108, Nov. 30, 1977.
14. Lemkey, F. D.: Superalloys: Metallurgy and Manufacture, B. H. Kear, D. R. Muzyka, J. K. Tien, and S. T. Wlodek, eds., Claitor's Publishing Div., Baton Rouge, LA, 1976, p 321.
15. Pearson, D. D.: Proc. Conf. In-Situ Composites-II, J. L. Walter, M. F. X. Gigliotti, B. F. Oliver and H. Bibring, eds., Ginn Custom Publishing, Lexington, MA, 1979.
16. Aigeltinger, E. H., S. R. Bates, R. W. Gould, J. J. Hren, and F. N. Rhines: Rapid Solidification Processing, Principles and Technologies, R. Mehrabian, B. H. Kear and M. Cohen, eds., Claitor's Publishing Div., Baton Rouge, 1978, p 291.
17. Snow, D. B. and E. M. Breinan: Applications of Lasers in Materials Processing, E. A. Metzbower, ed., American Society for Metals, Metals Park, OH, 1979, p 229.
18. Plummer, W. A.: A.I.P. Conf. Proc.: Thermal Expansion-1973, R. E. Taylor and G. L. Denman, eds., Plenum Press, NY, 1973, p 147.
19. Prager, M. and C. S. Shira: Welding Research Council, Bulletin No. 128, Feb. 1968.
20. Yeniscavich, W.: The Superalloys, C. T. Sims and W. C. Hagel, eds., John Wiley & Sons, New York, 1972, p 509.
21. Adam, P.: High Temperature Alloys for Gas Turbines, D. Coutsouradis, P. Felix, H. Fischmeister, L. Habraken, Y. Lindblom, and M. O. Speidel, eds., Applied Science Publishers, Ltd., London, 1978, p 737.

22. Smith, D. H., E. H. Chatworthy, D. G. Tipton, and W. L. Mankins: Superalloys 1980, J. K. Tien, S. T. Wlodek, H. Morrow III, M. Gell, and G. E. Maurer, eds., American Society for Metals, Metals Park, OH, 1980, p 521.
23. King, W. H. and D. W. Anderson: Technical Report AFML-TR-78-177, AFML/LLS, Wright-Patterson AFB, OH, Dec. 31, 1978.
24. Mehrabian, R.: Rapid Solidification Processing, Principles and Technologies, R. Mehrabian, B. H. Kear and M. Cohen, eds., Claitor's Publishing Div., Baton Rouge, 1978, p 9.
25. Holiday, P. R., A. R. Cox and R. J. Patterson II: Rapid Solidification Processing, Principles and Technologies, R. Mehrabian, B. H. Kear and M. Cohen, eds., Claitor's Publishing Div., Baton Rouge, 1978, p 246.
26. Field, R. D., E. H. Aigeltinger, and H. L. Fraser: Rapid Solidification Processing, Principles and Technologies, II, R. Mehrabian, B. H. Kear and M. Cohen, eds., Claitor's Publishing Div. Baton Rouge, 1980, p 93.
27. Donachie, M. J. and O. H. Krieger: J. Materials, JMLSA, 7, 269-278 (1972).
28. Loomis, W. T., J. W. Freeman and D. L. Sponseller: Met. Trans, 3, 989-1000 (1972).
29. Ruedl, E., P. Delavignette, and S. Amelinckx: Phys. Stat. Sol., 28, 305 (1968).
30. Okamoto, P. R. and G. Thomas: Acta Met., 19, 825-41 (1971).
31. van Tendeloo, G., R. DeRidder and S. Amelinckx: Phys. Stat. Sol., (a)27, 457-68 (1975).
32. Yamamoto, M., F. Shohno, and S. Nenno: Trans. JIM, 19, 475-82 (1978).
33. Ruedl, E.: Mat. Res. Bull., 10, 1267-1272 (1975).
34. Chevalier, J. P. and W. M. Stobbs: Acta Met., 27, 1197-1217 (1979).
35. Thomas, G. and R. Sinclair: Acta Met., 25, 231-234 (1977).
36. Breinan, E. M., C. O. Brown and D. B. Snow: UTRC Technical Report R79-914346-4, First Annual Report under Contract N00014-78-C-0387, Aug. 1979.
37. Smidoda, K., W. Gottschalk, and H. Gleiter: Acta Met., 26, 1833-36 (1978).

38. Barlow, C. Y. and B. Ralph: J. Mat. Sci., 14, 2500-2508 (1979).
39. Gust, W., T. Nguyen-Tat, and B. Predel: Z. Metallkde., 70, 241-46 (1979).
40. Wood, J. V., P. F. Mills, J. K. Bingham, and J. V. Bee: Met. Trans A, 10A, 575-84 (1979).
41. Hansen, M.: Constitution of Binary Alloys, McGraw-Hill, New York, 1958. p 968.
42. Elliott, R. P.: Constitution of Binary Alloys, First Supplement, McGraw-Hill, New York, 1965, p 622.
43. Pearson, W. B.: Handbook of Lattice Spacings and Structures of Metals, Vol. II, Pergamon Press, New York, 1967, p 321.
44. Yamamoto, M., S. Nenno, T. Saburi and Y. Mizutani: Trans. JIM, 11, 120-126 (1970).
45. Tawancy, H. M.: Met. Trans. A, 11A, 1764-65 (1980).
46. Martin, P. L., H. A. Lipsitt, and J. C. Williams: Rapid Solidification Processing, Principles and Technologies II, R. Mehrabian, B. H. Kear, and M. Cohen, eds., Claitor's Publishing Div., Baton Rouge, 1980, p 123.
47. Nemoto, M., T. Honda, Y. G. Nakagawa, Y. Saiga, and H. Suto: Trans. JIM 21, 495-504 (1980).
48. Dunn, R. G., D. L. Sponseller and J. M. Dahl: Proc. Symposium on Toward Improved Ductility and Toughness, Kyoto, 1971, p 319.
49. Spruiell, J. E., L. M. Ruch and C. R. Brooks: Met. Trans. A, 6A, 1301-5 (1975).
50. Goodrum, J. W. and B. G. Lefevre: Met. Trans. A, 8A, 939-43 (1977).

Table I

## LAYERGLAZE Operating Parameters

Parameter	NOL	Cross-Flow		Unstable Resonator
		Initial	Final	
Beam	Gaussian			
Power - kW	8	6	5	
Focal Length - cm	45.7	45.7	45.7	
Molten Pool Size - mm	2.54	1.0	3.175	
Power/Area=ω/cm <sup>2</sup>	0.16 x 10 <sup>5</sup>	0.76 x 10 <sup>5</sup>	0.63 x 10 <sup>5</sup>	
Wire Size - mm	0.9	0.9	0.9	
Wire Speed-cm/sec	2.1-7	7	.64-1.5	
Arbor Surface Speed - cm/sec	5	2.1-7	2.1-17 (4.2 typ)	
Advance Rate - mm/rev	0.76	0.5	1.44	

Table II

Composition and Weld Cracking Response  
Ni-Al-Mo Alloys

<u>Alloy Identification</u>	<u>Fusion Zone Cracking</u>			<u>Composition At % (Wt %)</u>		
	<u>None</u>	<u>Some</u>	<u>Extensive</u>	<u>Ni</u>	<u>Al</u>	<u>Mo</u>
2-28	X			70(60.00)	2(0.79)	28(39.21)
4-25	X			71(62.45)	4(1.62)	25(35.93)
4-28	X			68(58.83)	4(1.59)	28(39.58)
5-25	X			70(61.86)	5(2.03)	25(36.11)
5-28			X	67(58.23)	5(2.00)	28(39.77)
6-25	X			69(61.27)	6(2.45)	25(36.28)
6-28			X	66(57.64)	6(2.41)	28(39.96)
9-26			X	65(58.23)	9(3.71)	26(38.06)
9-28			X	63(55.81)	9(3.66)	28(40.53)
9.6-25.1			X	65.31(59.0)	9.63(4.0)	25.06(37.0)
10-11		X		79(77.78)	10(4.52)	11(17.70)
10-12	X			78(76.32)	10(4.50)	12(19.18)
10-13	X			77(74.87)	13(4.47)	13(20.66)
10-14	X			76(73.45)	10(4.44)	14(22.11)
10-15	X			75(72.04)	10(4.41)	15(23.55)
11-11		X		78(77.20)	11(5.00)	11(17.79)
11-12		X		77(75.74)	11(4.97)	12(19.29)
11-13	X			76(74.29)	11(4.94)	13(20.77)
11-14	X			75(72.86)	11(4.91)	14(22.23)
11-15	X			74(71.45)	11(4.88)	15(23.67)
11-16	X			73(70.06)	11(4.85)	16(25.09)
12-11			X	77(76.62)	12(5.49)	11(17.89)
12-12		X		76(75.16)	12(5.45)	12(19.39)
12-13	X			75(73.70)	12(5.42)	13(20.88)
12-14	X			74(72.27)	12(5.39)	14(22.34)
12-15		X		73(70.86)	12(5.35)	15(23.79)
12-16			X	72(69.46)	12(5.32)	16(25.22)
13-11			X	76(76.04)	13(5.98)	11(17.98)
13-12		X		75(74.56)	13(5.94)	12(19.50)
13-13	X			74(73.11)	13(5.90)	13(20.99)
13-14		X		73(71.67)	13(5.87)	14(22.46)
13-15			X	72(70.25)	13(5.83)	15(23.92)
13-16			X	71(68.85)	13(5.79)	16(25.36)
13-21			X	66(62.08)	13(5.62)	21(32.29)
13-22			X	65(60.79)	13(5.59)	22(33.62)
13-24			X	63(58.23)	13(5.52)	24(36.25)
14-9			X	77(78.46)	14(6.56)	9(14.98)
14-11			X	75(75.45)	14(6.47)	11(18.08)
14-13			X	73(72.51)	14(6.39)	13(21.10)
14-14			X	72(71.07)	14(6.35)	14(22.58)
14-15			X	71(69.65)	14(6.31)	15(24.04)

Table III

**Composition and Weld Cracking Response  
Ni-Al-Mo-Ta Alloys**

<u>Alloy Identification</u>	<u>Fusion Zone Cracking</u>			<u>Composition At % (Wt %)</u>			
	<u>None</u>	<u>Slight</u>	<u>Substantial</u>	<u>Ni</u>	<u>Al</u>	<u>Mo</u>	<u>Ta</u>
6-6-3		X		85(79.58)	6(2.58)	6(9.18)	3(8.66)
6-6-5			X	83(74.79)	6(2.49)	6(8.83)	5(13.89)
6-8-3	X			83(76.80)	6(2.55)	8(12.09)	3(8.56)
6-8-5	X			81(72.17)	6(2.46)	8(11.64)	5(13.73)
6-10-3	X			81(74.08)	6(2.52)	10(14.94)	3(8.46)
6-10-5	X			79(69.60)	6(2.43)	10(14.39)	5(13.58)
6-12-3	X			79(71.42)	6(2.49)	12(17.73)	3(8.36)
6-12-5	X			77(67.09)	6(2.40)	12(17.08)	5(13.43)
6-28-3			X	63(52.17)	6(2.28)	28(37.89)	3(7.66)
8-6-1	X			85(83.69)	8(3.62)	6(9.65)	1(3.04)
8-6-3			X	83(78.50)	8(3.48)	6(9.27)	3(8.75)
8-6-5			X	81(73.71)	8(3.35)	6(8.92)	5(14.02)
8-8-1	X			83(80.71)	8(3.58)	8(12.71)	1(3.00)
8-8-3			X	81(75.70)	8(3.44)	8(12.22)	3(8.64)
8-8-5			X	79(71.07)	8(3.31)	8(11.76)	5(13.86)
8-10-1	X			81(77.81)	8(3.53)	10(15.70)	1(2.96)
8-10-3		X		79(72.97)	8(3.40)	10(15.09)	3(8.54)
8-10-5			X	77(68.49)	8(3.27)	10(14.53)	5(13.71)
8-12-1	X			79(74.98)	8(3.49)	12(18.61)	1(2.92)
8-12-3	X			77(70.30)	8(3.36)	12(17.90)	3(8.44)
8-12-4	X			76(68.09)	8(3.29)	12(17.57)	4(11.05)
8-12-5	X			75(65.97)	8(3.23)	12(17.25)	5(13.55)
8-12-6			X	74(63.92)	8(3.18)	12(16.94)	6(15.97)
10-9.5-3			X	77.5(72.52)	10(4.30)	9.5(14.53)	3(8.65)
10-10.5-3		X		76.5(71.16)	10(4.28)	10.5(15.96)	3(8.60)
10-12-3	X			75(69.16)	10(4.24)	12(18.08)	3(8.52)
10-12-4			X	74(66.95)	10(4.16)	12(17.74)	4(11.15)
10-12-5			X	73(64.82)	10(4.08)	12(17.41)	5(13.68)
10-12-6			X	72(62.77)	10(4.01)	12(17.10)	6(16.12)
10-13-3		X		74(67.84)	10(4.21)	13(19.47)	3(8.48)
10-13-4			X	73(65.67)	10(4.13)	13(19.11)	4(11.09)
10-13-5			X	72(63.58)	10(4.06)	13(18.76)	5(13.61)
11-12-3		X		74(68.58)	11(4.68)	12(18.17)	3(8.57)
11-12-4			X	73(66.37)	11(4.60)	12(17.83)	4(11.21)
11-13-3		X		73(67.25)	11(4.66)	13(19.57)	3(8.52)
11-13-4			X	72(65.08)	11(4.57)	13(19.20)	4(11.14)

Table IV

Composition and Weld Cracking Response  
Ni-Al-Mo-Cr Alloys

Alloy Identification	Fusion Zone Cracking			Composition At % (Wt %)			
	None	Some	Extensive	Ni	Al	Mo	Cr
11-5-0-0-10			X	74(77.02)	11(5.26)	5(8.50)	10(9.22)
11-5-0-0-12		X		72(75.12)	11(5.27)	5(8.52)	12(11.09)
11-7-0-0-10			X	72(73.96)	11(5.19)	7(11.75)	10(9.10)
11-7-0-0-12		X		70(72.07)	11(5.20)	7(11.79)	12(10.94)
11-7-0-0-15		X		67(69.23)	11(5.22)	7(11.82)	15(13.73)
11-8-0-0-12			X	69(70.58)	11(5.17)	8(13.37)	12(10.87)
11-8-0-0-15		X		66(67.75)	11(5.19)	8(13.42)	15(13.64)
11-9-0-0-10		X		70(70.48)	11(5.13)	9(14.91)	10(8.98)
11-10-0-0-12		X		67(67.66)	11(5.11)	10(16.50)	12(10.73)
11-12-0-0-5	X			72(71.22)	11(5.00)	12(19.40)	5(4.38)
11-12-0-0-7.5			X	69.5(68.94)	11(5.02)	12(19.45)	7.5(6.59)
11-12-0-0-10	X			67(66.65)	11(5.03)	12(19.51)	10(8.81)
11-12-0-0-12.5	X			64.5(64.35)	11(5.04)	12(19.56)	12.5(11.05)
11-12-0-0-15			X	62(62.03)	11(5.06)	12(19.62)	15(13.29)
11-12-0-0-20			X	57(57.36)	11(5.09)	12(19.73)	20(17.82)
12-7-0-0-10			X	71(73.34)	12(5.70)	7(11.82)	10(9.15)
12-8-0-0-5			X	75(76.52)	12(5.63)	8(13.34)	5(4.52)
12-9-0-0-10			X	69(70.35)	12(5.62)	9(15.00)	10(9.03)
12-9-0-0-12			X	67(68.47)	12(5.64)	9(15.03)	12(10.86)
12-10-0-0-5			X	73(73.53)	12(5.56)	10(16.46)	5(4.46)
12-11-0-0-10		X		67(67.44)	12(5.55)	11(18.09)	10(8.92)
12-12-0-0-5		X		71(70.61)	12(5.49)	12(19.50)	5(4.40)
12-13-0-0-5			X	70(69.18)	12(5.45)	13(20.99)	5(4.38)
12-13-0-0-10			X	65(64.60)	12(5.48)	13(21.12)	10(8.80)
12-14-0-0-5			X	69(67.77)	12(5.42)	14(22.47)	5(4.35)
12-15-0-0-5			X	68(66.37)	12(5.38)	15(23.93)	5(4.32)
12-15-0-0-10			X	63(61.84)	12(5.41)	15(24.06)	10(8.69)
13-7-0-0-5			X	75(77.45)	13(6.17)	7(11.81)	5(4.57)
13-7-0-0-10			X	70(72.71)	13(6.21)	7(11.88)	10(9.20)
13-9-0-0-5			X	73(74.41)	13(6.09)	9(14.99)	5(4.51)
13-11-0-0-5			X	71(71.44)	13(6.01)	11(18.09)	5(4.46)
13-12-0-0-5			X	70(69.99)	13(5.97)	12(19.61)	5(4.43)
15-5-0-0-10			X	70(74.53)	15(7.34)	5(8.70)	10(9.43)

Table V

Composition and Weld Cracking Response  
Various Ni-Al-Mo Base Alloys

Alloy Identification	Fusion Zone Cracking		Composition At Z (Wt %)									
	None	Some Extensive	Ni	Al	Mo	Ta	Tl	Cr	Hf	Zr	B	V
11-12-0-0-0-0.5	X	X	76.5(74.50)	11(4.92)	12(19.10)			0.5(1.48)				
11-12-0-0-0-2	X	X	75(70.93)	11(4.78)	12(18.54)			2(5.75)				
11-12-0-0-5-0.5	X		71.5(70.02)	11(4.95)	12(19.20)			0.5(1.49)				
12-10 + 2 Re	X	X	76(72.94)	12(5.29)	10(15.68)			5(4.34)				
12-12 + 2 Re	X		74(70.16)	12(5.23)	12(18.59)							
12-13-0-0-0-0.5		X	74.5(72.49)	12(5.36)	13(20.67)			0.5(1.48)				
12-13-0-0-0-2		X	73(68.98)	12(5.21)	13(20.07)			2(5.74)				
12-13-0-0-0-4		X	71(64.59)	12(5.02)	13(19.33)			4(11.06)				
12-13 + 1 V	X		74(72.82)	12(5.43)	13(20.90)							1(0.85)
12-13 + B		X	74.9(73.67)	12(5.42)	13(20.89)							
12-13 + Zr		X	74.9(73.64)	12(5.43)	13(20.87)			0.05(0.076)				
12-13 + Zb		X	74.85(73.60)	12(5.42)	13(20.89)			0.05(0.076)				
12-13 + H2B		X	74.35(72.38)	12(5.37)	13(20.68)			0.1(0.018)				
12-15-0-0-0-0.5	X	X	72.5(69.68)		15(23.56)			0.5(1.46)				
12-15-0-0-0-2	X	X	71(66.29)	12(5.15)	15(22.88)			2(5.68)				
12-15 + 1 V	X		72(69.98)	12(5.36)	15(23.82)							
12-15 + B	X		72.9(70.81)	12(5.36)	15(23.81)							
13-9-0-0-0-2	X		76(73.96)	13(5.81)	9(14.31)			2(5.92)				
13-12-0-0-0-2	X		73(69.75)	13(5.71)	12(18.73)			2(5.81)				
14-13-0-0-0-2	X		71(67.78)	14(6.14)	13(20.28)			2(5.80)				
17-11-0-0-0-2	X		70(68.72)	17(7.67)	11(17.64)			2(5.97)				
8-12-0-3	X		77(74.95)	8(3.58)	12(19.09)							
8-12-1-5-1.5	X		77(72.55)	8(3.46)	12(18.48)			1.5(4.43)				
9.5-9.5-0-3.5	X		77.5(77.31)	9.5(4.35)	9.5(15.49)			1.5(1.15)				
8-9.5-1.5-0-5	X		76(72.90)	8(3.53)	9.5(14.89)			3(2.38)				
11-0-5-0-20	X		64(62.64)	11(4.95)				3.5(2.85)				
14-0-0-0-10	X		76(83.25)	14(7.05)				5(15.08)				
8-12-3 + 1 V	X		76(69.47)	8(3.36)	12(17.93)			5(4.25)				
8-12-3 + 3 V	X		74(67.81)	8(3.37)	12(17.97)			20(17.33)				
10-12-3 + 1 V	X		74(68.32)	10(4.24)	12(18.10)			10(9.70)				
10-12-3 + 3 V	X		72(66.63)	10(4.25)	12(18.15)							
10-12-3-0-0-0.5	X		74.5(68.05)	10(4.20)	12(17.91)			1(0.79)				
10-12-3 + B	X		74.90(69.11)	10(4.24)	12(18.10)			3(2.39)				
10-12-3 + Zr	X		74.95(69.09)	10(4.24)	12(18.08)			1(0.80)				
10-12-3 + Zb	X		74.35(69.05)	10(4.24)	12(18.09)			3(2.41)				
8-9-3-0-3	X		77(71.77)	8(3.43)	9(13.71)			0.5(1.39)				
8-10-3-0-3	X		76(70.42)	8(3.41)	10(15.14)			0.1(0.017)				
10-10-3-0-3	X		74(69.26)	10(4.30)	10(15.30)			0.05(0.072)				
10-12-3-0-3	X		72(66.60)	10(4.25)	12(18.14)			0.05(0.072)				

Table VI

Composition and Weld Cracking Response  
Conventional and Modified-Conventional Superalloys

Alloy Identification	Alloy	Fusion Zone Cracking				Composition, At % (Wt %)								Additional Elements				
		None	Some	Extensive	Ni	Al	Mo	Ta	Ti	Cr	Co	Fe	Nb	W	Hf	Zr	B	C
IN 100	X	56.28 (61.005)	11.04 (5.50)	1.69 (3.0)	5.37 (4.75)	9.89 (9.50)	13.78 (15.0)						0.95 (1.6)	0.25 (0.8)	0.04 (0.06)	0.08 (0.04)	0.77 (0.17)	1.06 (1.0)V
MERL 76	X	50.86 (54.0)	10.25 (5.0)	1.84 (3.2)	4.96 (4.3)	13.29 (12.5)	17.36 (18.5)						0.95 (1.6)	0.25 (0.8)	0.04 (0.06)	0.10 (0.02)	0.09 (0.02)	
MERL 76, Mod. A	X	51.67 (55.1)	10.20 (5.0)	1.84 (3.2)	4.94 (4.3)	13.24 (12.5)	17.28 (18.5)						0.83 (1.4)	0.25 (0.8)	0.04 (0.06)	0.10 (0.02)	0.09 (0.02)	
MERL 76, Mod. B	X	56.21 (59.4)	10.30 (5.0)	1.85 (3.2)	4.94 (4.3)	13.36 (12.5)	17.44 (18.5)						0.84 (1.4)	0.25 (0.8)	0.04 (0.06)	0.10 (0.02)	0.09 (0.02)	
AF2-1DA	X	57.86 (59.435)	4.74 (4.6)	1.79 (3.0)	0.47 (1.5)	3.58 (3.0)	13.19 (12.0)	9.70 (10.0)					1.86 (6.0)	0.06 (6.0)	0.08 (0.10)	0.08 (0.09)	1.67 (0.35)	
AF2-1DA, Mod. A	X	58.23 (54.335)	8.13 (3.5)	12.41 (19.0)	0.52 (1.5)	6.03 (5.0)	10.64 (10.0)						2.05 (6.0)	0.07 (0.10)	0.09 (0.09)	0.09 (0.09)	1.83 (0.35)	
AF2-1DA, Mod. B	X	59.11 (59.9)	9.88 (4.6)	1.81 (3.0)	0.48 (1.5)	3.63 (3.0)	13.37 (12.0)	9.83 (10.0)					1.89 (6.0)	0.07 (0.10)	0.09 (0.09)	0.09 (0.09)	1.83 (0.35)	
AF2-1DA, Mod. C	X	56.55 (57.74)	9.86 (4.6)	1.81 (3.0)	0.48 (1.5)	3.62 (3.0)	13.35 (12.0)	9.81 (10.0)					1.89 (6.0)	0.07 (0.10)	0.09 (0.09)	0.09 (0.09)	1.83 (0.35)	
AF2-1DA, Mod. D	X	59.62 (55.0)	8.25 (3.5)	12.60 (19.0)	0.53 (1.5)	6.12 (5.0)	10.80 (10.0)						2.08 (6.0)	0.07 (0.10)	0.09 (0.09)	0.09 (0.09)	2.63 (2.5)Mn	
AF 115	X	53.69 (53.78)	8.47 (3.9)	1.71 (2.8)	4.77 (3.9)	11.84 (10.5)	14.92 (15.0)						1.91 (6.0)	1.13 (1.8)	0.69 (2.1)	0.03 (0.05)	0.11 (0.11)	0.73 (0.15)
AF 115, Mod. A	X	65.32 (62.98)	8.80 (3.9)	12.06 (19.0)		5.85 (5.0)	5.17 (5.0)						1.18 (1.8)	0.72 (2.1)	0.03 (0.05)	0.11 (0.11)	0.76 (0.15)	
AF 115, Mod. B	X	66.64 (65.15)	8.68 (3.9)	11.89 (19.0)		5.78 (5.0)	5.10 (5.0)						1.16 (1.8)	0.72 (2.1)	0.03 (0.05)	0.11 (0.11)	0.76 (0.15)	
AF 115, Mod. C	X	55.58 (56.1)	8.41 (3.9)	1.70 (2.8)	4.73 (3.9)	11.75 (10.5)	14.80 (15.0)						1.90 (1.8)	1.13 (1.8)	0.03 (0.05)	0.11 (0.11)	0.76 (0.15)	
AF 115, Mod. D	X	53.02 (53.6)	8.39 (3.9)	1.69 (2.8)	4.73 (3.9)	11.73 (10.5)	14.78 (15.0)						1.89 (1.8)	1.13 (1.8)	0.03 (0.05)	0.11 (0.11)	0.76 (0.15)	
AF 115, Mod. E	X	64.51 (62.8)	8.72 (3.9)	11.94 (19.0)		5.80 (5.0)	5.12 (5.0)						6.00 (6.0)	1.17 (1.8)	0.03 (0.05)	0.11 (0.11)	0.76 (0.15)	
Rene 125	X	60.14 (59.29)	10.60 (4.8)	1.24 (2.0)	3.11 (3.8)	10.19 (2.5)	10.11 (8.9)						2.27 (7.0)	0.52 (1.55)	0.03 (0.05)	0.55 (0.11)		
Rene 95	X	60.07 (61.29)	7.46 (3.5)	2.10 (3.5)	3.0 (2.5)	15.49 (14.0)	7.81 (8.0)						1.10 (3.5)	2.17 (3.5)	0.03 (0.05)	0.05 (0.05)	0.72 (0.15)	
Rene 95, Mod. A	X	64.26 (60.79)	8.05 (3.5)	11.46 (18.0)	3.24 (2.5)	8.42 (8.0)							1.18 (3.5)	2.34 (3.5)	0.03 (0.05)	0.06 (0.05)	0.78 (0.15)	
Rene 95, Mod. B	Xq	66.52 (62.29)	8.13 (3.5)	12.42 (19.0)		8.51 (8.0)							1.19 (3.5)	2.36 (3.5)	0.03 (0.05)	0.06 (0.05)	0.78 (0.15)	
Rene 95, Mod. C	X	68.51 (65.79)	7.93 (3.5)	12.11 (19.0)		8.30 (8.0)							2.30 (3.5)	2.30 (3.5)	0.03 (0.05)	0.06 (0.05)	0.76 (0.15)	
Rene 95, Mod. D	X	69.08 (65.94)	7.98 (3.5)	12.18 (19.0)		8.35 (8.0)							2.32 (3.5)	2.32 (3.5)	0.03 (0.05)	0.06 (0.05)	0.76 (0.15)	
Rene 95, Mod. E	X	60.63 (61.5)	7.51 (3.5)	2.11 (3.5)	3.02 (2.5)	15.59 (14.0)	7.86 (8.0)						1.10 (3.5)	2.18 (3.5)	0.03 (0.05)	0.05 (0.05)	0.72 (0.15)	
Rene 95, Mod. F	X	58.07 (59.0)	7.49 (3.5)	2.11 (3.5)	3.02 (2.5)	15.56 (14.0)	7.84 (8.0)						1.10 (3.5)	2.18 (3.5)	0.03 (0.05)	0.05 (0.05)	0.78 (0.15)	
Rene 95, Mod. G	X	67.17 (62.5)	8.18 (3.5)	12.50 (19.0)		8.57 (8.0)							1.20 (3.5)	2.38 (3.5)	0.03 (0.05)	0.06 (0.05)	0.76 (0.15)	
Rene 95, Mod. H	X	64.37 (60.0)	8.17 (3.5)	12.47 (19.0)		8.55 (8.0)							1.20 (3.5)	2.37 (3.5)	0.03 (0.05)	0.06 (0.05)	0.76 (0.15)	

Alloy Identification	Fusion Zone Cracking		None		Some		Extensive		<u>Ni</u>		<u>Al</u>		<u>Mn</u>		<u>Ta</u>		<u>Ti</u>		<u>Cr</u>		<u>Co</u>		<u>Fe</u>		<u>W</u>		<u>Nb</u>		<u>Hf</u>		<u>Zr</u>		<u>B</u>		<u>C</u>		<u>Additional Elements</u>	
	None	Some	None	Some	None	Some	None	Some	None	Some	None	Some	None	Some	None	Some	None	Some	None	Some	None	Some	None	Some	None	Some	None	Some	None	Some	None	Some	None	Some				
Rene 62	X		47.12	2.7	5.46		3.06		16.8		21.16	10.81			23.47		1.41		(2.25)				0.03	0.43			(0.005)	0.03	0.43									
Rene 41	X		(47.5)	(1.25)	(9.0)		(2.5)		(15.0)		(3.1)	(19.0)	(11.0)																									
Rene 41, Mod. A	X		54.56	3.22	6.04		3.75		21.24	10.85																												
Rene 41, Mod. B	X		54.86	3.23	6.06		3.76		21.24	10.85																												
NX 188	X		52.29	3.23	6.05		3.76		21.20	10.83																												
NX 188	X		(52.9)	(1.5)	(10.0)		(3.1)		(19.0)	(11.0)																												
PWA 454	X		72.10	16.97	10.74		(73.96)	(8.0)	(18.0)																													
TRW VI A, Mod. A	X		64.66	11.26	4.03		1.90		11.68		5.15																											
TRW VI A, Mod. B	X		70.73	11.44	1.19		0.16		6.60		7.68		1.80		0.31																							
TRW VI A, Mod. C	X		64.62	(5.4)	(2.0)		(0.13)		(6.0)		(7.5)		(5.8)		(0.5)																							
MA6000E, Mod. A	X		66.03	6.87	5.15		3.03		1.27	7.03	8.18		1.92		0.33																							
MA6000E, Mod. B	X		(62.79)	(3.0)	(8.0)		(9.0)		1.01	(6.0)	(7.5)		(5.8)		(0.5)																							
MM 0011	X		67.67	9.50	1.89		0.63		2.97	16.42	1.24																											
MM 0011, Mod. A	X		(69.79)	(4.5)	(2.0)		(2.5)		(15.0)	(4.0)	1.24																											
MM 0011, Mod. B	X		(62.79)	(3.0)	(7.0)		(1.0)		1.27	7.01	8.16		1.92		0.33																							
Astroloy	X		60.85	12.18	0.44		0.99		1.25	9.54	10.14																											
Astroloy, Mod. A	X		(59.785)	(5.5)	(0.7)		(3.0)		(1.0)	(8.3)	(10.0)																											
Astroloy, Mod. B	X		65.53	7.96	0.45		1.02		9.80	10.41	3.34																											
Astroloy, Mod. C	X		(62.785)	(3.5)	(0.7)		(3.0)		(8.3)	(10.0)	(10.0)																											
Astroloy, Mod. D	X		56.4	8.34	8.04		1.07		10.27	10.91	3.30																											
Astroloy, Mod. E	X		(51.485)	(3.5)	(12.0)		(3.0)		(8.3)	(10.0)	(10.0)																											
Astroloy, Mod. F	X		53.46	9.02	3.03		4.04		15.95	14.07	3.25																											
Astroloy, Mod. G	X		(56.76)	(4.4)	(5.25)		(3.5)		(15.0)	(15.0)	(15.0)																											
Astroloy, Mod. H	X		52.11	8.24	3.07		4.06		16.03	16.03	0.03																											
Astroloy, Mod. I	X		(55.06)	(4.0)	(5.3)		(3.5)		(15.0)	(17.0)	(0.05)																											
Astroloy, Mod. J	X		51.18	8.32	3.10		4.10		16.18	16.18	0.47																											
Astroloy, Mod. K	X		(53.56)	(4.0)	(5.3)		(3.5)		(15.0)	(17.0)	(1.5)																											
Astroloy, Mod. L	X		51.31	8.33	3.10		4.10		16.20	16.20	0.47																											
Astroloy, Mod. M	X		52.58	8.48	5.96		4.04		16.49	16.49	0.47																											
Astroloy, Mod. N	X		(56.0)	(4.0)	(10.0)		(1.0)		(15.0)	(17.0)	(1.5)																											
Astroloy, Mod. O	X		51.84	9.05	3.04		4.05		16.01	16.01	0.47																											
Astroloy, Mod. P	X		(54.85)	(4.4)	(5.25)		(3.5)		(15.0)	(17.0)	(1.5)																											
Astroloy, Mod. Q	X		49.40	9.04	3.03		4.05		15.98	15.98	0.47																											
Astroloy, Mod. R	X		(52.35)	(4.4)	(5.25)		(3.5)		(15.0)	(17.0)	(1.5)																											
Astroloy, Mod. S	X		53.10	9.10	3.05		4.10		16.10	16.10	0.47																											
Astroloy, Mod. T	X		(55.85)	(4.4)	(5.25)		(3.5)		(15.0)	(17.0)	(1.5)																											
Astroloy, Mod. U	X		56.24	2.95	2.55		3.56		21.3	13.01	0.47																											
Wasalloy	X		(58.154)	(1.4)	(4.31)		(3.0)		(19.5)	(13.5)	(3.5)																											
Wasalloy, Mod. A	X		55.28	2.97	2.57		3.59		21.50	13.13	0.48																											
Wasalloy, Mod. B	X		(56.615)	(1.4)	(4.3)		(3.0)		(19.5)	(13.5)	(1.5)																											
Wasalloy, Mod. C	X		56.32	2.95	2.54		3.56		21.29	13.01	0.48																											
Wasalloy, Mod. D	X		(56.23)	(1.4)	(4.3)		(3.0)		(19.5)	(13.5)	(1.5)																											
Wasalloy, Mod. E	X		54.02	2.95	2.55		3.56		21.13	13.02	0.48																											
Wasalloy, Mod. F	X		(55.8)	(1.4)	(4.3)		(3.0)		(19.5)	(13.5)	(1.5)																											

Alloy Identification	Fusion Zone Cracking		<u>Ni</u>	<u>Al</u>	<u>Mo</u>	<u>Ta</u>	<u>Ti</u>	<u>C<sub>x</sub></u>	<u>Co</u>	<u>Fe</u>	<u>W</u>	<u>Nb</u>	<u>Hf</u>	<u>Zr</u>	<u>B</u>	<u>C</u>	Additional Elements
	<u>None</u>	<u>Some</u>															
IN 718	X		52.28 (52.96)	1.07 (0.5)	1.81 (3.0)		1.09 (0.9)	21.18 (19.0)									
IN 718, Mod. A	X		52.40 (53.0)	1.08 (0.5)	1.81 (3.0)		1.09 (0.9)	21.21 (19.0)									
IN 718, Mod. B	X		49.84 (50.5)	1.08 (0.5)	1.81 (3.0)		1.09 (0.9)	21.17 (19.0)									
PWA MMT 143	X		76.0 (73.90)	13.0 (5.81)	9.0 (14.30)	2.0 (5.99)											
PWA MMT 185	X		74.0 (72.65)	15.0 (6.77)	9.0 (14.44)												
NiTaC 13	X		64.63 (63.36)	11.99 (5.4)	2.68 (8.1)		5.07 (4.4)	3.35 (3.3)			1.0 (3.1)						
CoTaC	X		26.99 (25.0)		4.80 (13.7)		18.29 (15.0)	43.45 (40.4)			1.72 (5.0)						
CoTaC 3	X		10.28 (10.0)		4.07 (12.2)		23.23 (20.0)	58.40 (57.0)									
CoTaC 74	X		50.68 (50.5)	8.73 (4.0)			11.33 (10.0)	20.0 (20.0)			3.21 (10.0)	3.11 (4.9)					
CoTaC 741	X		59.48 (59.8)	10.82 (5.0)			11.23 (10.0)	9.91 (10.0)			3.18 (10.0)	2.95 (4.7)					
Udimet 630	X		50.69 (49.97)	1.10 (0.5)	1.86 (3.0)		1.24 (1.0)	20.62 (18.0)			19.20 (18.0)	0.97 (3.0)	4.17 (6.5)				
IN 901	X		44.19 (44.9)		3.61 (6.0)		3.14 (2.6)	13.89 (12.5)			35.17 (34.0)						
IN 903	X		38.11 (38.9)	1.49 (0.7)			1.68 (1.4)				14.64 (15.0)	42.22 (41.0)					
IN 903, Mod. A*	X		36.99 (38.0)	2.12 (1.0)			1.79 (1.5)	2.30 (3.0)			14.55 (15.0)	39.40 (38.5)					
IN 903, Mod. B	X		37.65 (38.0)				1.82 (1.5)				14.81 (15.0)	43.22 (41.5)					
IN 903, Mod. C	X		37.80 (38.0)				1.83 (1.5)				14.87 (15.0)	42.36 (40.5)					
IN 903, Mod. D	X		36.98 (38.0)	2.11 (1.0)			1.79 (1.5)	3.30 (3.0)			14.54 (15.0)	36.83 (36.0)					
IN 939	X		46.47 (48.24)	3.98 (1.9)			0.44 (1.4)	4.37 (3.7)			18.23 (19.0)	0.61 (2.0)					
AFC-6-7**	X		46.98 (48.5)	4.01 (1.9)			0.44 (1.4)	4.39 (3.7)			18.34 (19.0)	0.62 (2.0)					
IN 939, Mod. B	X		44.49 (46.0)	4.00 (1.9)			0.44 (1.4)	4.38 (3.7)			18.31 (19.0)	0.62 (2.0)					
			55.37 (55.365)	2.17 (1.0)			1.78 (5.5)	1.23 (1.0)			12.62 (12.0)	1.90 (3.0)					
			55.56 (55.5)	2.18 (1.0)			1.79 (5.5)	1.23 (1.0)			12.63 (12.0)	1.90 (3.0)					
AFC-4-6**	X		38.43 (57.365)	2.21 (1.0)			2.48 (7.5)	21.85 (19.0)			12.85 (12.0)	1.93 (3.0)					
AFC-4-6, Mod. A.	X		55.98 (55.0)	2.21 (1.0)			2.48 (7.5)	21.84 (19.0)			12.84 (12.0)	1.93 (3.0)					

Table VII  
Phase Transformation Temperatures

Alloy Identification	Ni	Composition, At. %				Cr	None	Some	Extensive	Laser Weld		Transformation Temperatures (°C)	
		Al	Mo	Ta	Ti					Liquidus (DTA)	Solidus (DTA)	Y' (DTA)	D022 Ni3Mo (DTE)
11-12	77	11	12				X			1388	1365	1140	912
12-11	77	12	11				X			1386	1363	1173	—**
12-12	76	12	12				X			1376	1354	1182	880
12-13	75	12	13				X			1377	1397*	1195	913
12-14	74	12	14				X			1372	1303*	1185	—
12-15	73	12	15				X			1365	1289*	1200	907
13-12	75	13	12				X			1377	1304*	1210	911
14-9	77	14	9				X			1391	1363	1218	—
14-11	75	14	11				X			1374	1305*	1232	—
14-13	73	14	13				X			1361	1304*	1234	908
NX 188	72.1	17	10.7				X			1355	1306	1281	
8-12-3	77	8	12	3			X			1372	1330	1197	810
10-9.5-3	77.5	10	9.5	3			X			1382	1353	1247	—
10-10.5-3	76.5	10	10.5	3			X			1375	1290*	1262	—
10-12-3	73	10	12	3			X			1361	1292*	1262	900
MMT 143	76	13	9	2						1374	1333	1300	770
11-7-0-0-15	67	11	7				15			1351	1319	1044	—
11-10-0-0-12	67	11	10				12			1335	1278*	1083	—
11-12-0-0-5	72	11	12				5			1366	1292*	1128	825
11-12-0-0-7.5	69.5	11	12				7.5			1382	1368	1195	—
11-12-0-0-10	67	11	12				10			1388	1282*	1100	—
11-12-0-0-12.5	64.5	11	12				12.5			1324	1274*	1094	—
12-8-0-0-5	75	12	8							1384	1367	1140	—
12-10-0-0-5	73	12	10				5			1370	1329	1145	74.9
12-11-0-0-10	67	12	11				10			1329	1278*	959	4.94
12-12-0-0-5	71	12	12				5			1353	1291*	1160	807
12-14-0-0-5	69	12	14				5			1342	1292*	1160	81.2
13-7-0-0-5	75	13	7				5			1378	1367	1160	—
15-5-0-0-10	70	15	5				10			1359	1327	1174	—
8-12-1.5-1.5	77	8	12	1.5				X		1374	1337	1180	—
8-12-0-3	77	8	12	3				X		1371	1334	1190	—
9.5-9.5-0-3.5	77.5	9.5	9.5	3.5				X		1371	1341	1242	—
11-0-5-0-20								X		1314	1250*	1207	—

\*Eutectic peak observed

\*\*Not determined

Table VIII

## Chemical Analyses, Experimental Ni-Al-Mo Base Superalloys

Alloy Identification	Processing History	Nominal Composition, At %						Observed Composition, At %										
		Ni	Al	Mo	Ta	Cr	Ni	Al	Mo	Ta	Cr	Ca	Si	Zr	P	S	C	O
8-12-3, Lot A	Chill Cast, Laser Welded	Bal.	8	12	3	Bal.	8.0	12.3	2.9	ND*	ND	ND	ND	ND	0.06	ND		
8-12-3, Lot B	"	Bal.	8	12	3	Bal.	6.8	12.4	3.1	0.11	0.09	0.18	0.02	<0.004	0.16	0.014		
8-12-3, Lot C	"	Bal.	8	12	3	Bal.	8.0	12.2	3.2	0.08	0.02	0.04	0.02	<0.004	0.03	0.007		
8-12-3, (Disk 1-8)	Argon Atomized, Chill Cast	Bal.	8	12	3	Bal.	8.1	11.8	2.9	0.05	0.02	0.10	0.01	0.004	0.11	0.028		
10-12-3, Lot A	Chill Cast, Laser Welded	Bal.				Bal.	9.9	12.2	3.0	ND	ND	ND	ND	ND	0.10	ND		
10-12-3, Lot B	"	Bal.				Bal.	10.2	12.4	3.3	0.06	0.07	0.16	0.01	<0.004	0.05	0.010		
10-12-3, Lot C	"	Bal.				Bal.	10.1	12.8	3.0	0.05	0.02	0.03	0.02	0.016	0.05	0.006		
10-12-3, (Disk 9-2)	Argon Atomized, Layerglazed	Bal.				Bal.	10.0	12.8	3.2	0.11	0.59	0.16	0.01	0.010	0.11	0.025		
11-12, Lot A	Chill Cast, Laser Welded	Bal.	11	12		Bal.	11.1	11.9	ND	0.05	<0.02	0.05	0.01	<0.004	0.03	0.006		
11-12, Lot B	"	Bal.	11	12		Bal.	10.7	14.3	ND	0.12	<0.02	0.04	<0.004	0.009	<0.03	0.008		
11-12-0-10 (Disk 3-2)	Argon Atomized, Layerglazed	Bal.	11	12		Bal.	10	10.7	13.3	ND	0.13	0.06	0.05	<0.002	ND	ND	0.15	
50 11-13	Chill Cast, Laser Welded	Bal.	11	13		Bal.	12.4	13.3	ND	0.09	<0.02	0.03	<0.004	<0.004	<0.03	0.008		
12-11, Lot A	"	Bal.	12	11		Bal.	11.6	10.4	ND	0.04	<0.02	0.14	<0.004	0.006	0.10	0.010		
12-11, Lot B	"	Bal.	12	11		Bal.	11.7	11.4	ND	0.04	<0.02	0.08	<0.004	<0.004	0.10	0.012		
12-12, Lot A	"	Bal.	12	12		Bal.	11.6	11.2	ND	0.04	0.04	0.14	<0.004	<0.004	0.03	0.017		
12-12, Lot B	"	Bal.	12	12		Bal.	10.9	11.5	ND	0.06	0.02	0.07	<0.004	<0.004	<0.03	0.009		
12-13, Lot A	"	Bal.	12	13		Bal.	11.6	11.0	ND	0.04	0.02	0.07	<0.004	<0.004	0.03	0.008		
12-13, Lot B	"	Bal.	12	13		Bal.	11.4	11.2	ND	0.04	0.02	0.07	<0.004	<0.004	<0.03	0.009		
12-13, (Disk 12-7)	Argon Atomized, Layerglazed	Bal.	12	13		Bal.	11.5	12.0	ND	0.07	0.04	0.09	<0.004	<0.004	0.15	0.030		
12-14, Lot A	Chill Cast, Laser Welded	Bal.	11.5	13.1	ND	Bal.	11.5	13.1	ND	0.05	0.02	0.02	<0.004	<0.004	<0.03	0.007		
12-14, Lot B	"	Bal.	12	14		Bal.	11.4	12.7	ND	0.08	0.02	0.09	<0.004	<0.004	0.03	0.010		
12-15, Lot A	"	Bal.	12	15		Bal.	11.4	14.4	ND	0.06	0.02	0.09	<0.004	<0.004	<0.03	0.008		
12-15, Lot B	"	Bal.	12	15		Bal.	11.5	12.7	ND	0.06	<0.02	0.11	<0.004	<0.004	0.15	0.009		
12-15, (Disk 9-1)	Argon Atomized, Laser Welded	Bal.	12	15		Bal.	11.8	17.3	ND	0.12	0.02	0.09	<0.004	<0.004	0.036	0.032		
12-16	Chill Cast, Laser Welded	Bal.	12	16		Bal.	11.4	14.4	ND									

\*ND = not determined

Table IX

## Tensile Test Data, Disk 1-8, Alloy 8-12-3

<u>Test Temperature</u>	<u>Specimen Identification</u>	<u>Orientation*</u>	<u>Gage Diameter</u>	<u>0.2% Yield Strength</u>	<u>Ultimate Tensile Strength</u>	<u>% Elongation</u>
			mm	MPa (ksi)	MPa (ksi)	
Ambient	6A	Radial;	3.18	1055 (153)	1227 (178)	37.0
	6B	Radial;	3.18	1055 (153)	1296 (188)	31.0
	9A	Radial;	2.03	1020 (148)	1241 (180)	53.0
	9B	Radial;	2.03	979 (142)	1227 (178)	44.0
	#1 inner	Axial;	3.18	993 (144)	1255 (182)	23.9
	#1 outer	Axial;	3.18	1110 (161)	1351 (196)	12.8
	#4 inner	Axial;	2.03	1062 (154)	1324 (192)	21.7
	#4 middle	Axial;	2.03	1069 (155)	1331 (193)	13.7
	#4 outer	Axial;	2.03	1055 (153)	1338 (194)	22.0
		Mean:	1044 (151)	1288 (187)	28.8	
		Unbiased Standard Deviation:	40 (6)	51 (7)	13.7	
538°C(1000°F)	6C	Radial;	3.18	993 (144)	1131 (164)	40.0
	9C	Radial;	2.03	931 (135)	1069 (155)	47.0
	#2 inner	Axial;	3.18	945 (137)	1089 (158)	9.3
	#3 inner	Axial;	2.03	938 (136)	1062 (154)	5.7
	#7 middle	Axial;	2.03	931 (135)	1084 (152)	6.0
		Mean:	948 (137)	1087 (158)	44.0	(Radial): 7.0 (Axial)
		Unbiased Standard Deviation:	26 (4)	27 (4)		
704°C(1300°F)	6D	Radial;	3.18	979 (142)	1124 (163)	31.5
	#2 outer	Axial;	3.18	800 (116)	800 (116)	2.3
	#7 inner	Axial;	2.03	724 (105)	724 (105)	5.0
	#7 outer	Axial;	2.03	642 (93)	642 (93)	0
	Single Test Value, Radial:		979 (142)	1124 (163)	31.5	
	Mean, Axial:		722 (105)	722 (105)	2.4	

Table X  
Tensile Properties, Nickel Base Turbine Disk Alloys

Alloy: Orientation of Load Axis:	8-12-3 (Radial)	LAYERGLAZED ALLOYS (As Processed)				COMMERCIAL ALLOYS (Heat Treated)			
		8-12-3 (Axial)	12-15 (Axial)	11-12-0-0-5 (Axial)	11-12-0-0-10 (Axial) (Solution) (Annealed)	Forged HIP, L/C Gatorized HIP Waspaloy Astroloy	IN 100	MERL 76	
0.2% Yield Strength MPa (ksi)									
Ambient Temperature	1027(149)	1055(153)	1214(176)	1096(159)	1014(147)	1172(170)	793(115)	1048(152)	1117(162)
538°C (1000°F)	965(140)	938(136)	—	—	—	—	724(105)	965(140)	1089(158)
704°C (1300°F)	979(142)	724(105)	1179(171)	—	979(142)	—	690(100)	938(136)	1089(158)
Ultimate Tensile Strength MPa (ksi)									
Ambient Temperature	1248(181)	1317(191)	1393(202)	1407(204)	1358(197)	1365(198)	1241(180)	1379(200)	1558(226)
538°C (1000°F)	1103(160)	1069(155)	—	—	—	—	1103(160)	1310(190)	1510(219)
704°C (1300°F)	1124(163)	724(105)	1241(180)	600(87)	1048(152)	—	1069(155)	1227(178)	1241(180)
% Elongation									
Ambient Temperature	40	20	<6	4	5	2	15	22	22
538°C (1000°F)	43	7	—	—	—	—	15	21	22
704°C (1300°F)	32	2	<6	<1	9.9	—	20	26	18

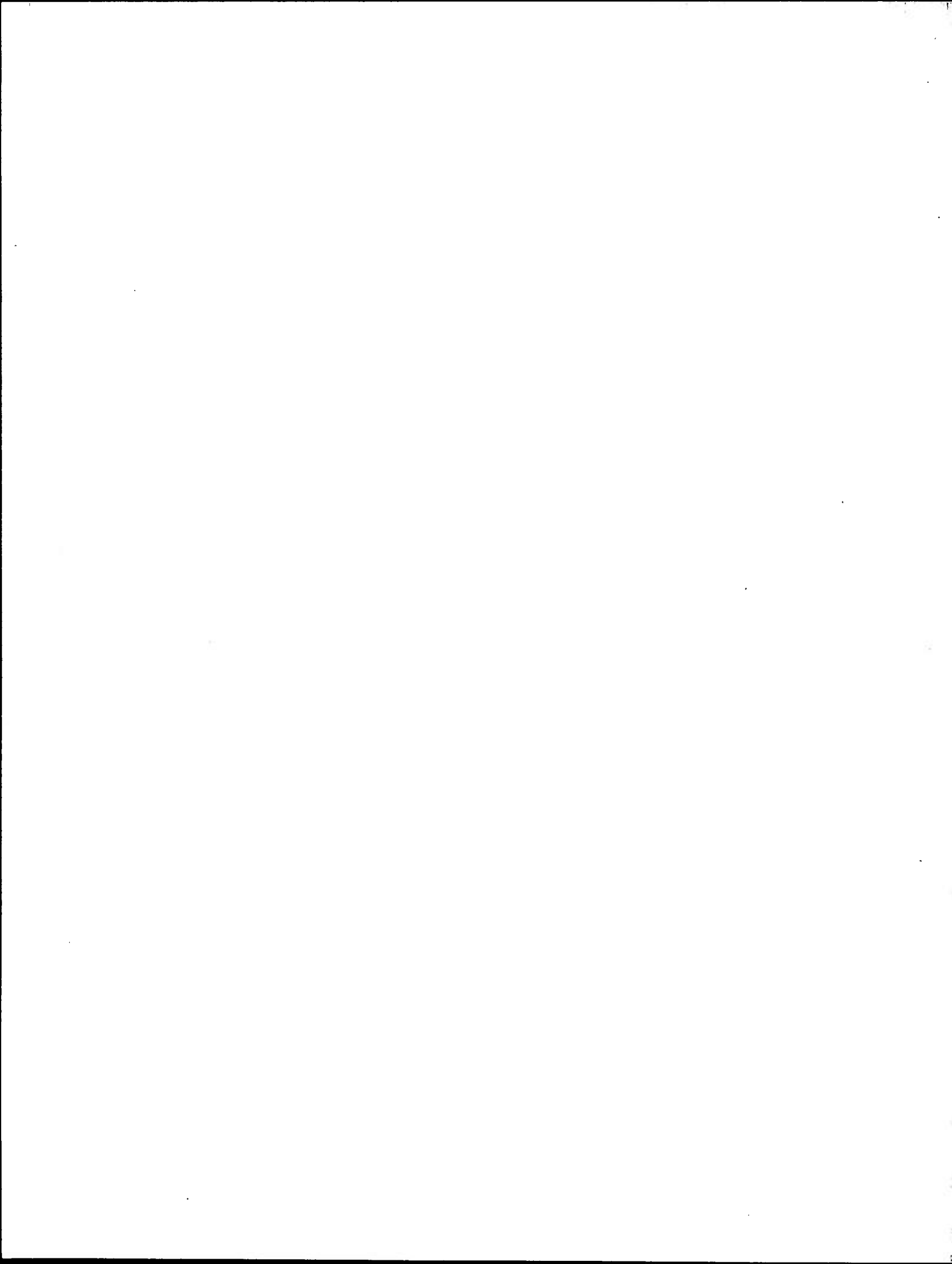
Table XI

Observed Interplanar Spacings of Orthorhombic Ni<sub>3</sub>Mo  
 (Disk 1-8, Alloy 8-12-3, Annealed 32 hrs at 704°C)

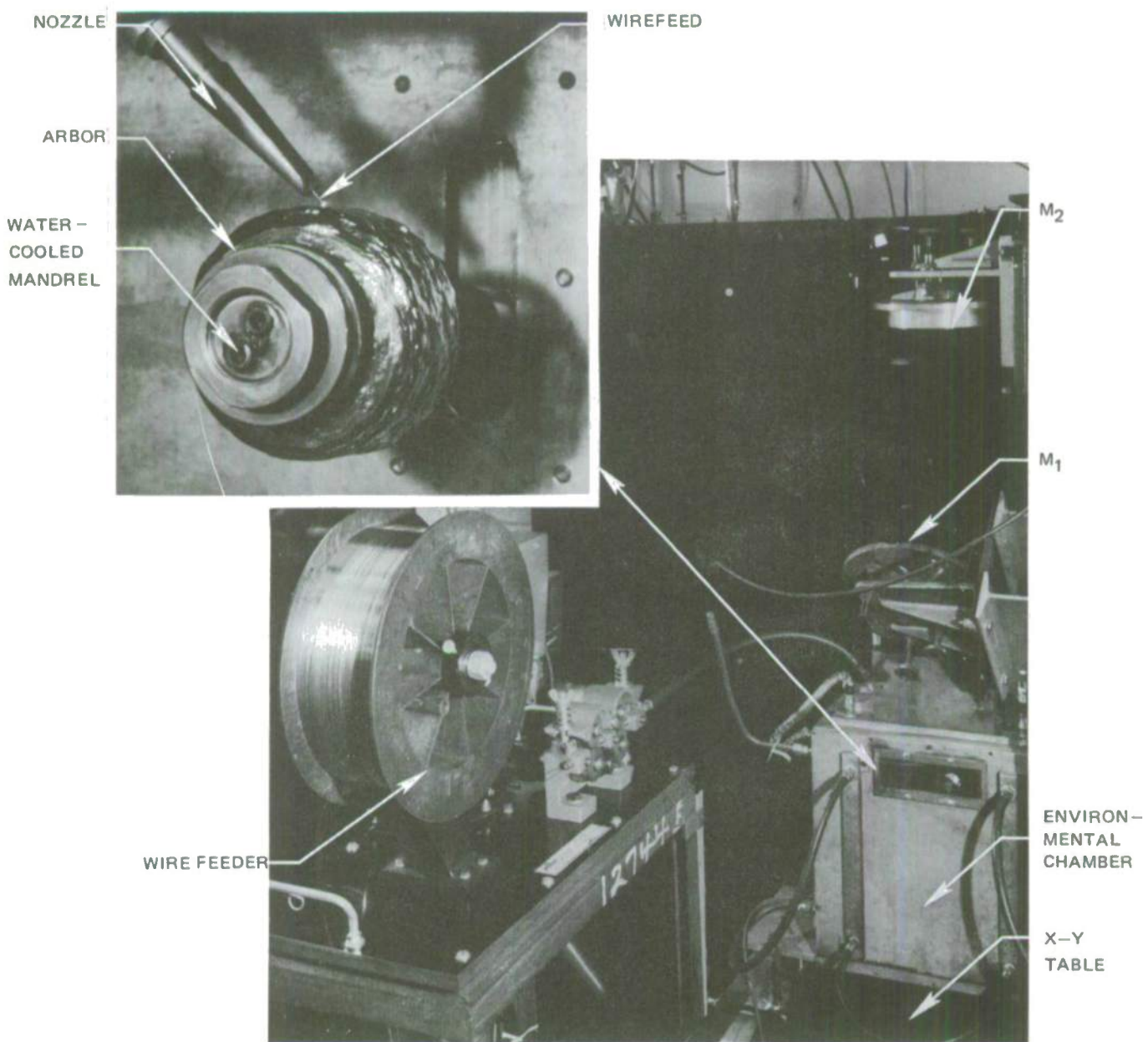
<u>d observed (Å)</u>	<u>h k l</u>	<u>d calculated** (Å)</u>
4.23	010*	4.22
4.43	001	4.45
3.07	011	3.06
1.97	012	1.97
1.92	021	1.91
1.42	013	1.40
1.35	031	1.34

\*forbidden reflection; present due to double diffraction

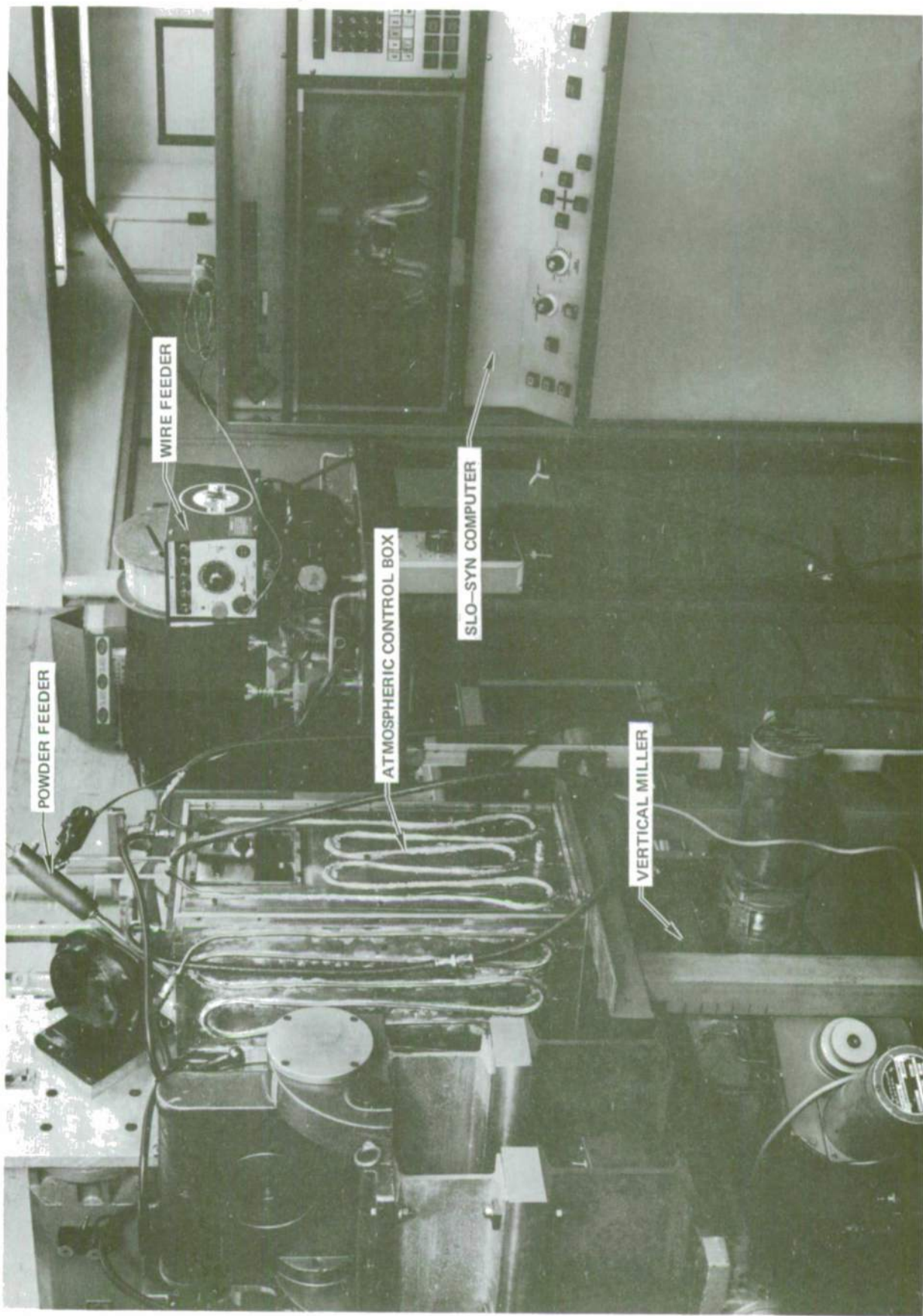
\*\*a<sub>0</sub> = 5.064; b<sub>0</sub> = 4.224; c<sub>0</sub> = 4.448 (Ref. 43)



## LAYERGLAZE PROCESSING APPARATUS

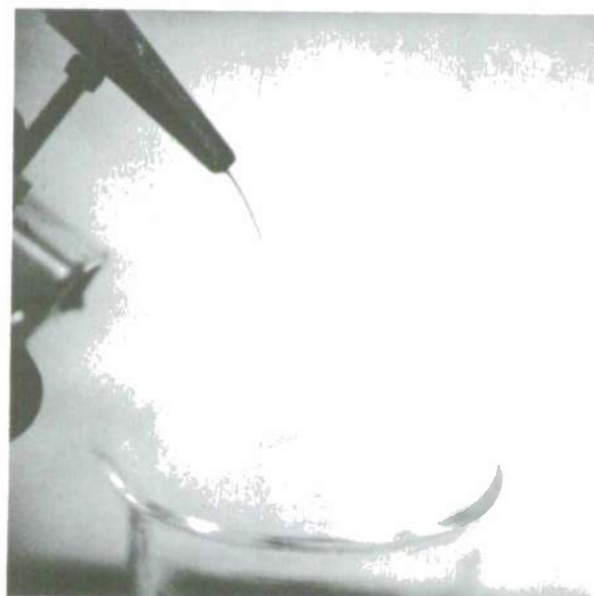


## AUTOMATED LAYERGLAZE PROCESSING APPARATUS



### LAYERGLAZE POWDER FEED FLOW TEST

- 8-12-3 SUPERALLOY
- VIBRATOR FORCED

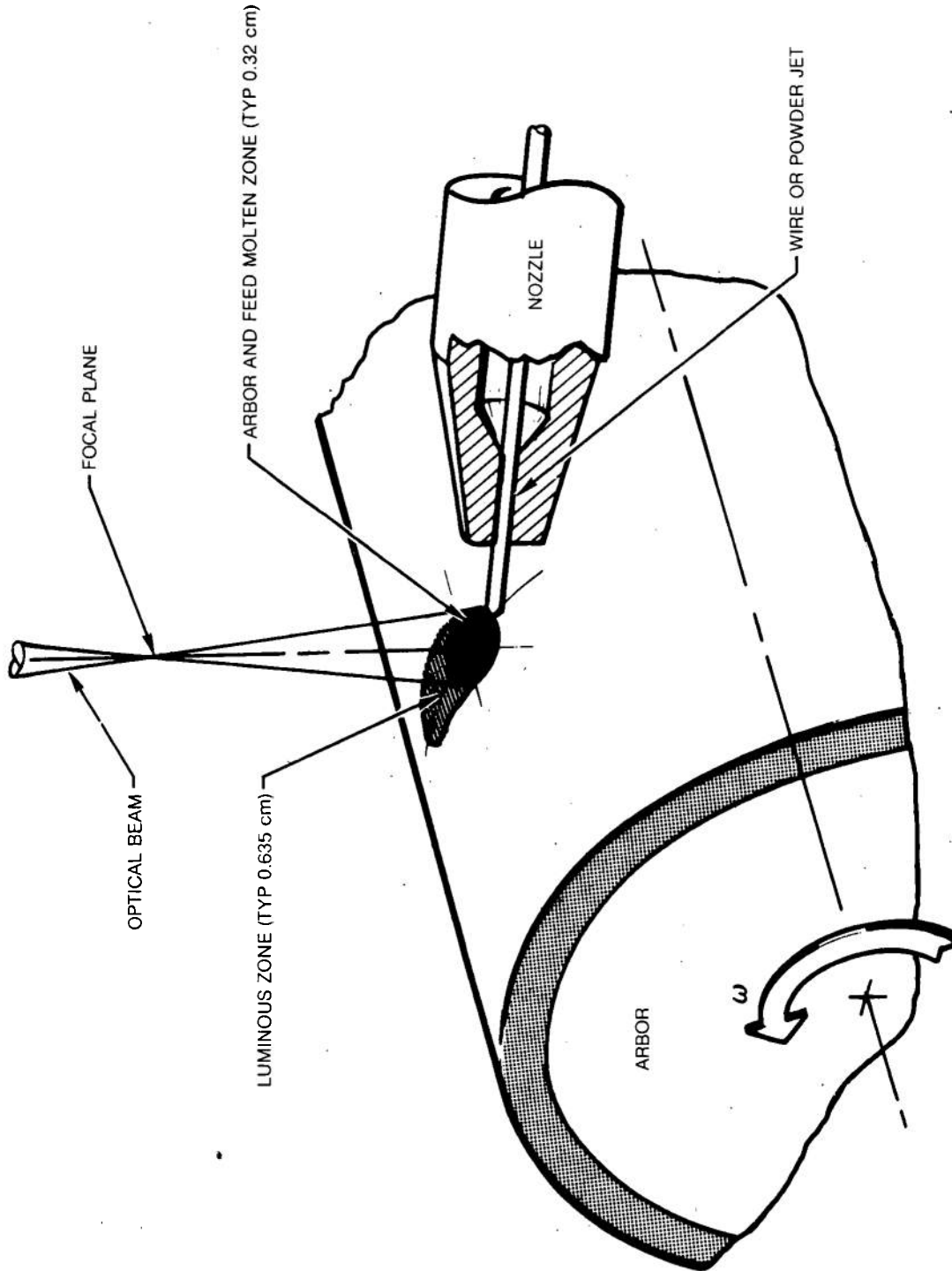


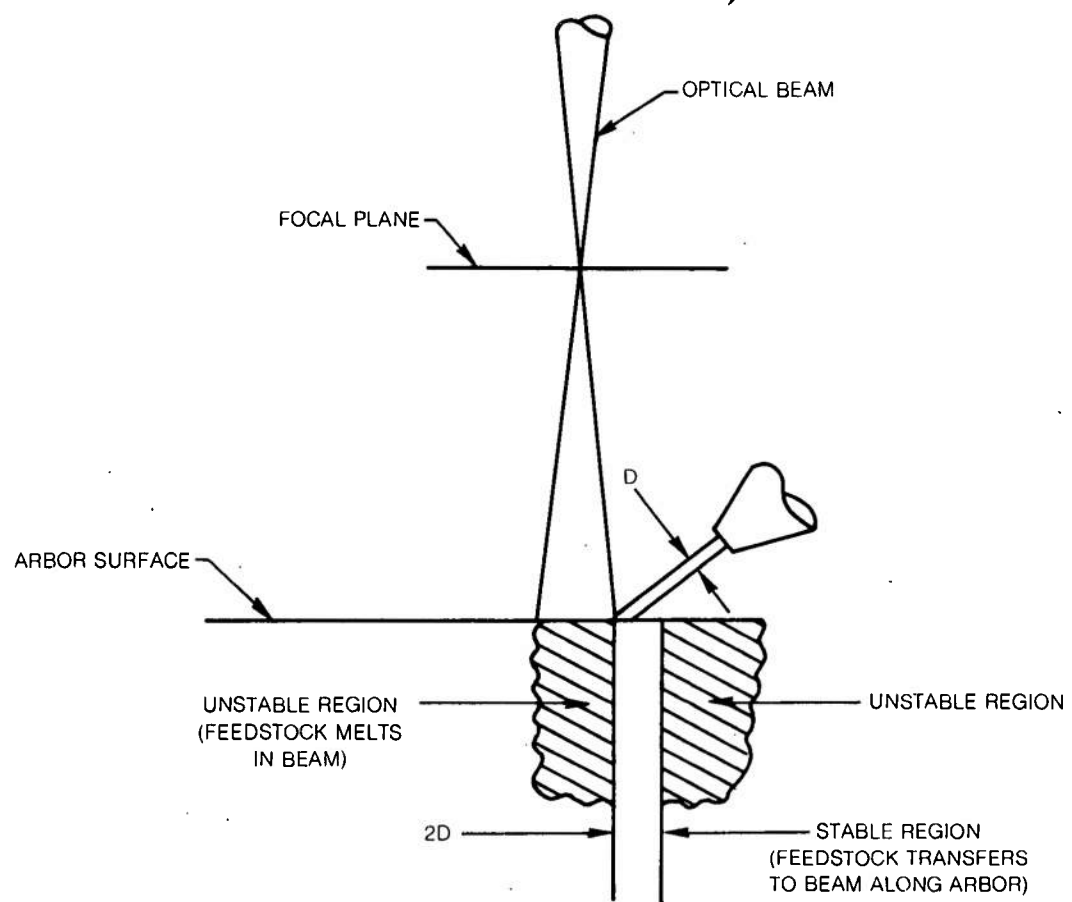
## DROP TRANSFER EFFECTS IN WIRE - FEED LAYERGLAZE PROCESS

- SINGLE LAYER
- MULTIPLE LAYER
- NEAR OPTIMUM DROPLETS
- LARGE DROPLETS



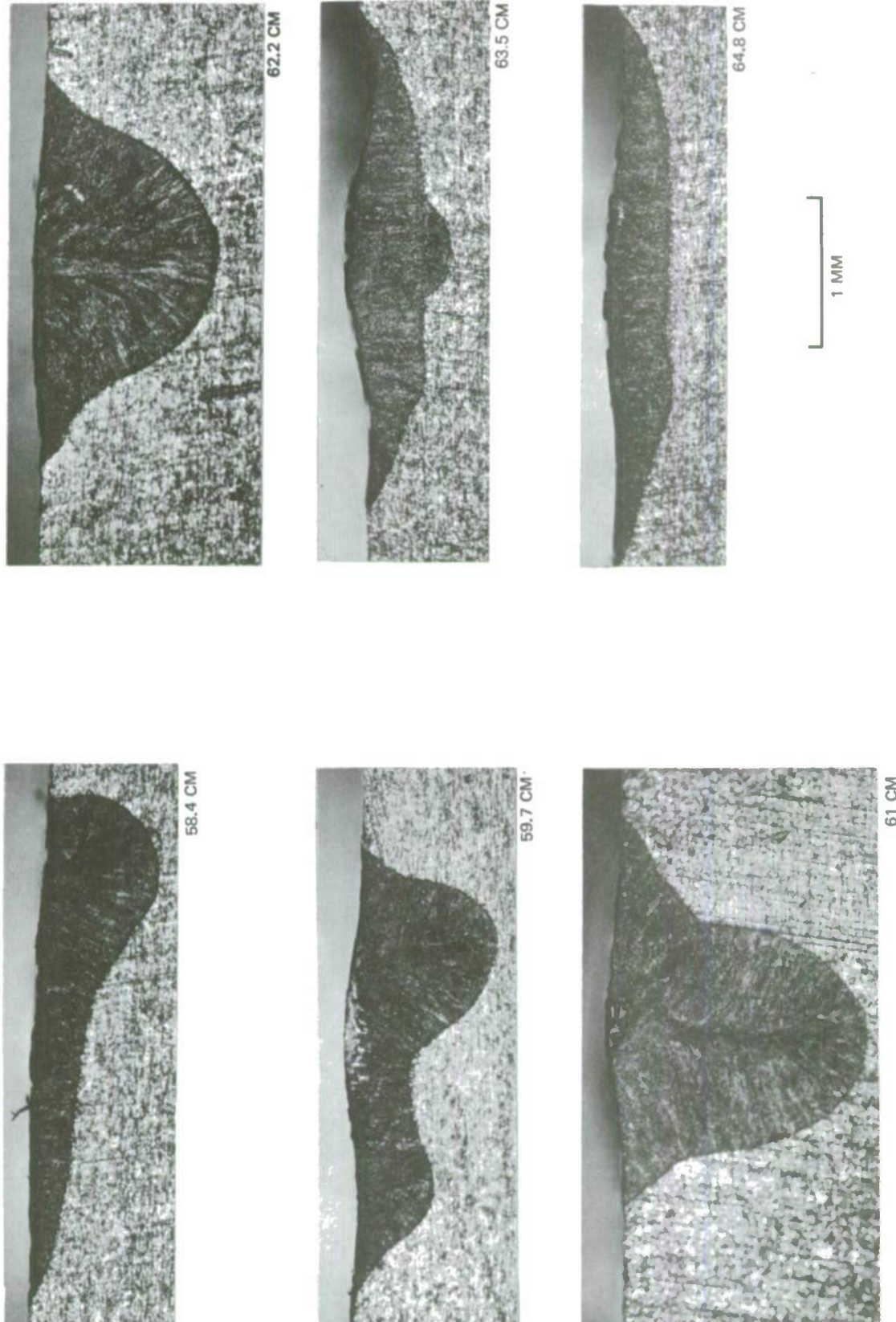
DETAILS OF INTERACTION REGION BETWEEN OPTICAL BEAM,  
ARBOR AND FEEDSTOCK MATERIAL

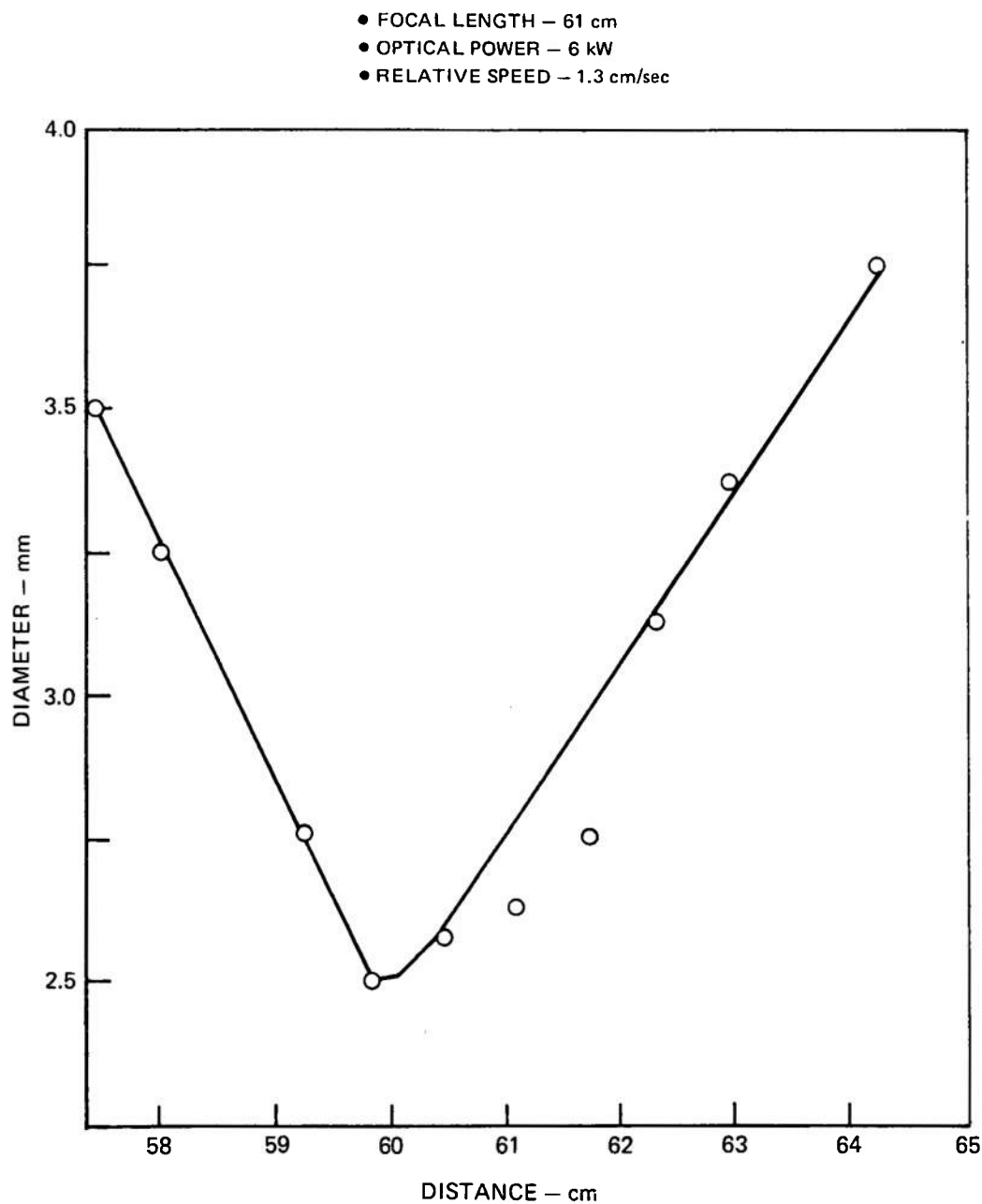


**STABILITY CRITERION FOR LAYERGLAZE PROCESS FEEDSTOCK INTERACTION ZONE**

**MOLTED PROFILE AS FUNCTION POSITION**

- RELATIVE SPEED - 1.3 CM/SEC
- FOCAL LENGTH - 61 CM
- OPTICAL POWER - 6 kW



**SPOT SIZE AS FUNCTION OF DISTANCE FROM FOCUS MIRROR**

## EFFECT OF CROSS FEED SPEED ON WIRE DEPOSIT

- SINGLE LAYER
- POWER—5.5 KW
- WIRE—1.5 CM/SEC
- SURFACE SPEED—4.45 CM/SEC
- SPACING—64.5 CM



3.8 CM/MIN

3 CM/MIN

5 CM/MIN

## LAYERGLAZE TEST ARBORS WITH FIVE LAYER DEPOSITS



3 CM/MIN.

3.8 CM/MIN.

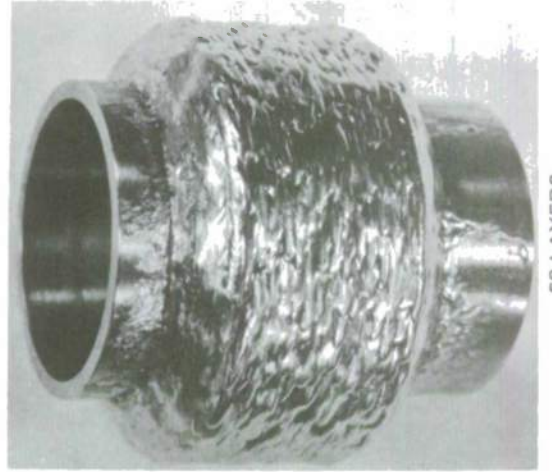
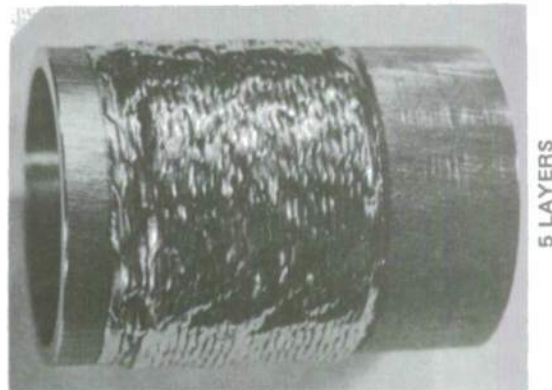
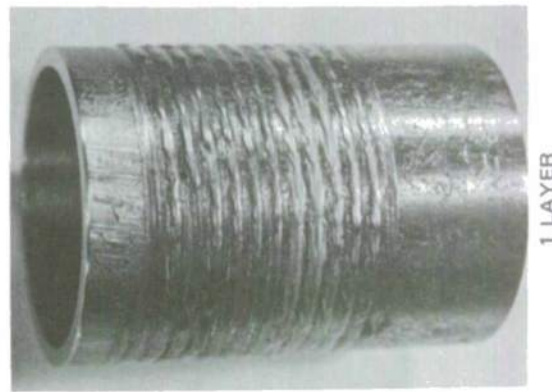
5 CM/MIN.



- SURFACE SPEED - 4.45 CM/SEC
- ARBOR ADVANCE RATE - AS SPECIFIED
- WIRE - 0.9 MM DIAMETER AT 1.5 CM/SEC
- LASER POWER AT WORKPIECE - 5.0 kW

## EFFECT OF NUMBER OF DEPOSITED LAYERS ON SURFACE APPEARANCE

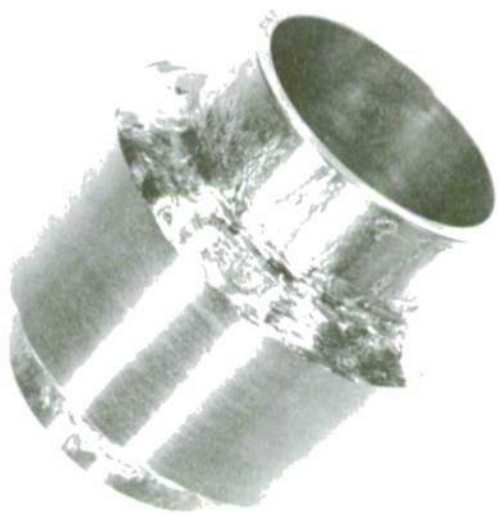
- POWER—5.5 KW
- WIRE—1.5 CM/SEC
- SURFACE SPEED—4.45 CM/SEC
- SPACING — 64.5 CM



58 LAYER LAYERGLAZE DEPOSIT

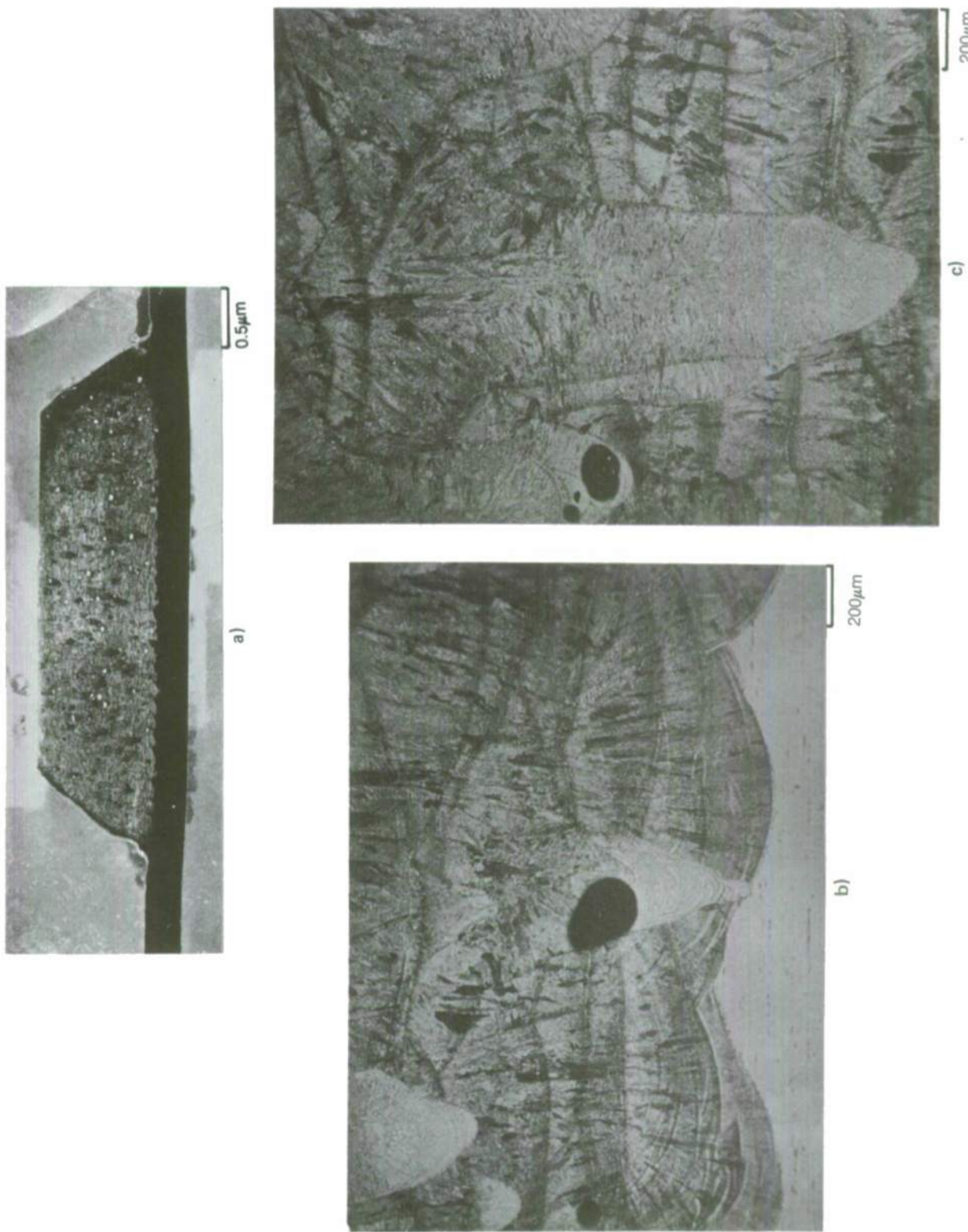


AS DEPOSITED



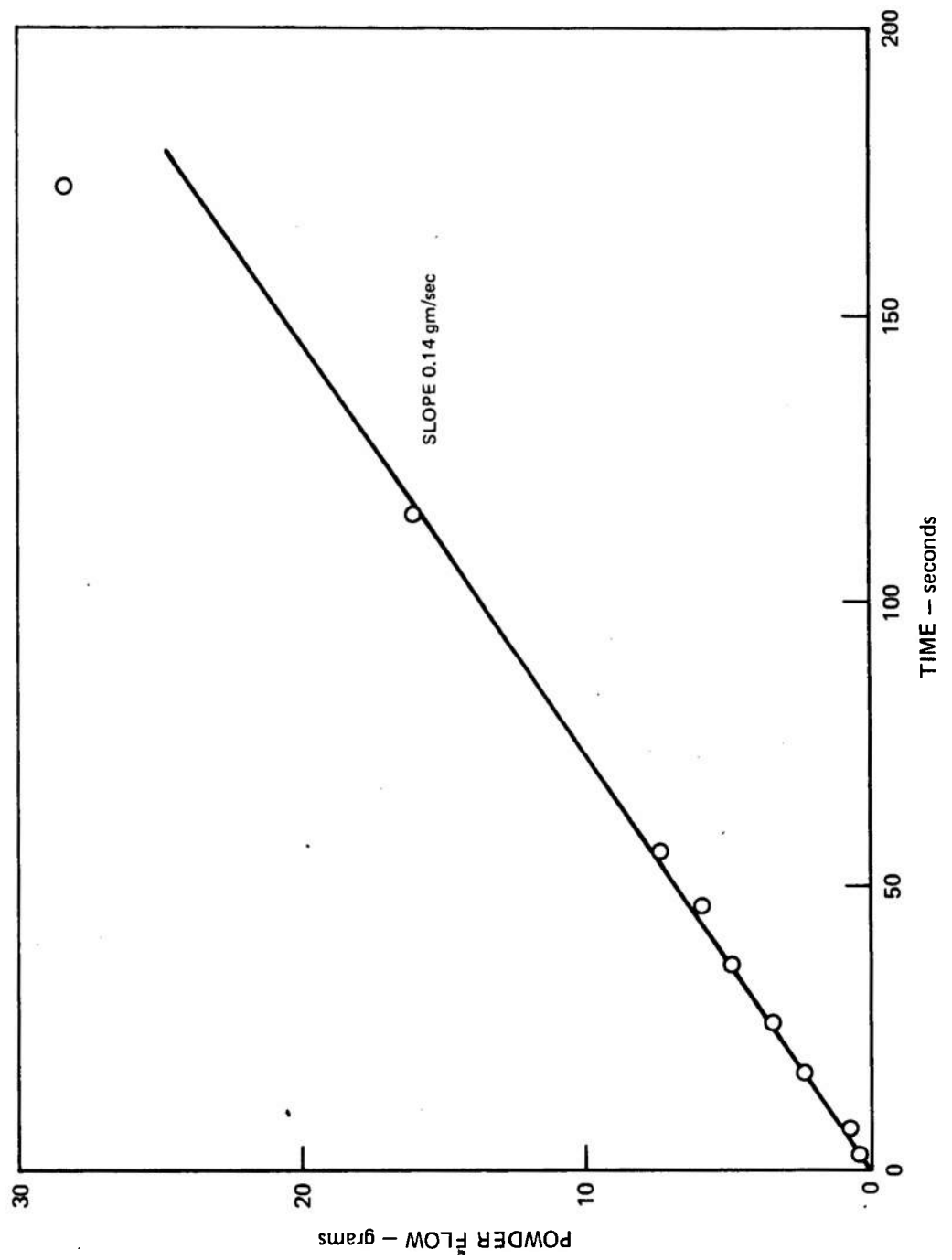
SURFACE MACHINED

MACROETCHED CROSS-SECTION OF 58 LAYER DEPOSIT



## 8-12-3 POWDER FLOW RATE CALIBRATION

- 0.9 mm dia COPPER NOZZLE
- HAND VIBRATOR
- -170 TO +500 MESH.



LAYERGLAZE TEST SAMPLE NO. 1-6

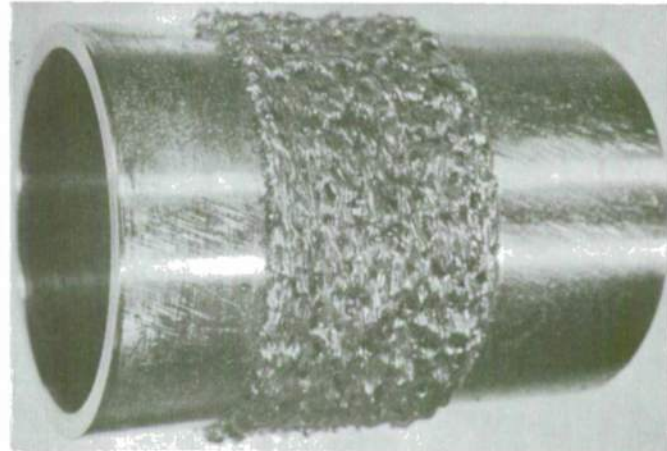
- ALLOY: 8-12-3
- POWDER: (-170, + 500 MESH)
- POWER: 5 kW
- SURFACE SPEED: 6.7 CM/SEC



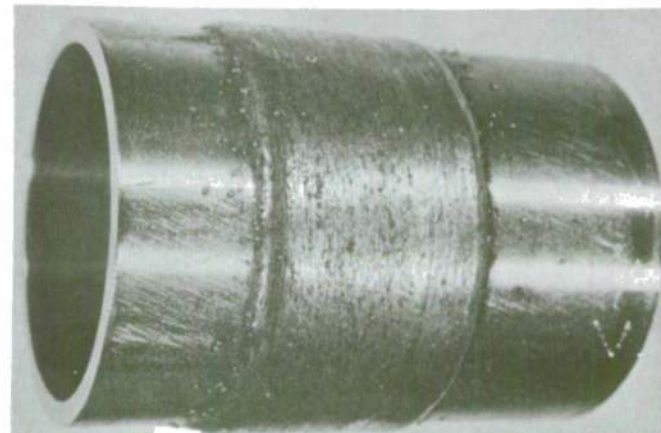
## EFFECT OF LASER POWER ON POWDER DEPOSIT QUALITY

(ALL SAMPLES SAME NOZZLE DIAMETER AND TRAVERSE SPEEDS)

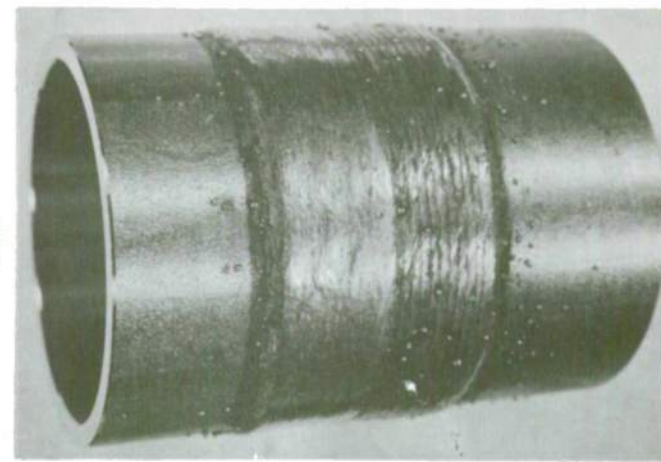
3 kW



4 kW



5 kW



### SAMPLE #2-6

- 5 LAYERS
- INCOMPLETE MELTING
- SURFACE NOT GLAZED

### SAMPLE #2-7

- 5 LAYERS
- SLIGHT ADHERENT SPATTER
- 3/4 SURFACE GLAZED, FINAL PASS
- SURFACE SLIGHTLY OXIDIZED DUE TO WATER LEAK

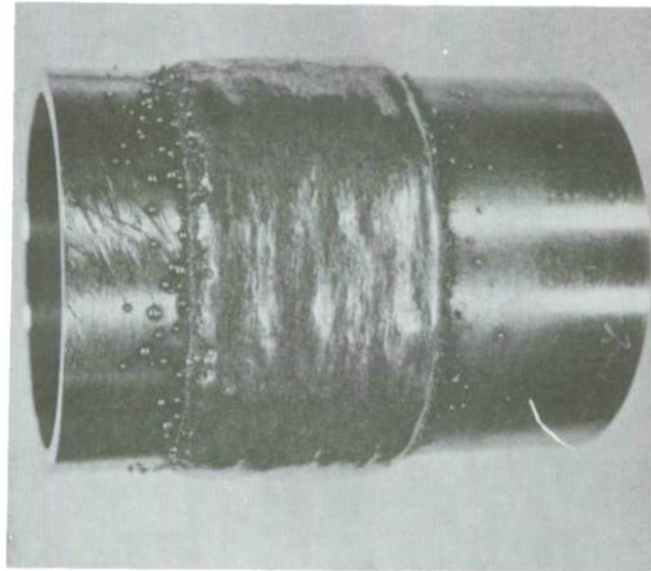
### SAMPLE #2-8

- 5 LAYERS
- LESS ADHERENT SPATTER
- 1/2 SURFACE GLAZED FINAL PASS

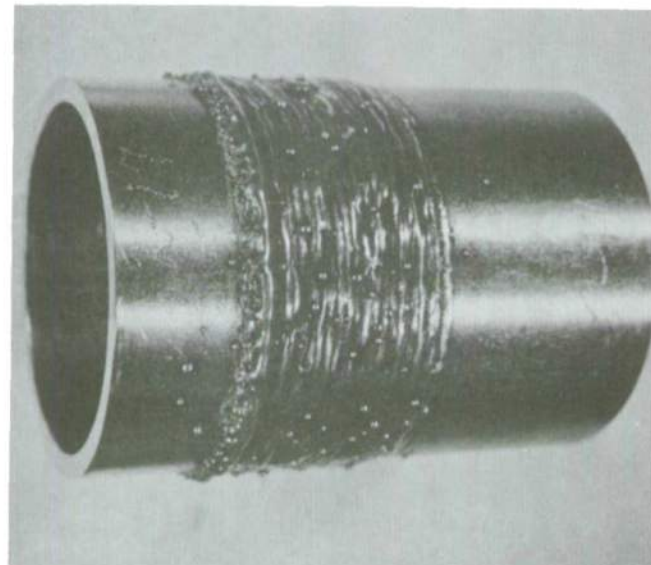
## EFFECT OF MASS FLOW ON POWDER DEPOSIT QUALITY

(ALL SAMPLES AT 5 kW AND SAME TRAVERSE SPEEDS)

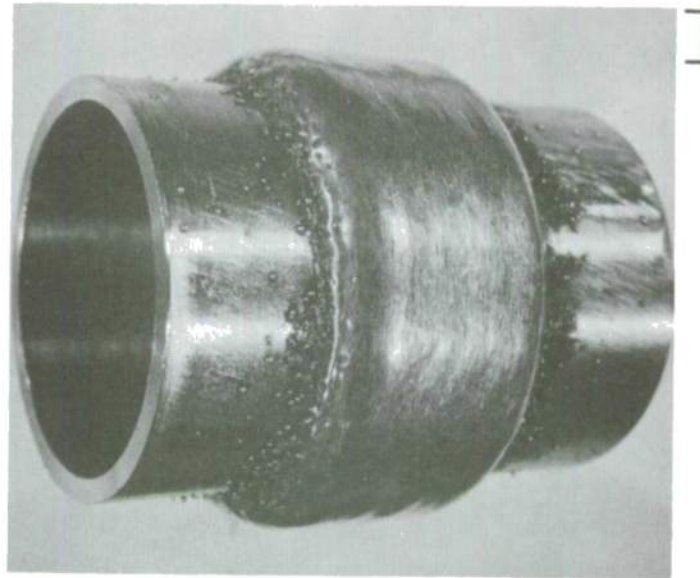
1.1 MM NOZZLE



1.1 MM NOZZLE



0.9 MM NOZZLE



1 CM

SAMPLE #2-16

- 2 LAYERS
- 0.8 MM/LAYER
- LARGE DROPLETS GLAZED ON BOTH PASSES

SAMPLE #2-17

- 1 LAYER
- 0.8 MM/LAYER
- LARGE DROPLETS NOT GLAZED

SAMPLE #2-4

- 15 LAYERS
- 0.25 MM/LAYER
- SMALLER DROPLETS
- GLAZED ON FINAL PASS ONLY

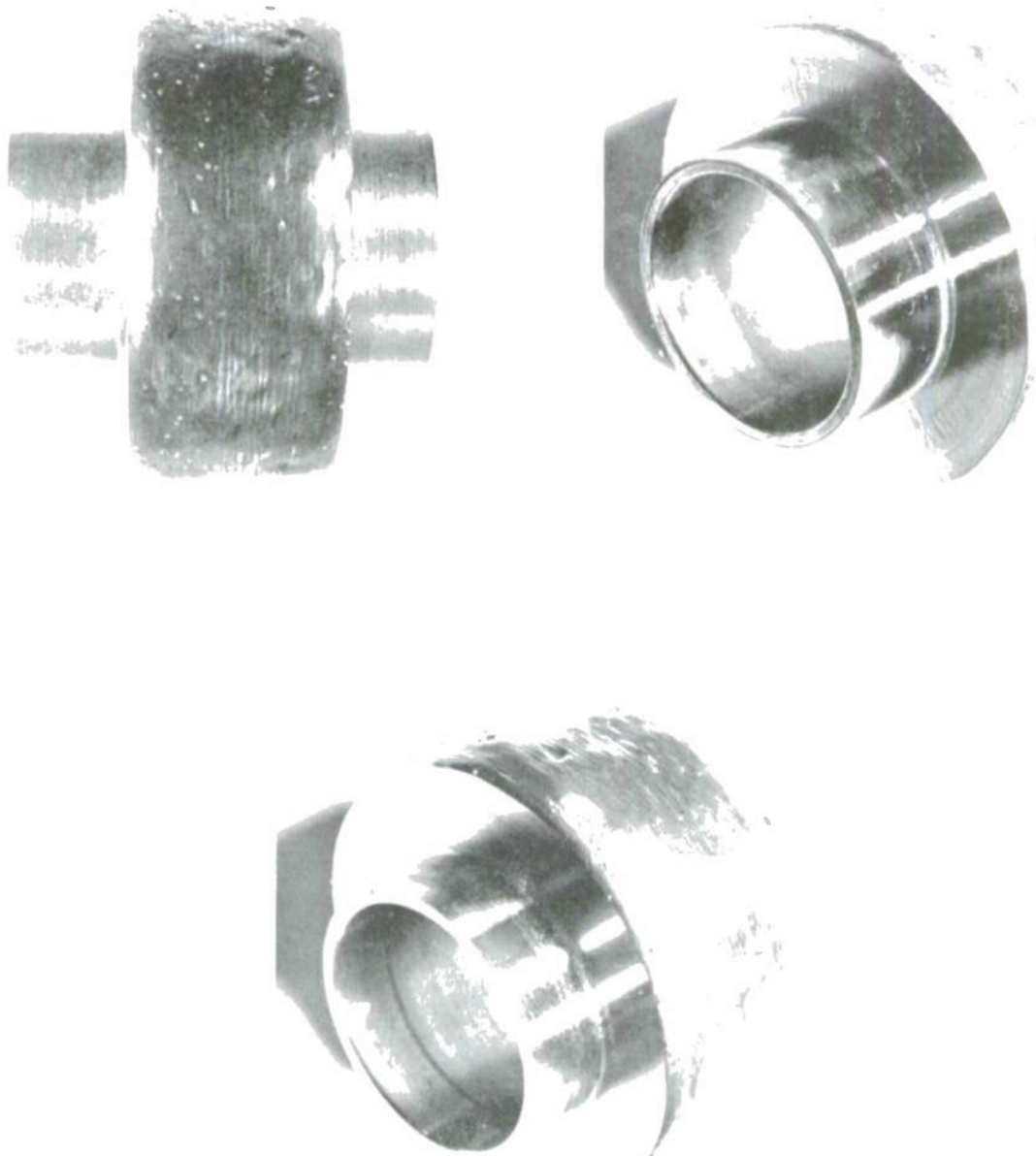
**LAYERGLAZE TEST SAMPLE NO. 1-8, AS-FABRICATED**

- POWER: 5.0 kW
- SURFACE SPEED: 8.5-14.2 CM/SEC
- 8-12-3 POWDER: (-100, + 500 MESH)
- FINAL DIAMETER: 6.45 CM



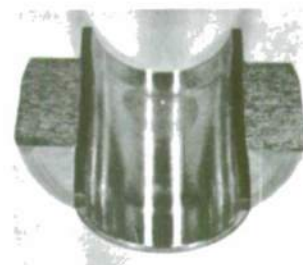
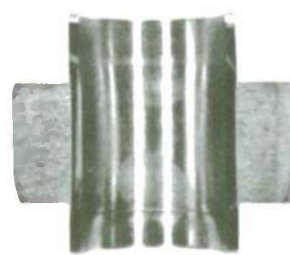
## LAYERGLAZE TEST SAMPLE NO. 1-8 AFTER MACHINING OF ENDS

- POWER: 5.0 kW
- SURFACE SPEED: 8.5–14.2 CM/SEC
- 8-12-3 POWDER: (-100, + 500 MESH)
- FINAL DIAMETER: 6.45 CM

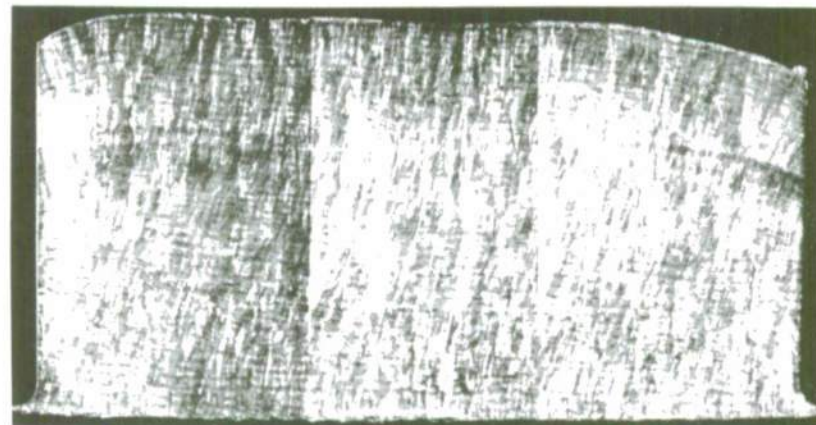


CROSS SECTION OF LAYERGLAZE TEST SAMPLE NO. 1-8

(TRANSVERSE SECTION—MACROETCHED)



MACRO PHOTOS



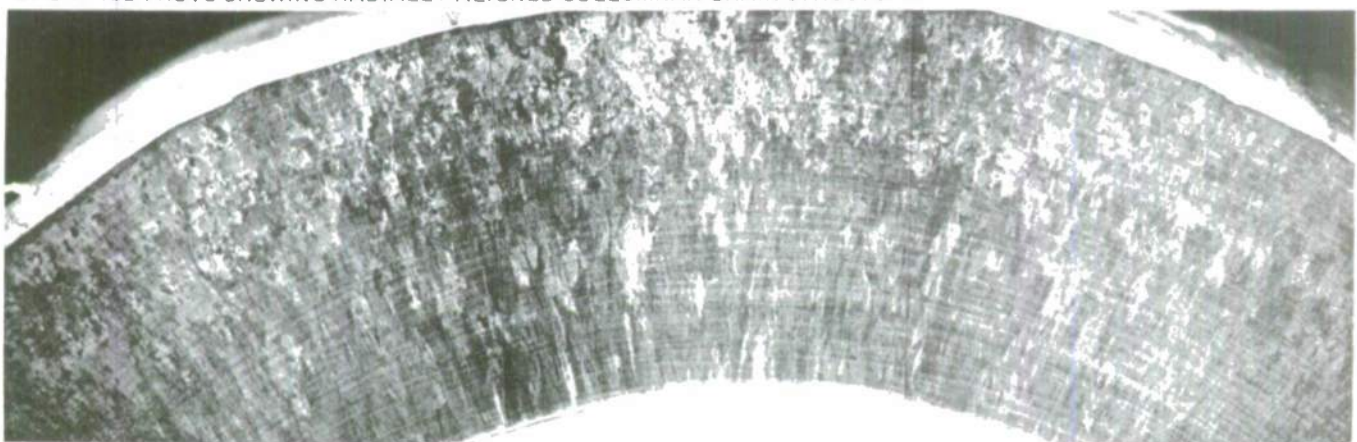
LOW MAGNIFICATION MAP OF DEPOSITED CROSS SECTION

END VIEW OF DEPOSITED MATERIAL ON LAYERGLAZE TEST SAMPLE NO. 1-8

MACRO PHOTO OF PART



MAGNIFIED PHOTO SHOWING RADIALLY ALIGNED COLUMNAR GRAIN STRUCTURE



LAYERGLAZE—FABRICATED TURBINE DISK PREFORM

FINAL DIAMETER : 13.2 CM  
(BOTH SIDES ARE SHOWN)



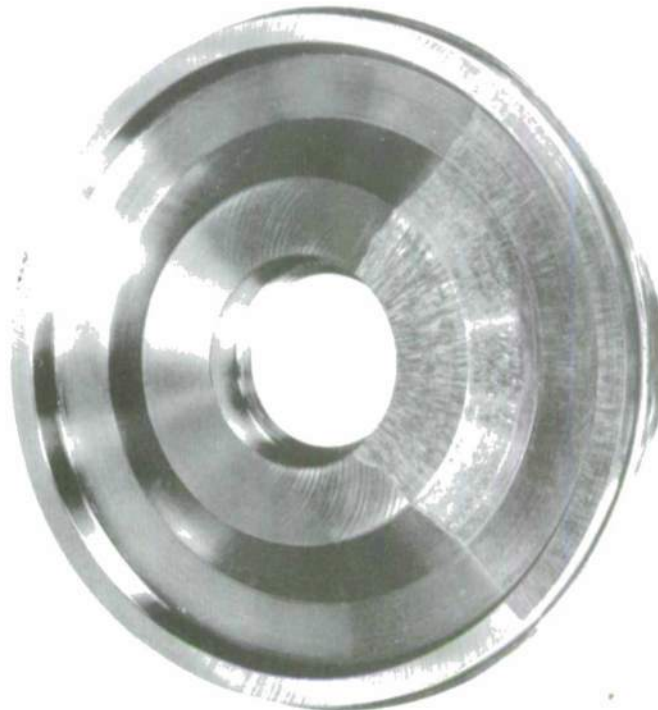
LAYERGLAZE—FABRICATED TURBINE DISK PREFORM

(MACHINED TO A ROUGH DISK CONFIGURATION AND ETCHED)

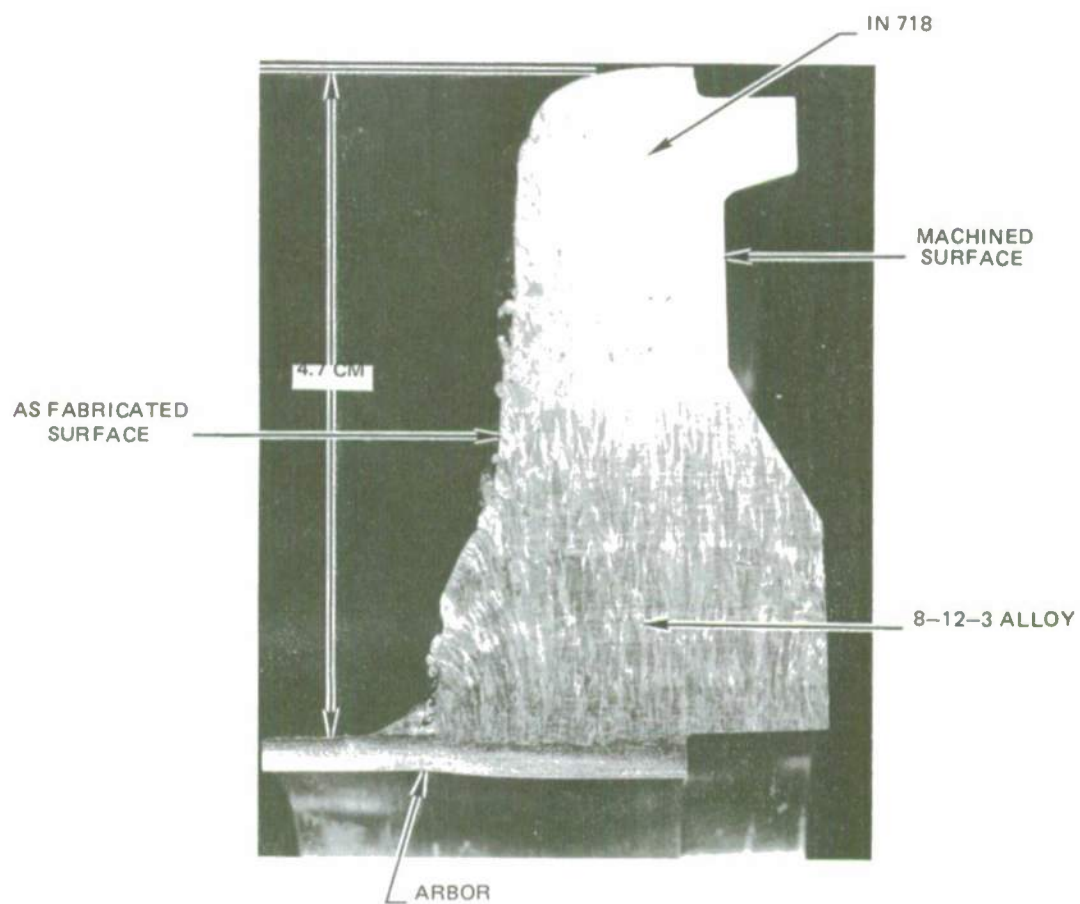
FINAL DIAMETER : 13.2 CM

AS MACHINED

PARTIALLY ETCHED

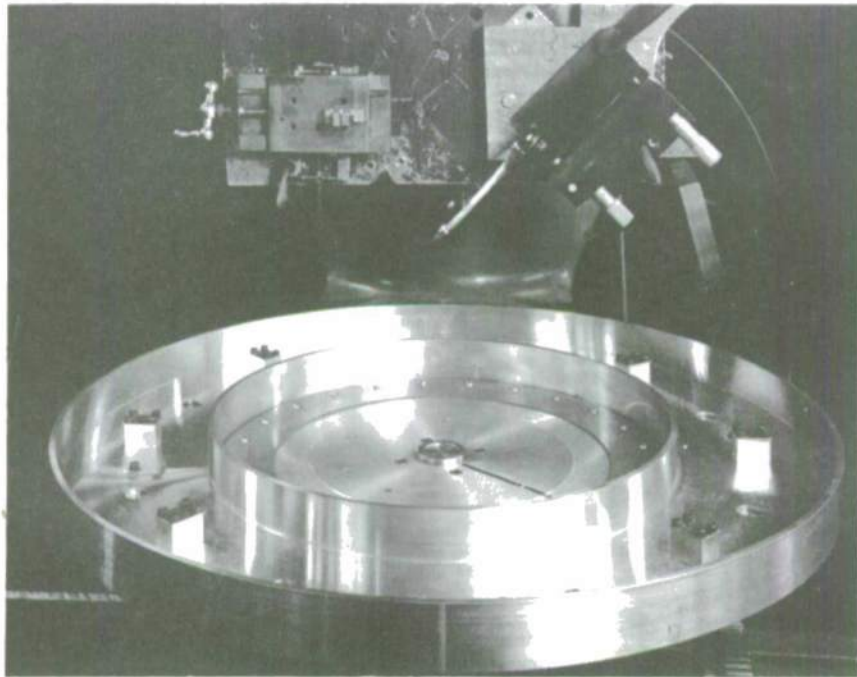


MACROETCH CROSS-SECTION OF LAYERGLAZE—  
FABRICATED TURBINE DISK PREFORM

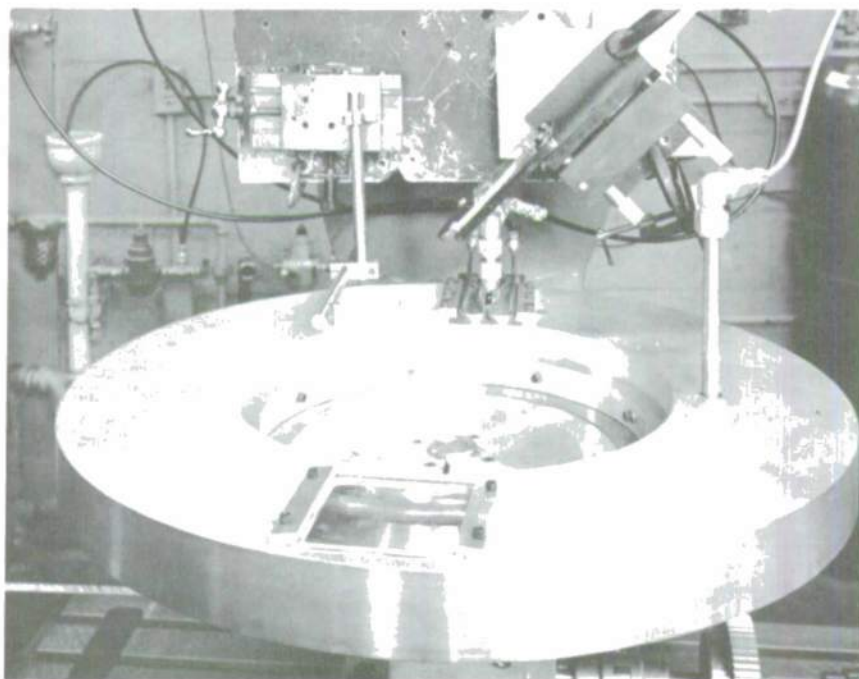


**COVERED WHEEL ASSEMBLY UTILIZED FOR LASER WELD CRACK TESTING**

(a) MOVING PORTION OF ASSEMBLY WITH COVER REMOVED AND SIX SPECIMENS IN PLACE, 23 CM FROM WHEEL CENTER



(b) STATIONARY COVER IN PLACE; LASER BEAM PORT AT 12 O'CLOCK

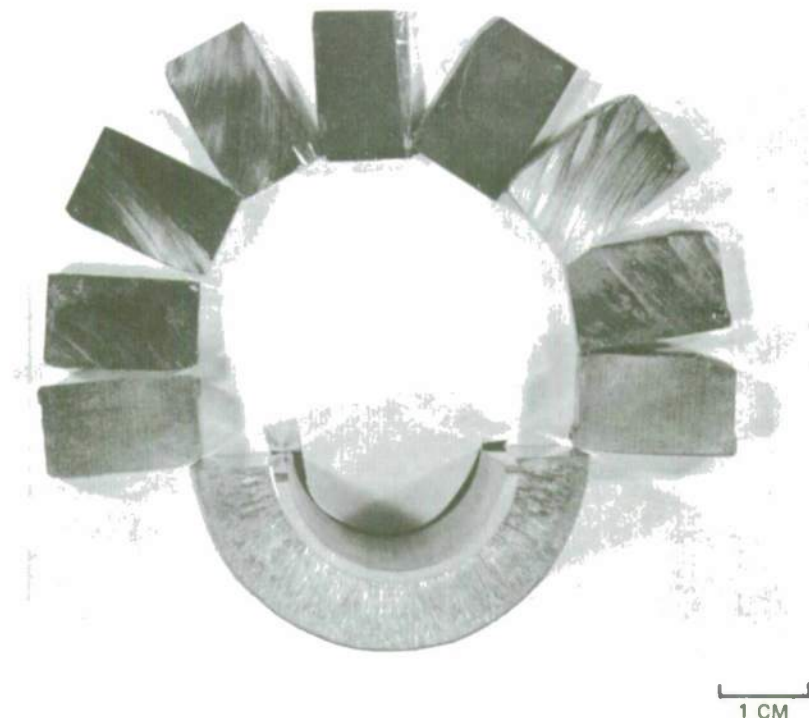


## PIECES SECTIONED FROM DISK 1-8, ALLOY 8-12-3, FOR RADIOGRAPHY AND TENSILE SPECIMENS

(A) VIEW EDGE-ON

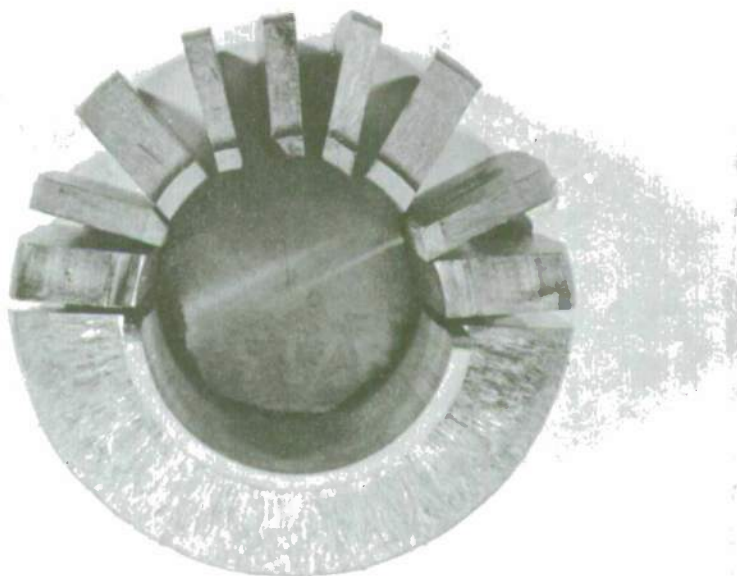
(B) VIEW WITH CUT FACES FLAT

A.



1 CM

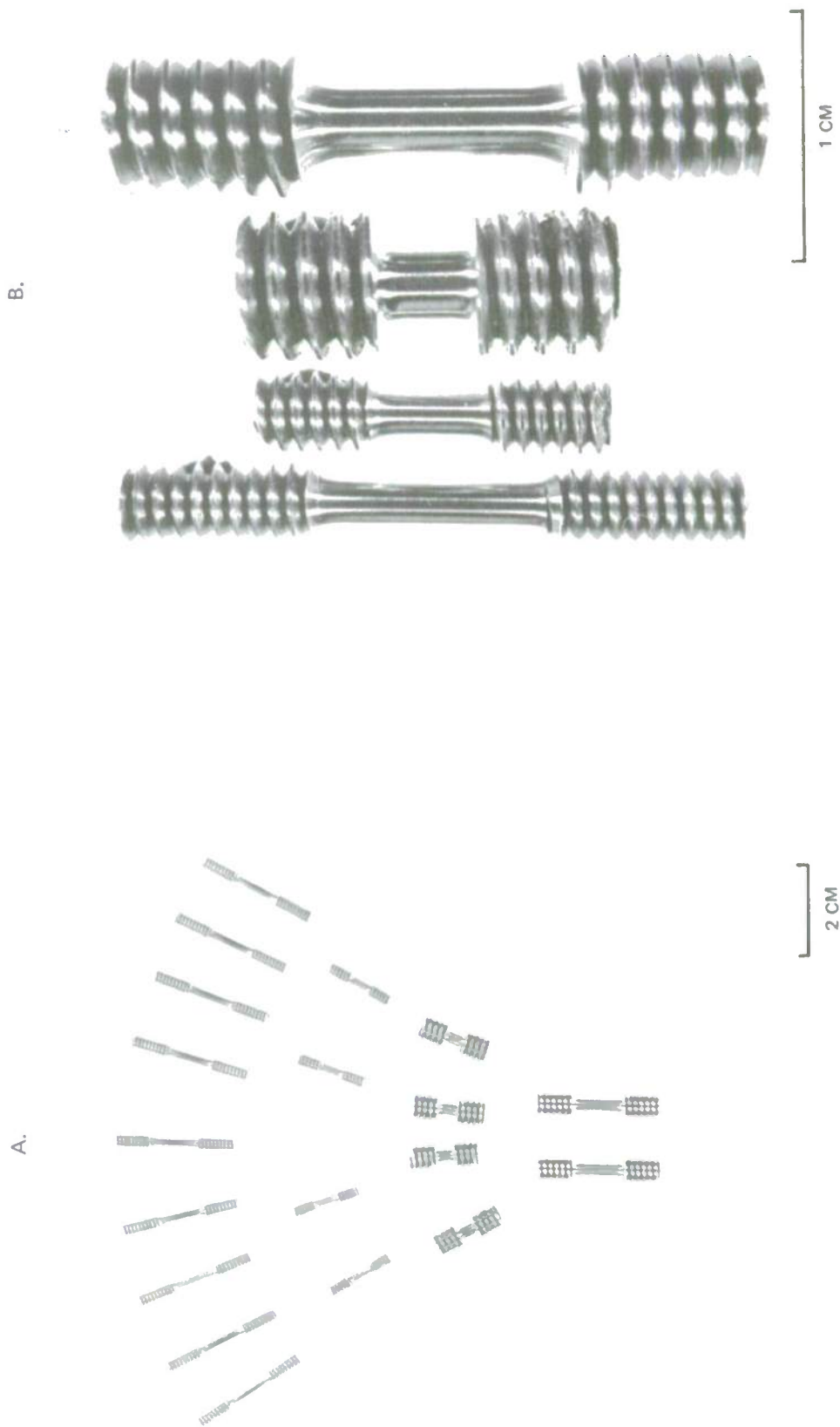
B.



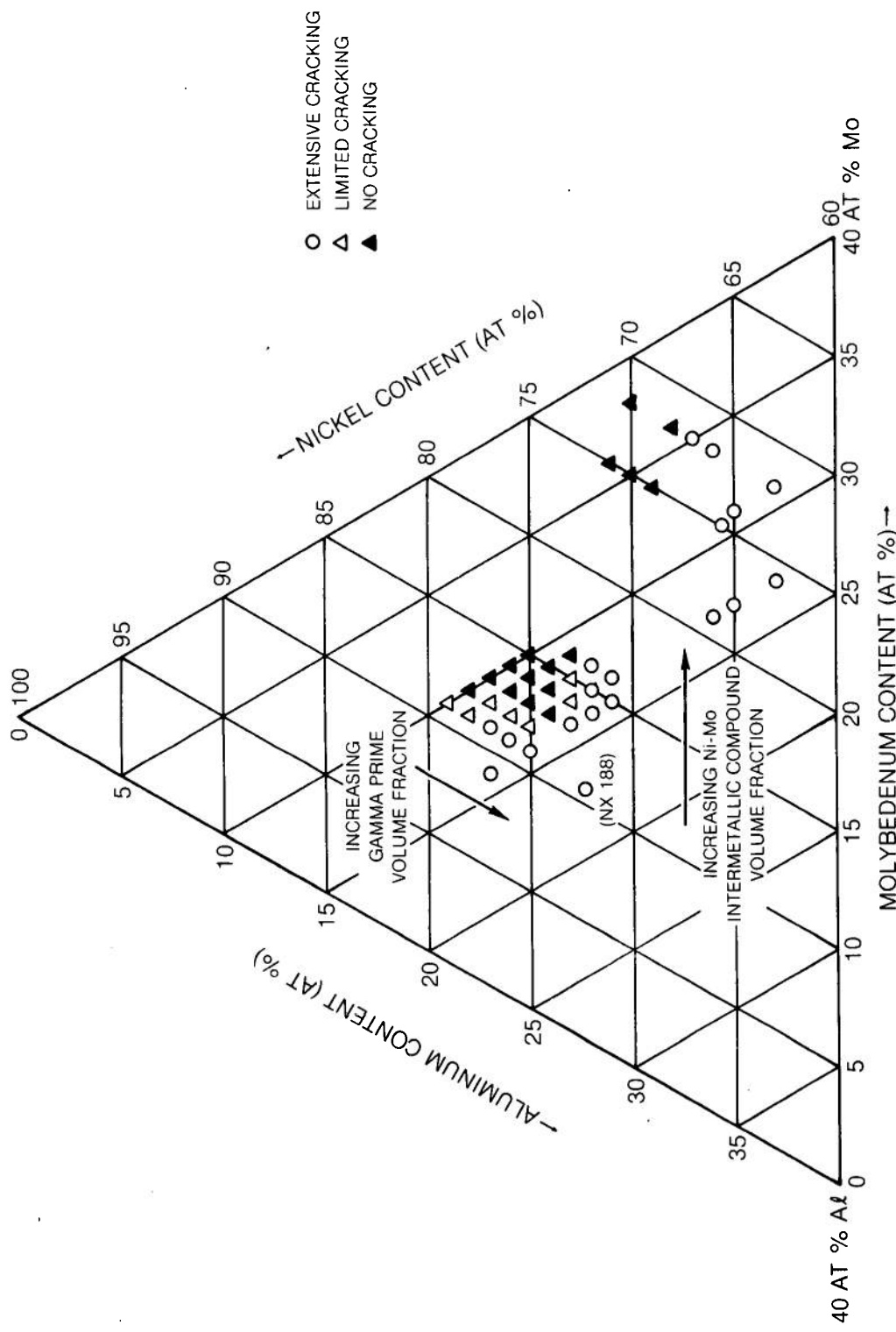
1 CM

**TENSILE SPECIMENS MACHINED FROM OF DISK 1-8**

SHORT SPECIMENS ARE ORIENTED PARALLEL TO THE DISK RADIUS; LONG SPECIMENS ARE PARALLEL TO THE DISK ROTATIONAL AXIS.  
(A) ALL TENSILE SPECIMENS (B) ALL FOUR SIZES OF TENSILE SPECIMEN. GAGE LENGTHS ARE 7.62 AND 2.54 MM (0.3 AND 0.1 IN.).  
GAGE DIAMETERS ARE 3.18 AND 2.03 MM (0.125 AND 0.08 IN.)



## CRACKING RESPONSE TO LASER PROCESSING, NICKEL-ALUMINUM-MOLYBDENUM ALLOYS



## **NICKEL-ALUMINUM-MOLYBDENUM-TANTALUM ALLOYS CRACKING RESPONSE TO LASER PROCESSING,**

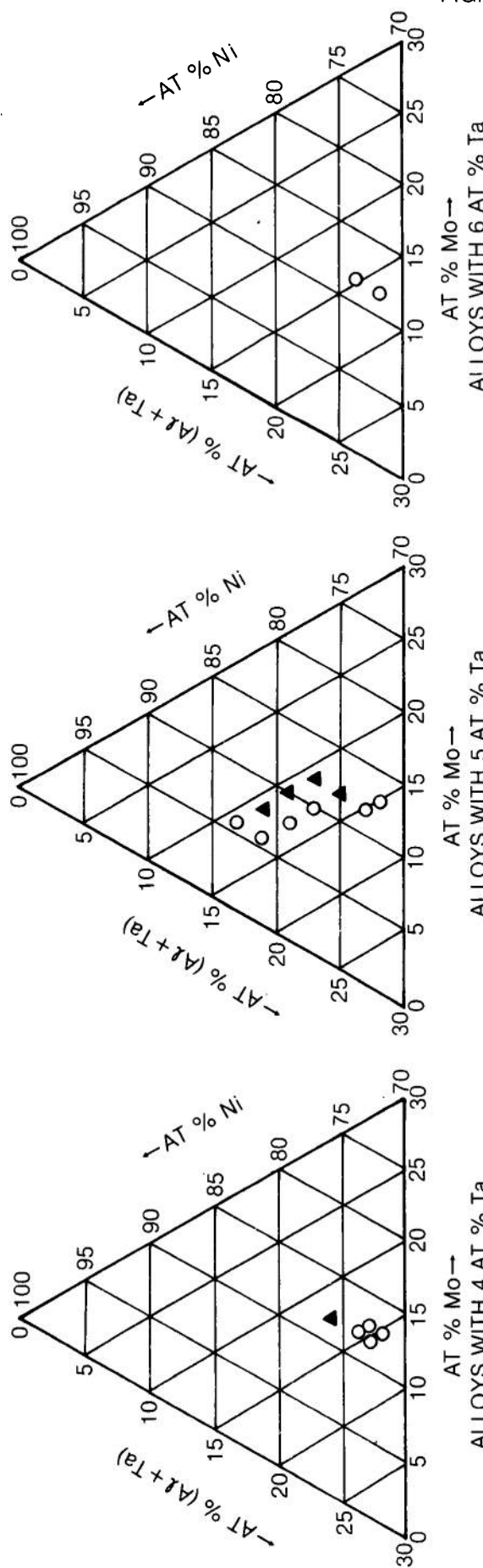
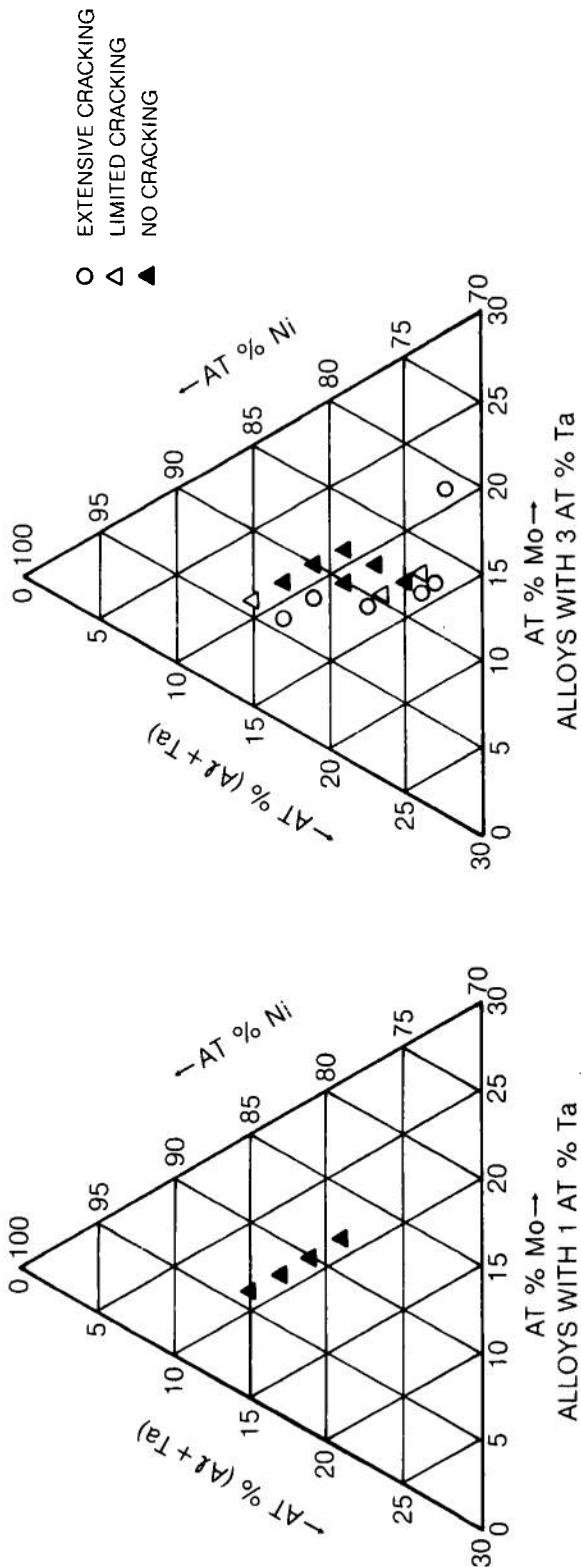


FIG. 29

## SURFACE OF VARIOUS ALLOY SPECIMENS AFTER LASER WELD CRACK TESTING

OVERLAPPING PASS BEAD-ON-PLATE LASER WELDS AT 1 MW/cm<sup>2</sup> BEAM INTENSITY  
AND 5 cm/s BEAM TRAVERSE SPEED



(A) ALLOY 10-12-3, CRACK FREE

7 mm

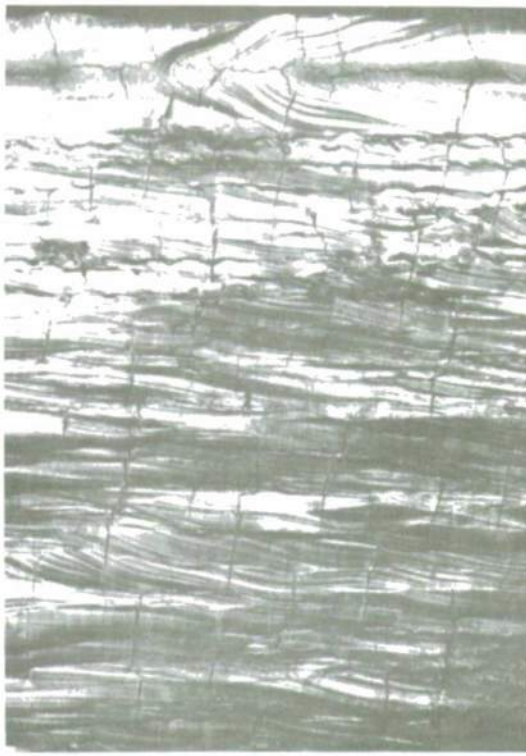


(C) RENE 62, NO SURFACE CRACKS

7.5 mm



(B) ALLOY 9.5-9.5-0-3.5, TRANSVERSE SURFACE CRACKS

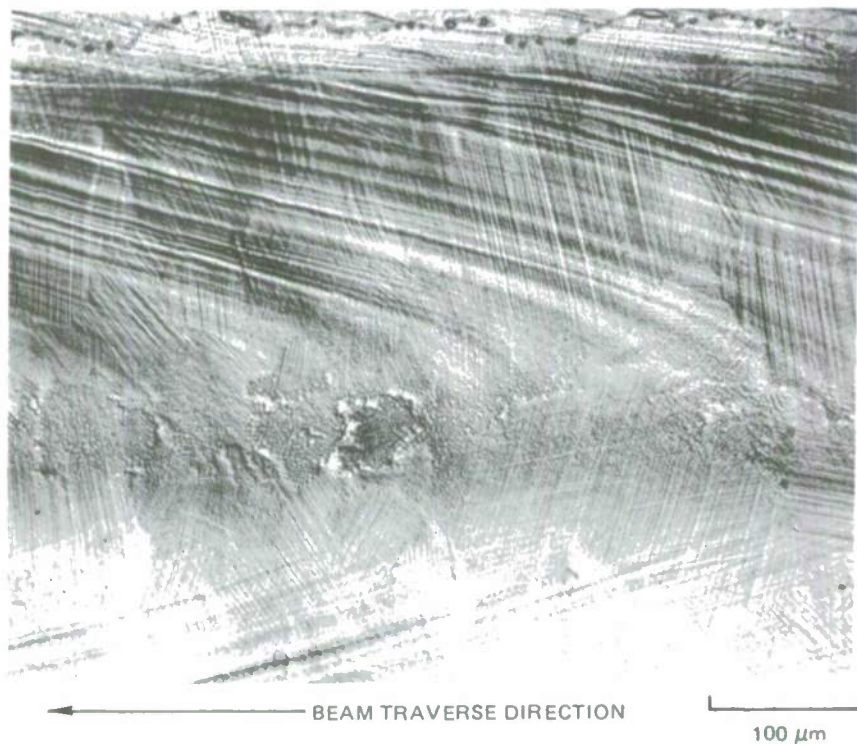


(D) RENE 125, LONGITUDINAL AND TRANSVERSE SURFACE CRACKS

7.5 mm

SLIP LINES ON FUSION ZONE SURFACE, ALLOY 8-12-3

LASER WELDED AT  $0.5 \text{ MW}/\text{CM}^2$  BEAM INTENSITY AND 25 CM/S BEAM TRAVERSE SPEED



TRANSVERSE SECTION OF WELD CRACK TEST SPECIMEN, ALLOY 8-12-3 (CRACK FREE)

BEAM TRAVERSE DIRECTION INTO PAGE. OVERLAPPING BEAD-ON-PLATE LASER WELDS MADE ON AS-CHILL-CAST  
SPECIMEN, 1 MW/cm<sup>2</sup> BEAM INTENSITY, 5 cm/s BEAM TRAVERSE SPEED.



CENTERLINE GRAIN BOUNDARY CRACKING

TRANSVERSE SECTION OF LASER WELD CRACK TEST SPECIMEN,  
ALLOY 9.5-9.5-0-3.5



R81-914346-8

FIG. 34

TRANSVERSE SECTION OF LASER WELD CRACK SPECIMEN, ALLOY 8-12-3

AREA IN FIGURE 29 SHOWING OVERALL GRAIN STRUCTURE OF FUSION ZONE



200 $\mu$ m  
79-08-34-18

R81-914346-8

FIG. 35

**TRANSVERSE SECTION OF LASER WELD CRACK SPECIMEN, ALLOY 8-12-3**  
AREA IN FIGURE 29 ILLUSTRATING REFINEMENT OF DENDRITIC STRUCTURE FROM CHILL CASTING (BOTTOM)  
TO OVERLAPPED FUSION ZONES (TOP)

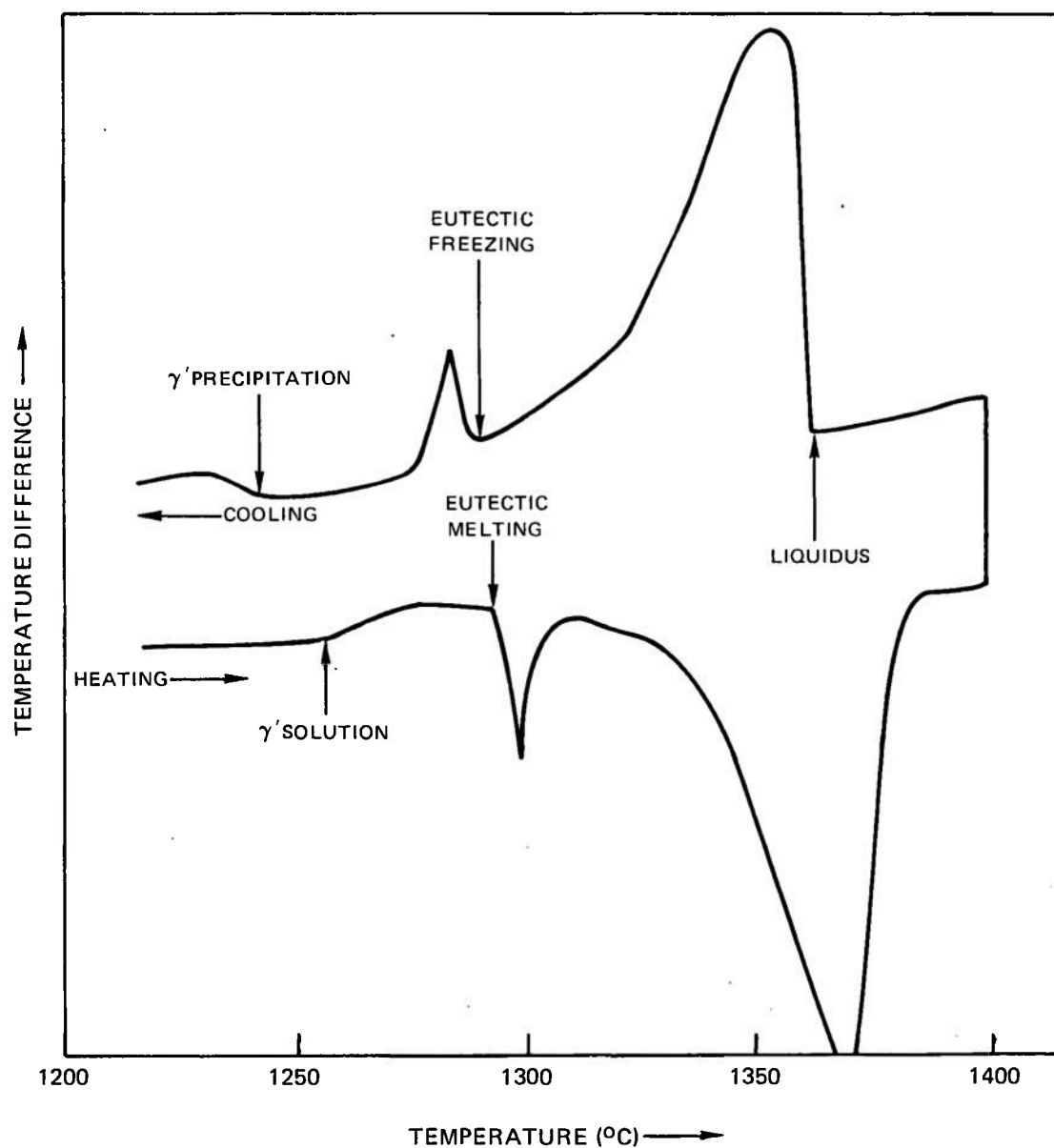


100 $\mu$  m

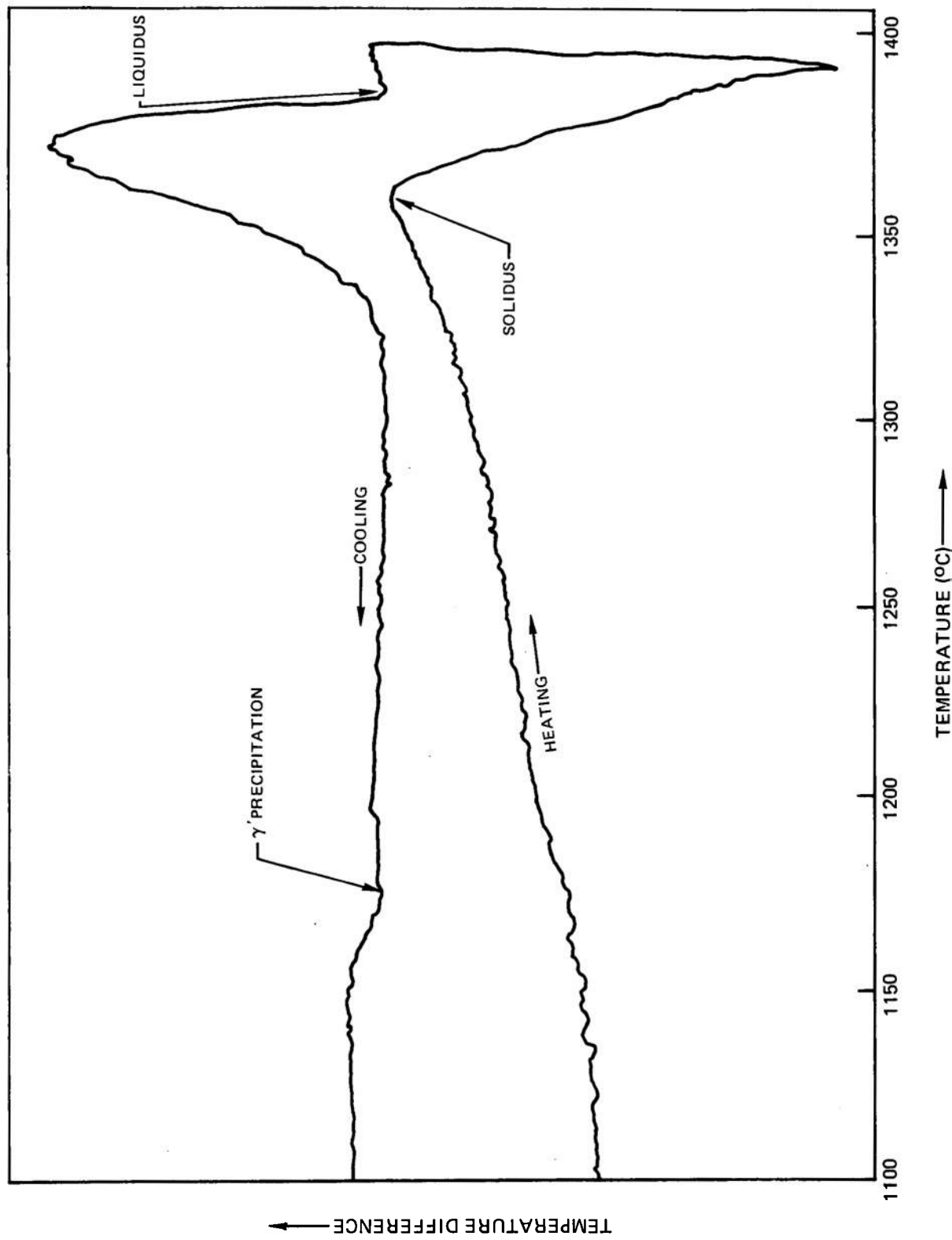
79-08-34-19

## DIFFERENTIAL THERMAL ANALYSIS (DTA) TRACE FROM ALLOY 10-12-3

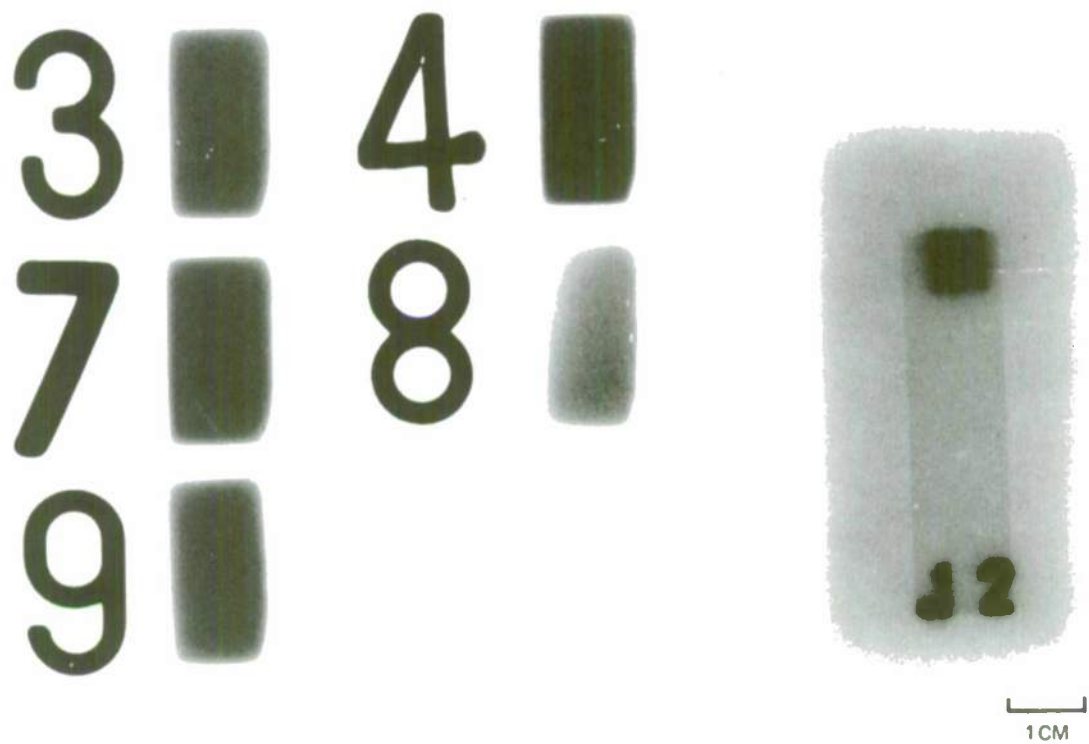
HEATING AND COOLING RATES, 5°C/min. PURE NICKEL STANDARD



## DIFFERENTIAL THERMAL ANALYSIS (DTA) TRACE FROM ALLOY 12-11

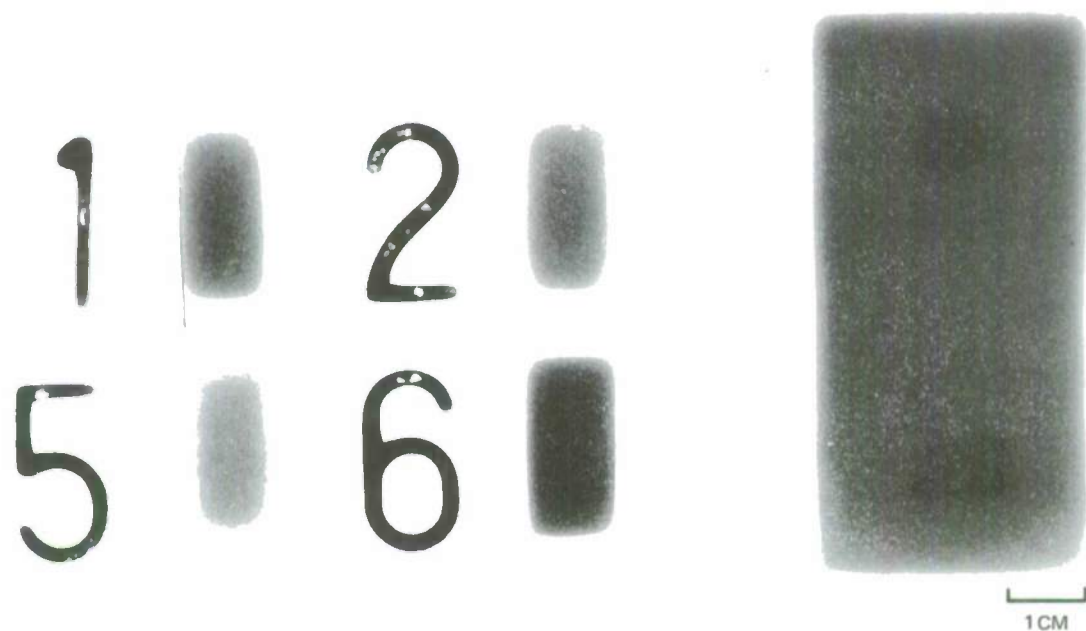
HEATING AND COOLING RATES,  $5^{\circ}\text{C}/\text{min}$ . PURE NICKEL STANDARD

RADIOGRAPH OF 3.6 MM (0.14 IN) THICK PIECES SECTIONED FROM DISK 1-8  
SEE FIGURE 25 FOR LIGHT MICROGRAPH



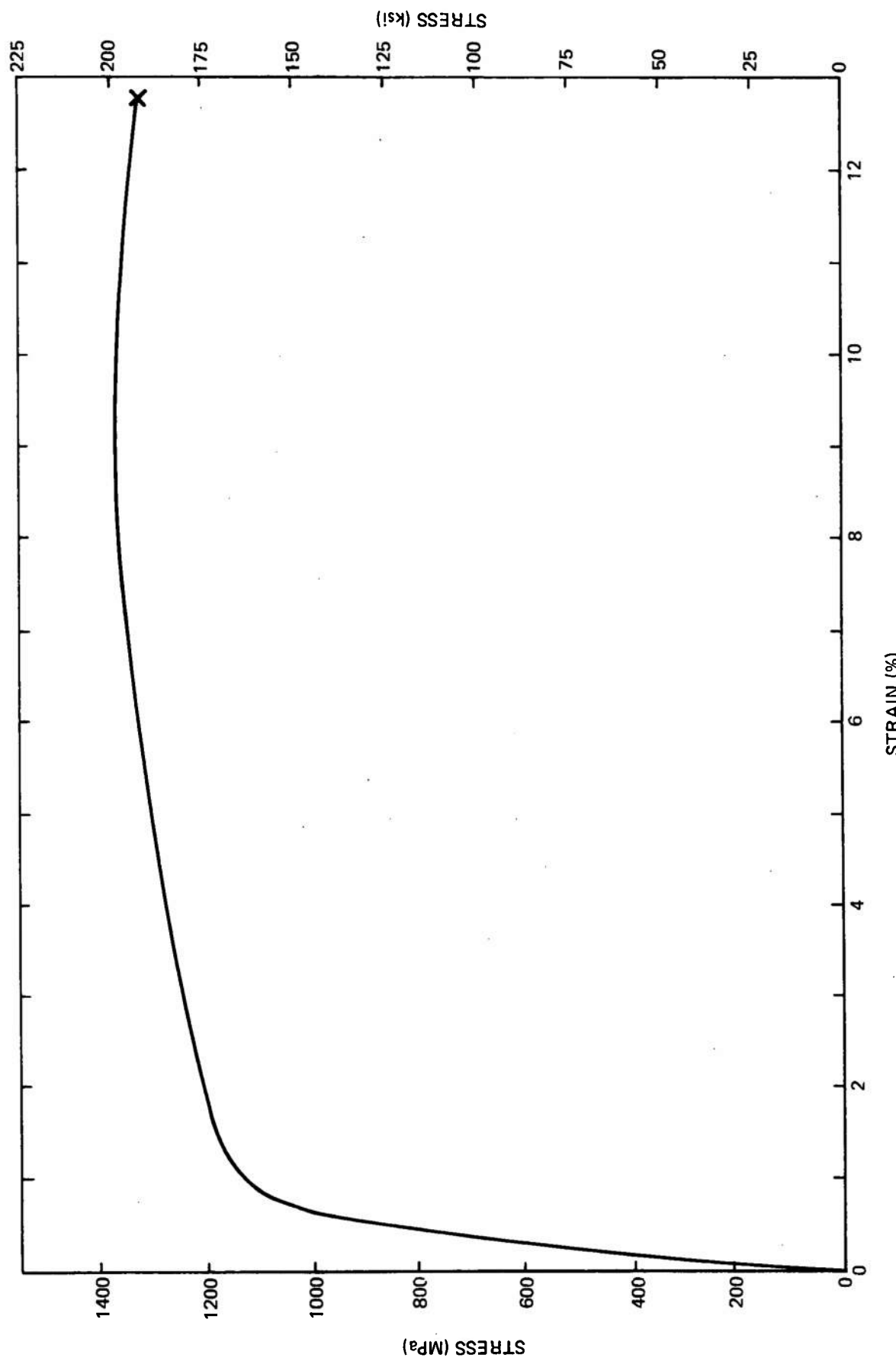
RADIOGRAPH OF 6.4 MM (0.25 IN) THICK PIECES SECTIONED FROM DISK 1-8

SEE FIGURE 25 FOR LIGHT MICROGRAPH



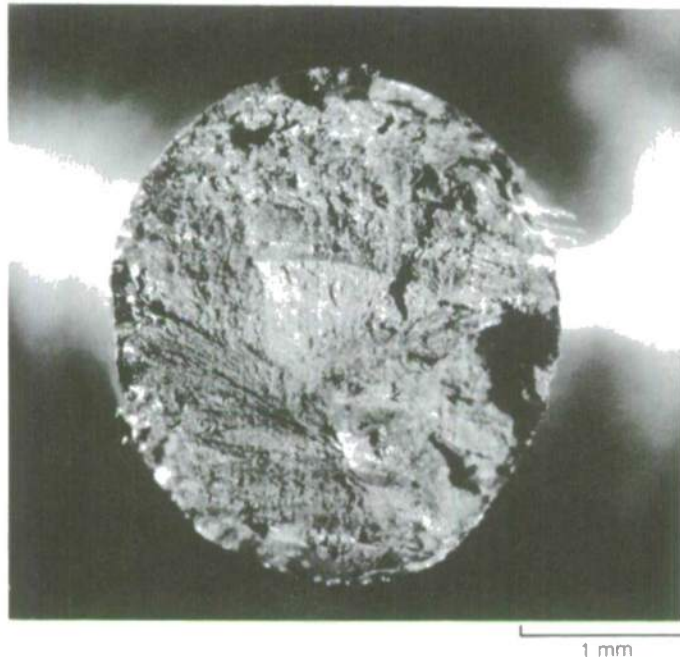
## ENGINEERING STRESS-STRAIN CURVE OF TENSILE SPECIMEN FROM DISK 1-8

AMBIENT TEMPERATURE TEST, AXIAL SPECIMEN ORIENTATION (LOAD DIRECTION PARALLEL TO Z  
DIRECTION, THE DISK ROTATIONAL AXIS). YIELD STRENGTH AT 0.2% OFFSET: 1110 MPa (161 ksi).  
ULTIMATE TENSILE STRENGTH: 1352 MPa (196 ksi). ELONGATION: 12.8 %



**TENSILE FRACTURE SURFACES OF DISK 11-2, ALLOY 11-12-0-0-5**

(LOAD AXIS PARALLEL TO DISK ROTATIONAL AXIS)

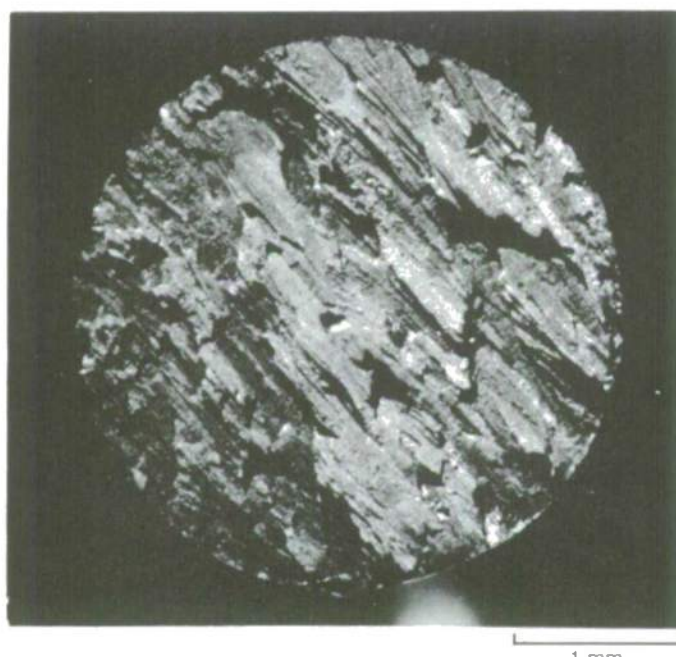


a) AMBIENT TEMPERATURE TEST SPECIMEN

$$\sigma_{ys} = 1096 \text{ MPa (159 ksi)}$$

$$\sigma_{UTS} = 1413 \text{ MPa (205 ksi)}$$

$$\epsilon_f = 3.7\%$$



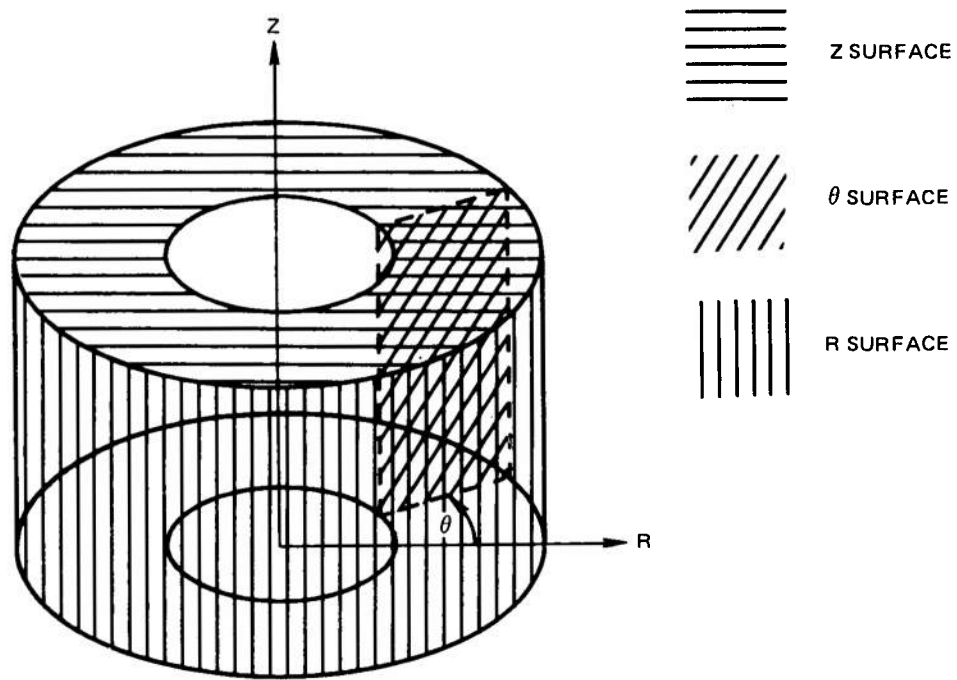
b) 704° (1300°F) TEST SPECIMEN

$$\sigma_{ys} = - \text{ (BRITTLE FRACTURE)}$$

$$\sigma_{UTS} = 552 \text{ MPa (80 ksi)}$$

$$\epsilon_f = < 1\%$$

SCHEMATIC DRAWING OF DISK 1-8, SHOWING ORIENTATION OF  
CYLINDRICAL COORDINATES



R81-914346-8

FIG. 43

R FACE NEAR OUTER SURFACE, DISK 1-8, ALLOY 8-12-3



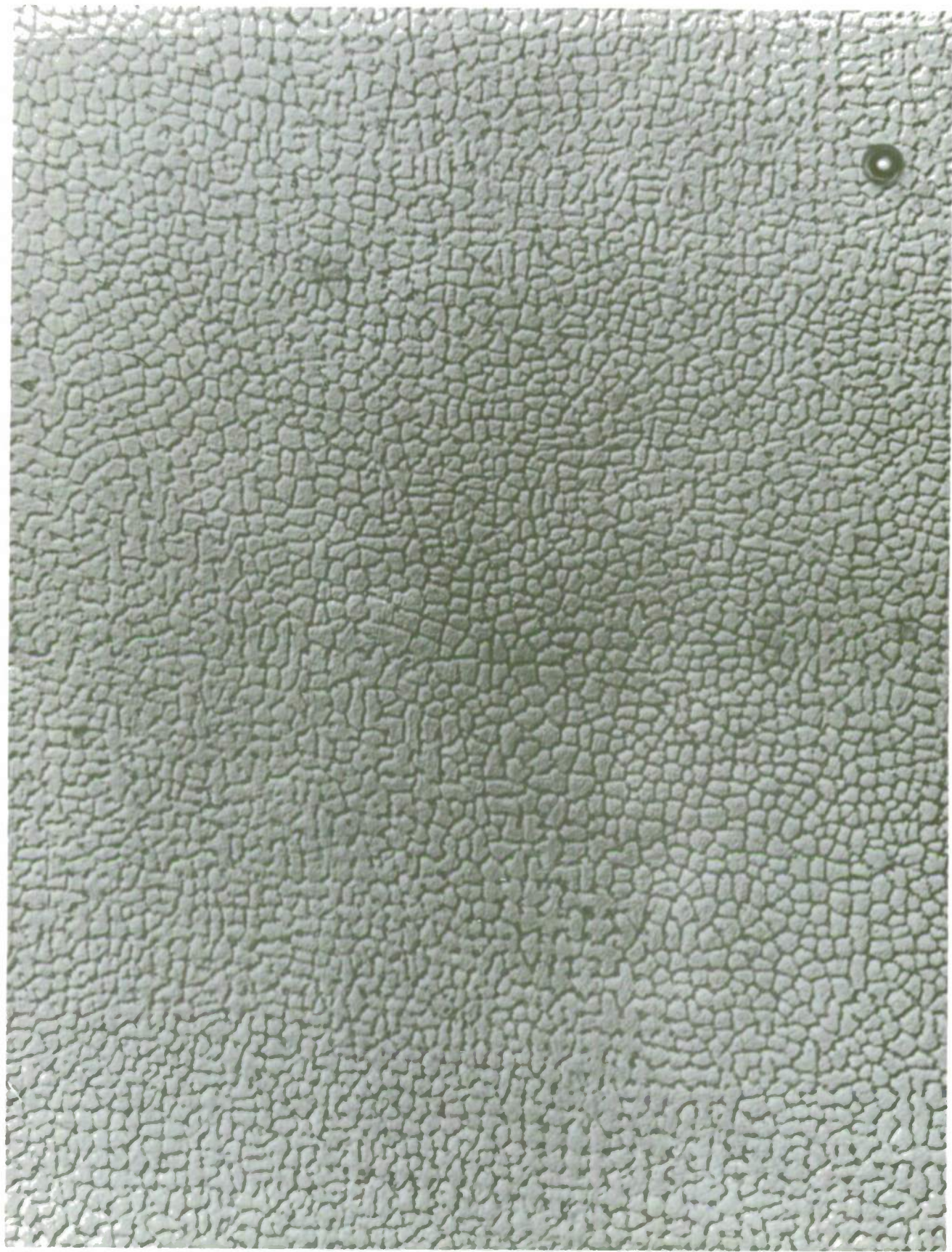
200 $\mu$ m

79-08-34-1

R81-914346-8

FIG. 44

R FACE NEAR OUTER SURFACE, DISK 1-8, ALLOY 8-12-3



20 $\mu$ m  
79-08-34-2

R81-914346-8

FIG. 45

Z FACE NEAR STAINLESS STEEL SUBSTRATE, DISK 1-8, ALLOY 8-12-3



200 $\mu$ m  
79-08-34-3

R81-914346-8

FIG. 46

Z FACE NEAR STAINLESS STEEL SUBSTRATE, DISK 1-8, ALLOY 8-12-3



20 $\mu$ m

79-08-34-4

R81-914346-8

FIG. 47

Z FACE NEAR MID-RADIUS, DISK 1-8, ALLOY 8-12-3



200 $\mu$ m

79-08-34-5

R81-914346-8

FIG. 48

Z FACE NEAR MID-RADIUS, DISK 1-8, ALLOY 8-12-3



20 $\mu$ m

79-08-34-6

R81-914346-8

FIG. 49

Z FACE NEAR OUTER SURFACE, DISK 1-8, ALLOY 8-12-3



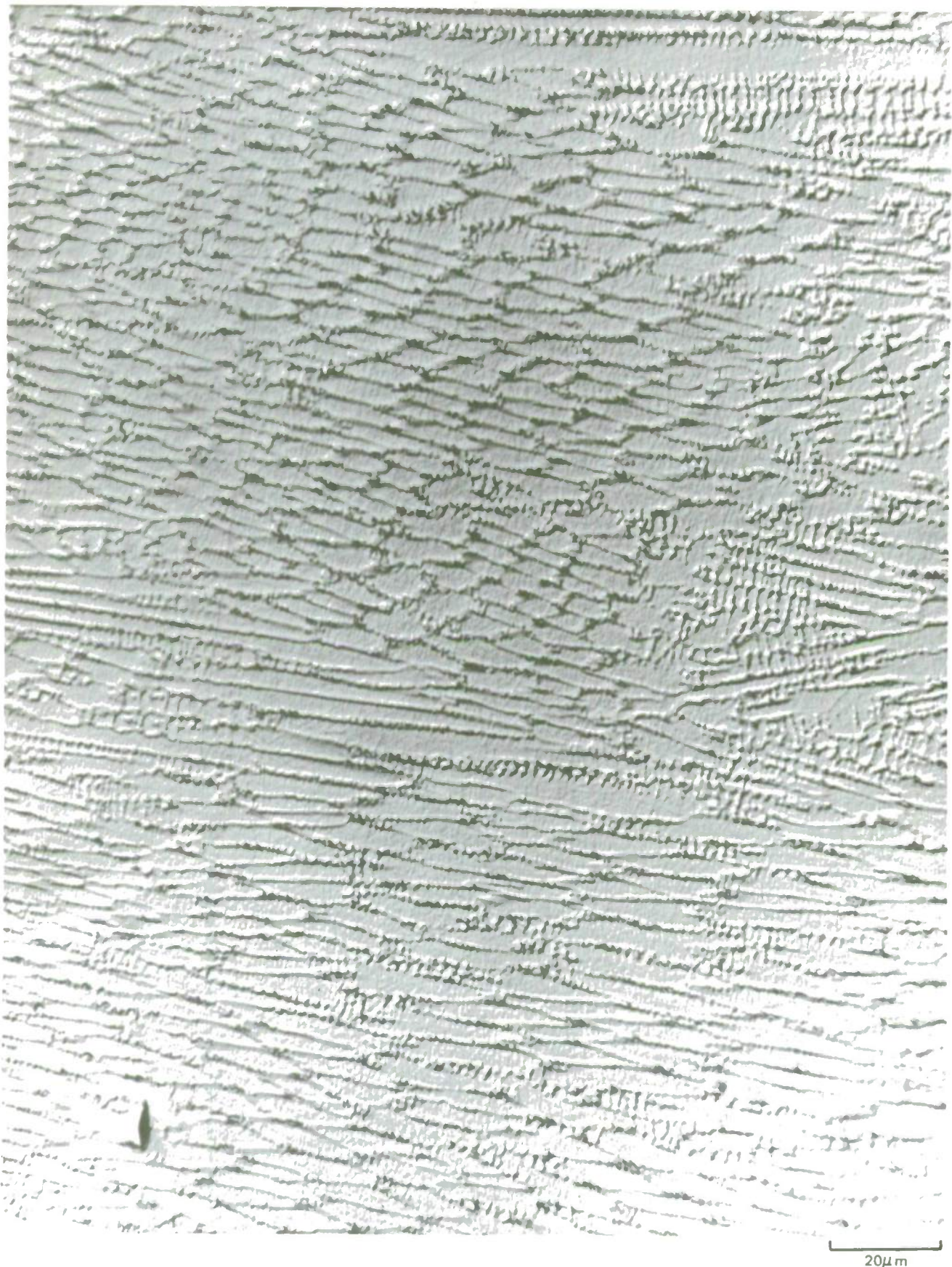
200 $\mu$ m

79-08-34-7

R81-914346-8

FIG. 50

Z FACE NEAR OUTER SURFACE, DISK 1-8, ALLOY 8-12-3



20 $\mu$ m

79-08-34-8

R81-914346-8

FIG. 51

θ FACE NEAR STAINLESS STEEL SUBSTRATE, DISK 1-8, ALLOY 8-12-3



200 $\mu$ m

79-08-34-9

R81-914346-8

FIG. 52

$\theta$  FACE NEAR OUTER SURFACE, DISK 1-8, ALLOY 8-12-3



200 $\mu$ m

79-08-34-10

R81-914346-8

FIG. 53

⊖ FACE NEAR OUTER SURFACE, DISK 11-2, ALLOY 11-12-0-0-5



81-2-115-15

R81-914346-8

FIG. 54

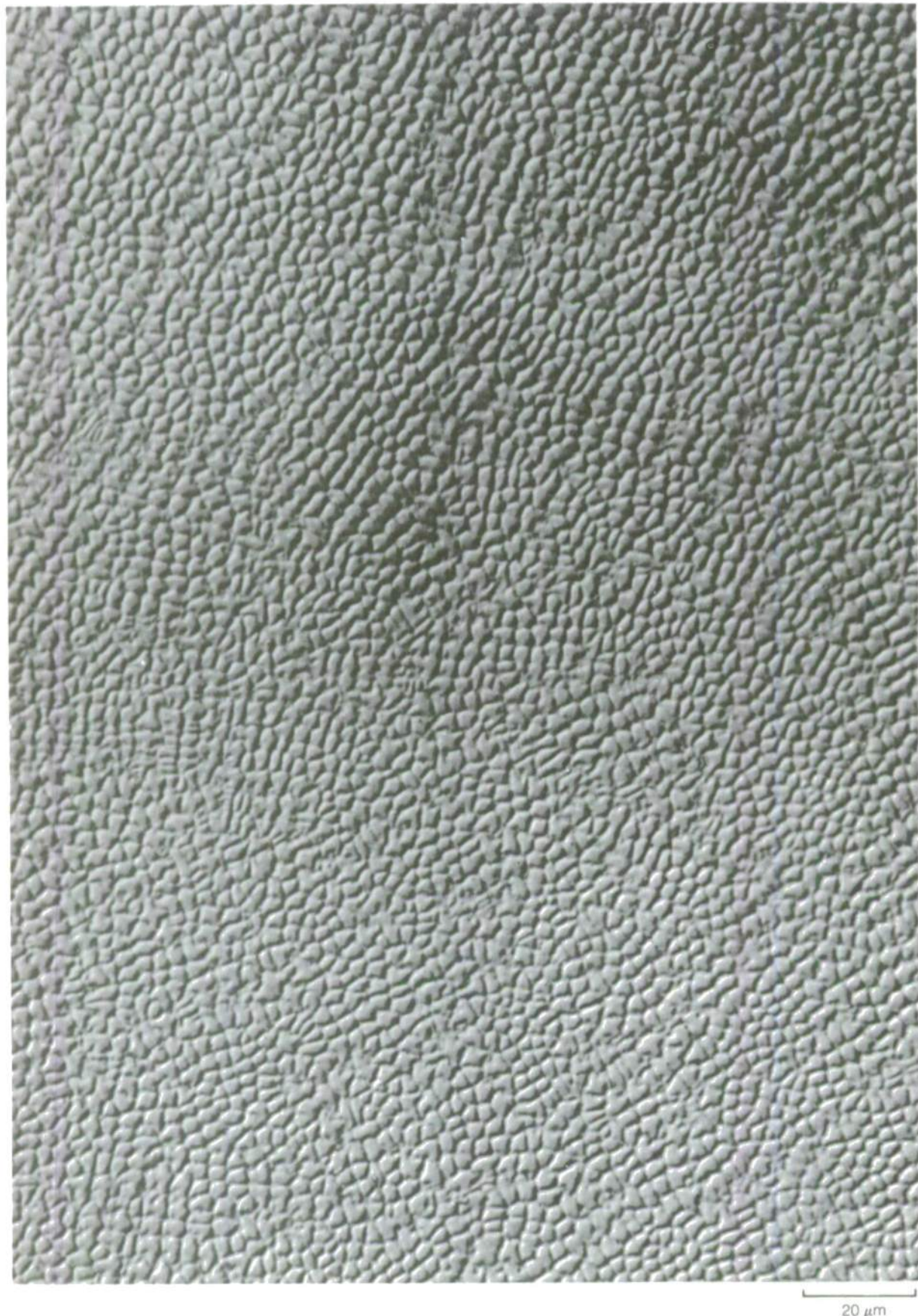
⊖ FACE NEAR OUTER SURFACE, DISK 11-2, ALLOY 11-12-0-0-5



20  $\mu\text{m}$

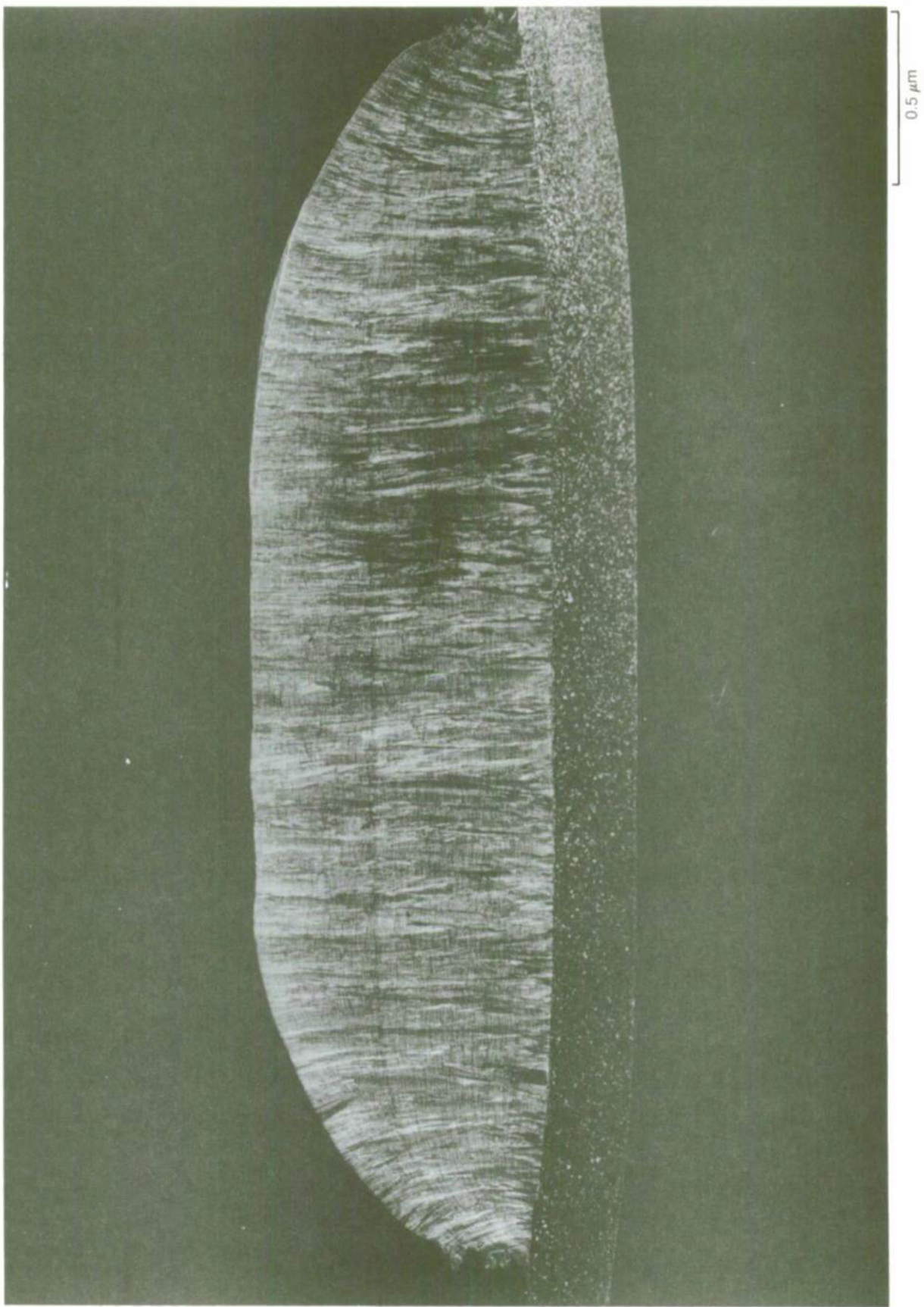
81-2-115-11

R FACE NEAR OUTER SURFACE, DISK 11-2, ALLOY 11-12-0-0-5



20  $\mu\text{m}$

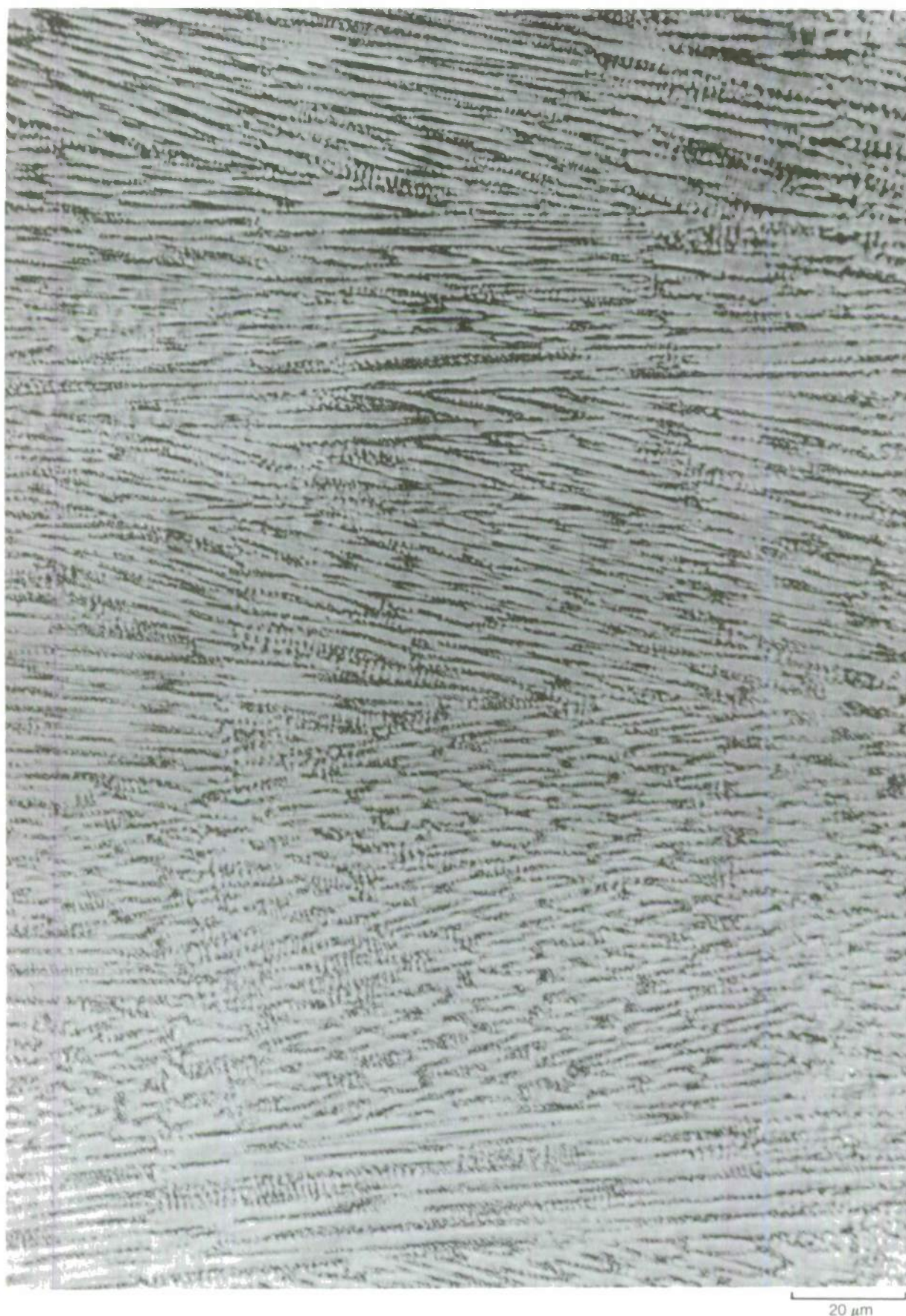
GRAIN STRUCTURE OF MACROETCHED CROSS-SECTION, DISK 9-1, ALLOY 12-15



R81-914346-8

FIG. 57

⊖ FACE NEAR OUTER SURFACE, DISK 9-1, ALLOY 12-15



20 μm

81-2-115-18

## R FACE NEAR OUTER SURFACE, DISK 9-1, ALLOY 12-15

20  $\mu\text{m}$ 

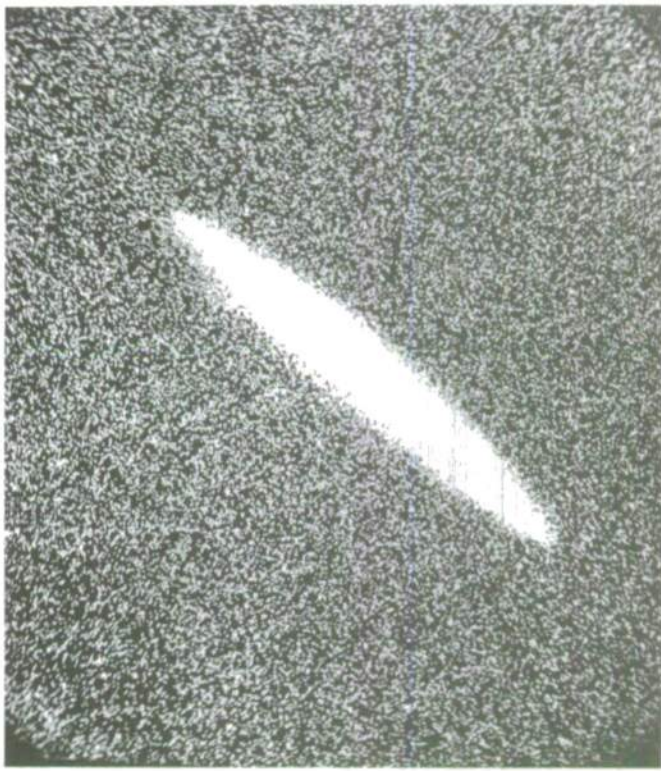
81-2-115-19

ELECTRON MICROPROBE CHARACTERIZATION OF CERAMIC INCLUSION IN  
AS-LAYERGLAZED DISK 9-1, ALLOY 12-15



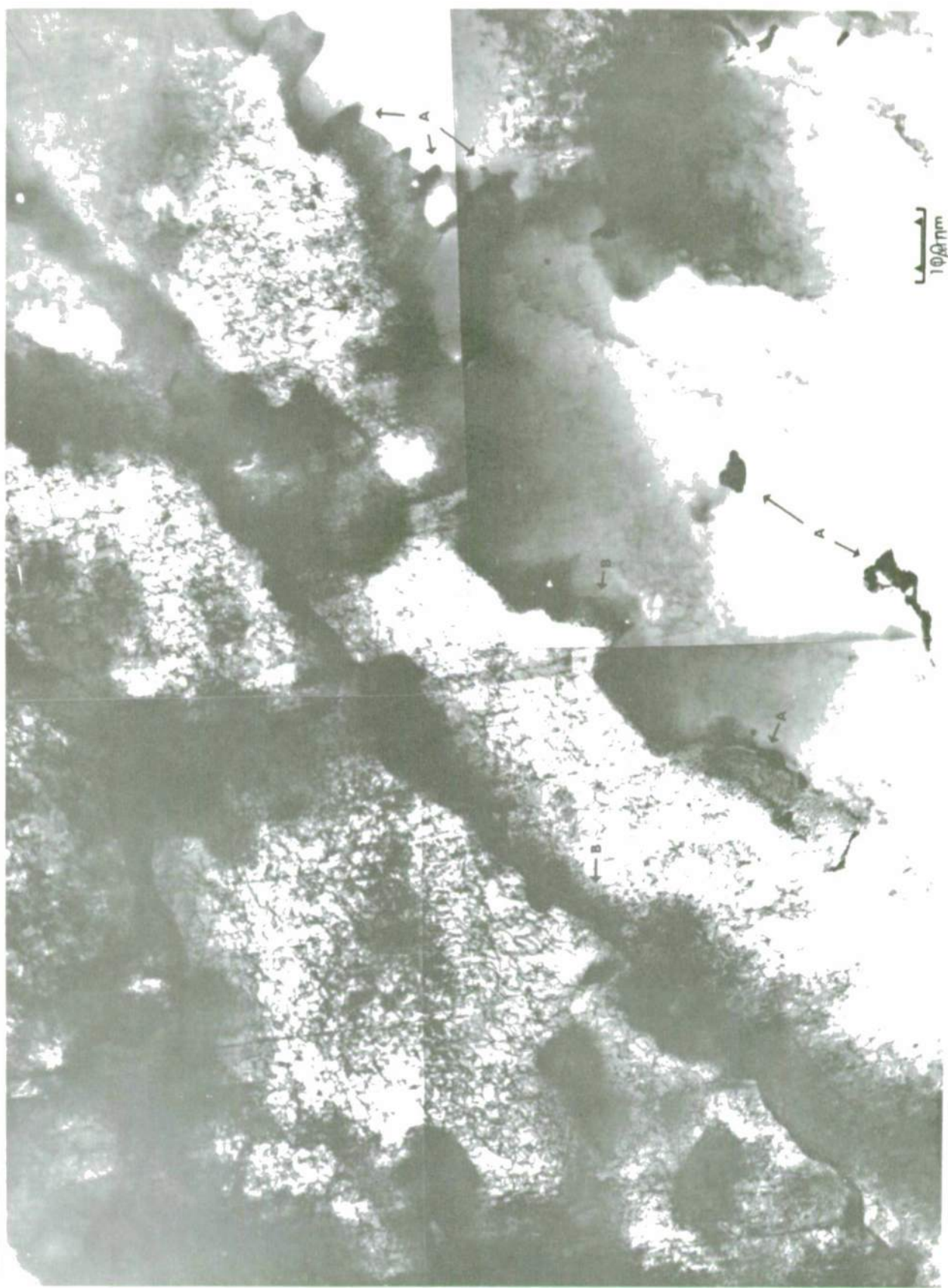
a) SECONDARY ELECTRON IMAGE

10  $\mu\text{m}$

b) ALUMINUM  $\text{K}\alpha$  IMAGEc) OXYGEN  $\text{K}\alpha$  IMAGEd) CALCIUM  $\text{K}\alpha$  IMAGE

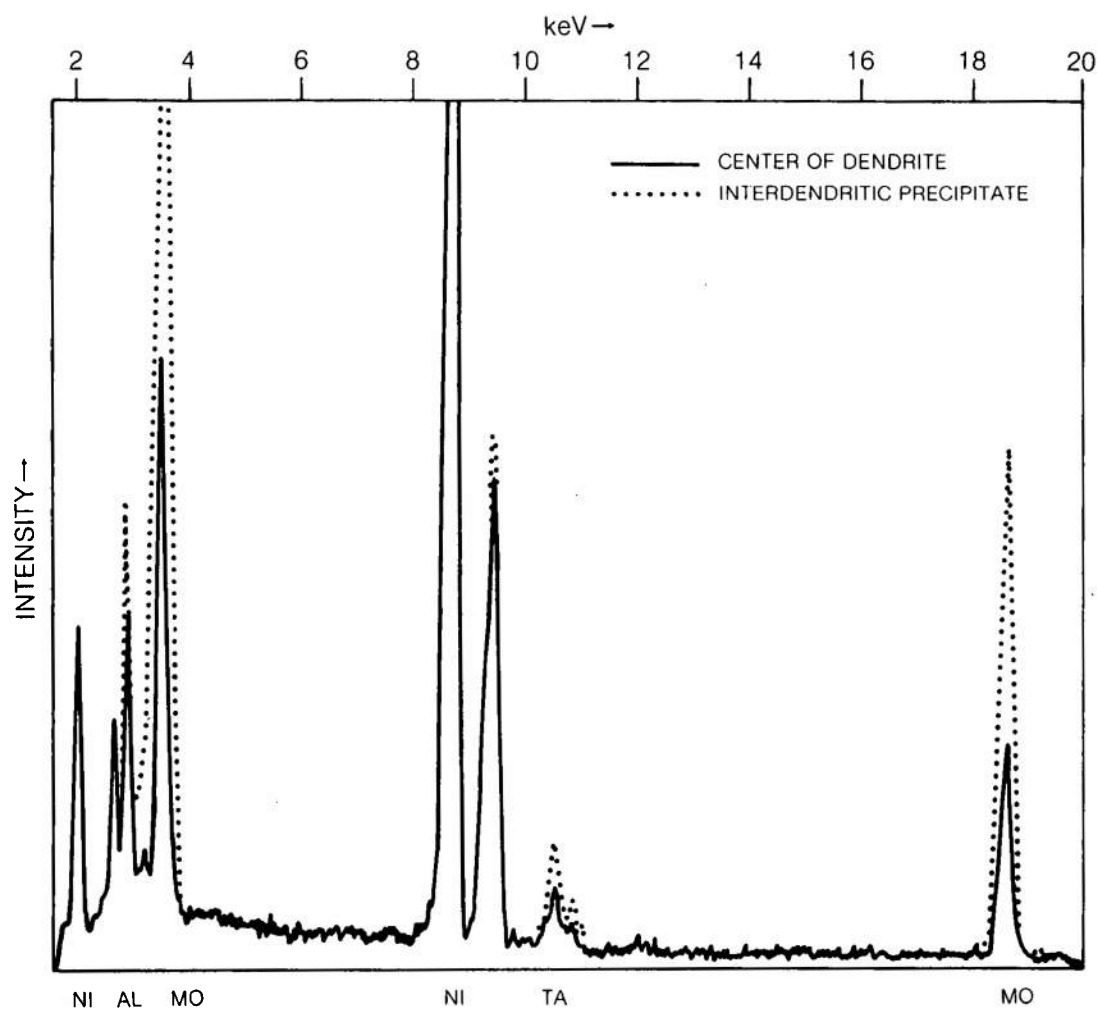
**TRANSMISSION ELECTRON MICROGRAPH OF R FACE, DISK 1-8, ALLOY 8-12-3**

DENDRITIC GROWTH DIRECTION IS INCLINED TO THE FOIL NORMAL IN THIS REGION. EXAMPLES OF A POLYCRYSTALLINE INTERDENDRITIC PHASE ARE MARKED BY "A". SOME OF THE DENSE DISLOCATION TANGLES COMPRISING SUBBOUNDARIES ARE MARKED BY "B". NO GRAIN BOUNDARIES ARE PRESENT IN THE MATRIX IN THIS FIELD OF VIEW.

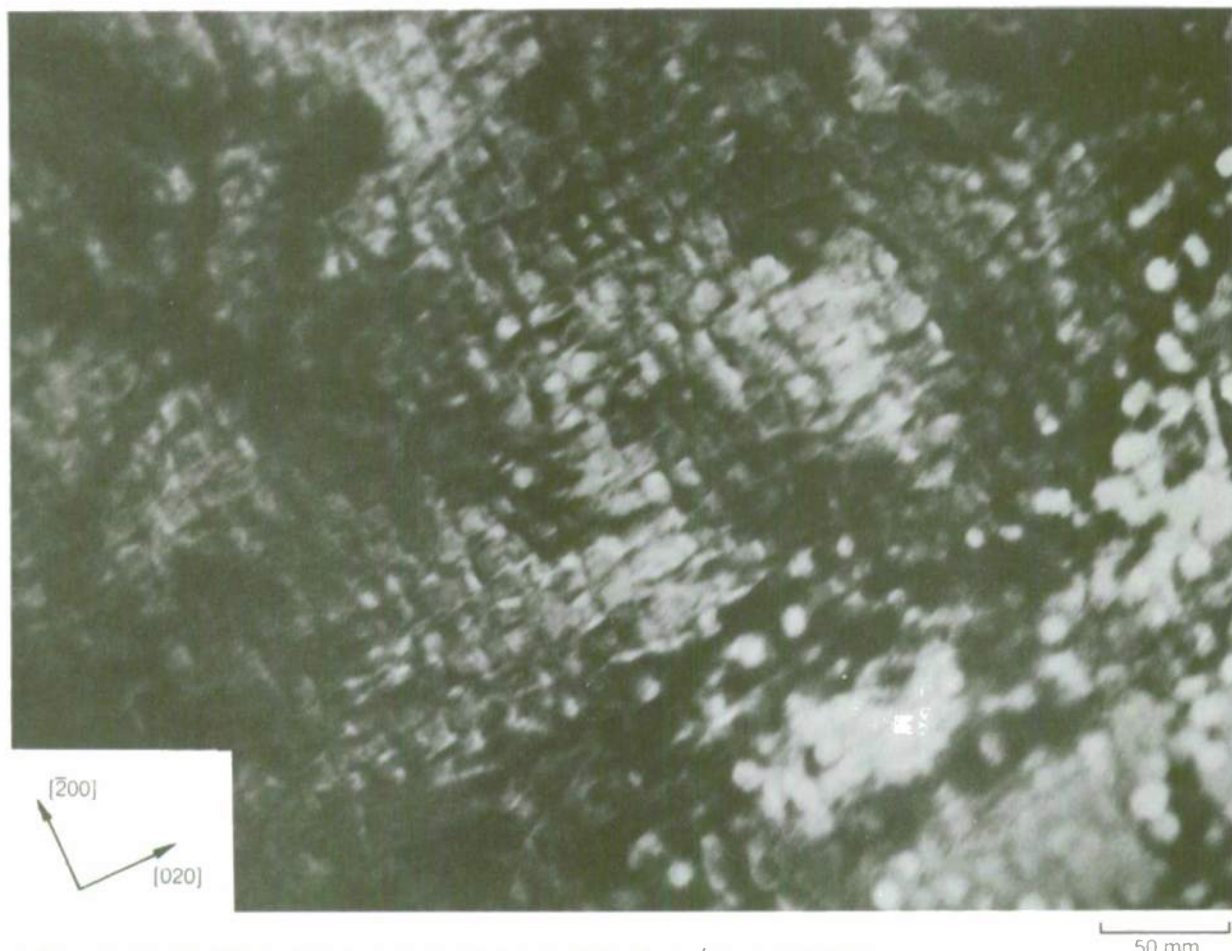
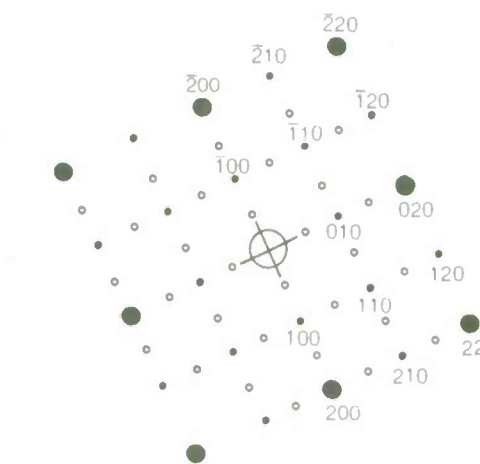


**CHARACTERISTIC X-RAY SPECTRA SHOWING THE QUALITATIVE COMPOSITIONAL  
DIFFERENCE BETWEEN THE DENDRITE CENTER AND AN INTERDENDRITIC  
PRECIPITATE, AS-LAYERGLAZE-FABRICATED DISK 1-8, ALLOY 8-12-3**

120 kV, ~2 nm SPOT SIZE  
TIME 98 sec 0-20 KEV: 10 EV/CH PRST: 100 sec

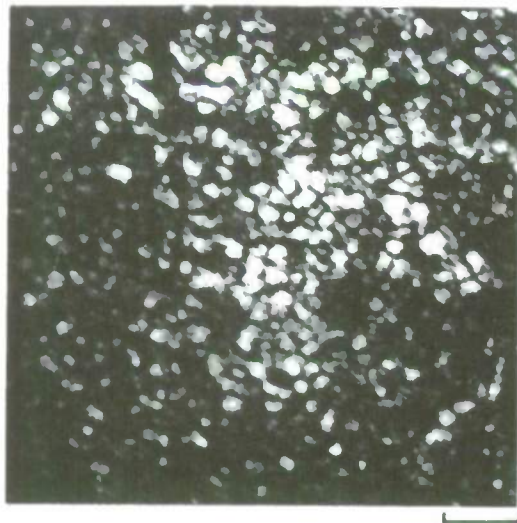


## AS-LAYERGLAZED DISK 1-8, ALLOY 8-12-3

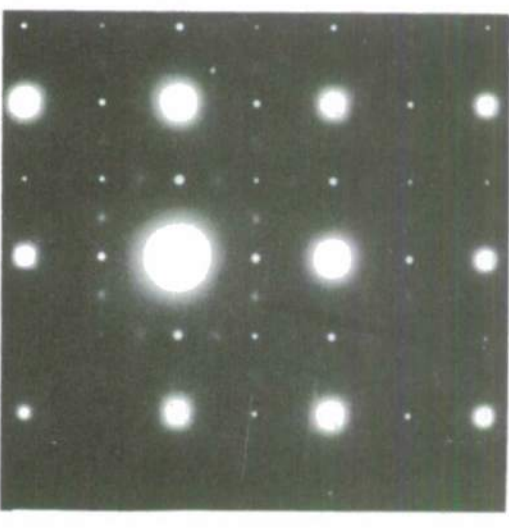
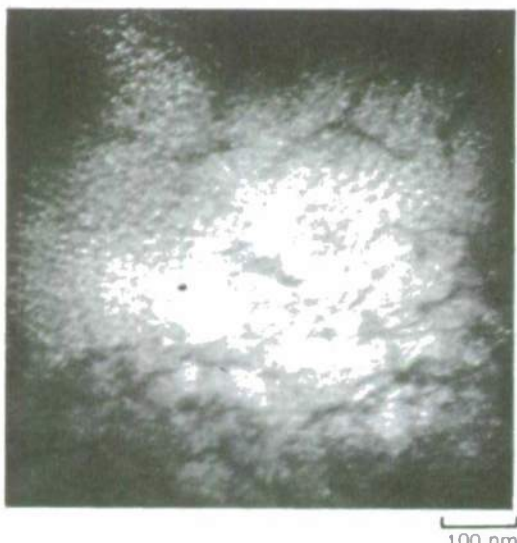
a) MULTI-BEAM BRIGHT FIELD IMAGE OF CUBOIDAL  $\gamma'$  IN  $\gamma$  MATRIXb) ASSOCIATED SELECTED AREA DIFFRACTION PATTERN,  
[001] ZONE AXISc) SCHEMATIC DIAGRAM  
OF SADP IN (B)

- $\gamma + \gamma'$
- $\gamma'$
- SHORT RANGE ORDER

DARK FIELD IMAGES AND ASSOCIATED SADP's, AS-LAYERGLAZE-FABRICATED DISK 1-8, ALLOY 8-12-3

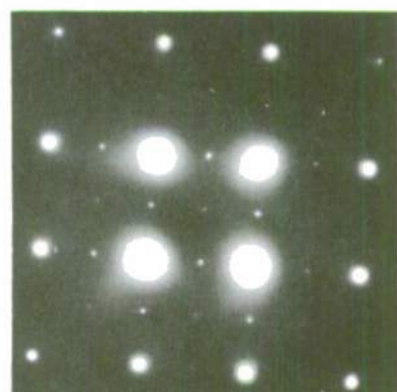
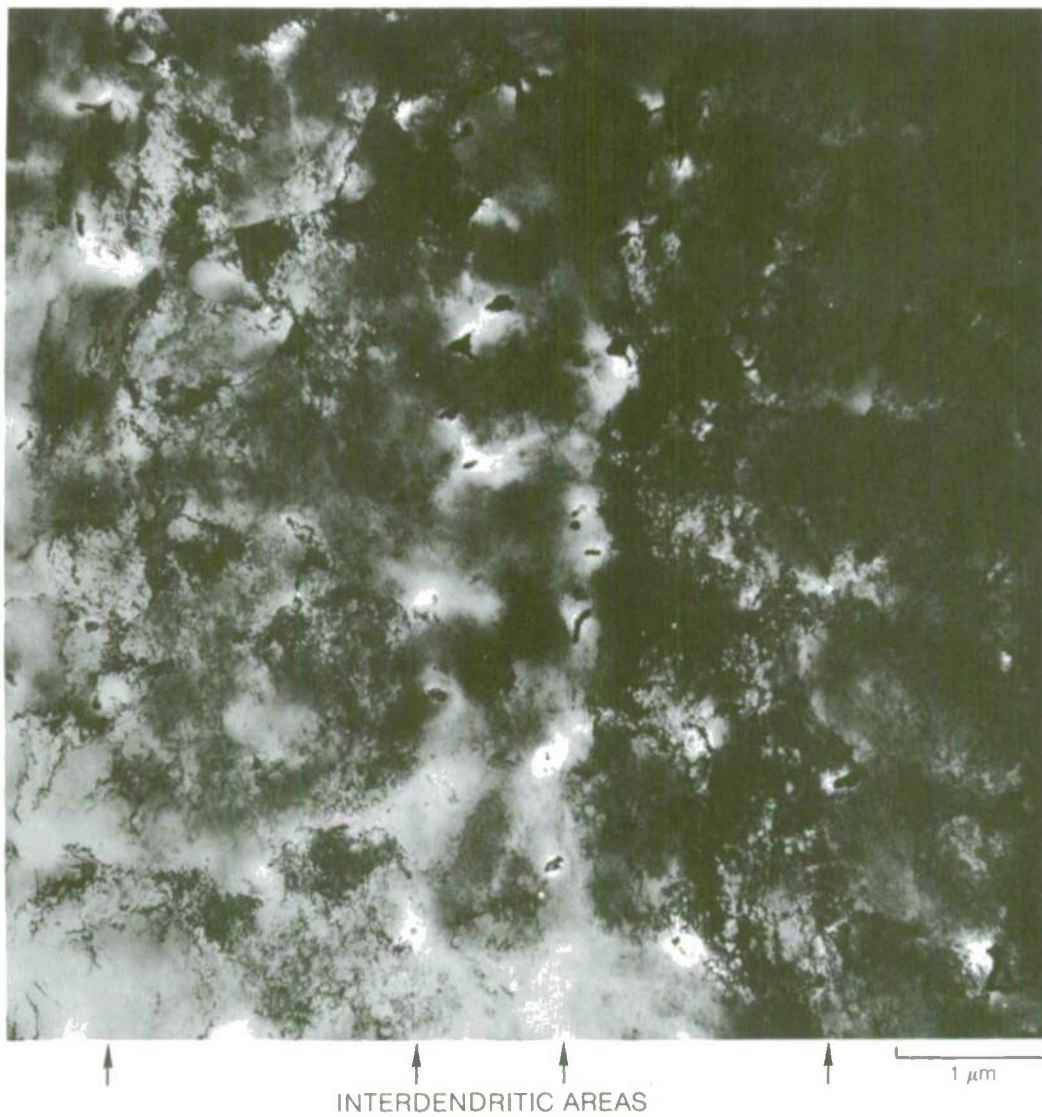


- DARK FIELD IMAGE AND ASSOCIATED SADP.  
IMAGE FORMED FROM SUPERIMPOSED  $\gamma'$  AND SRO SPOTS MARKED BY POINTER



- DARK FIELD IMAGE AND ASSOCIATED SADP.  
IMAGE FORMED FROM SRO SPOT IN 1-1/2-0 POSITION, MARKED BY POINTER

**AS-LAYERGLAZED MICROSTRUCTURE AND ASSOCIATED SELECTED AREA DIFFRACTION PATTERN, DISK 9-4, ALLOY 11-12-0-0-5**



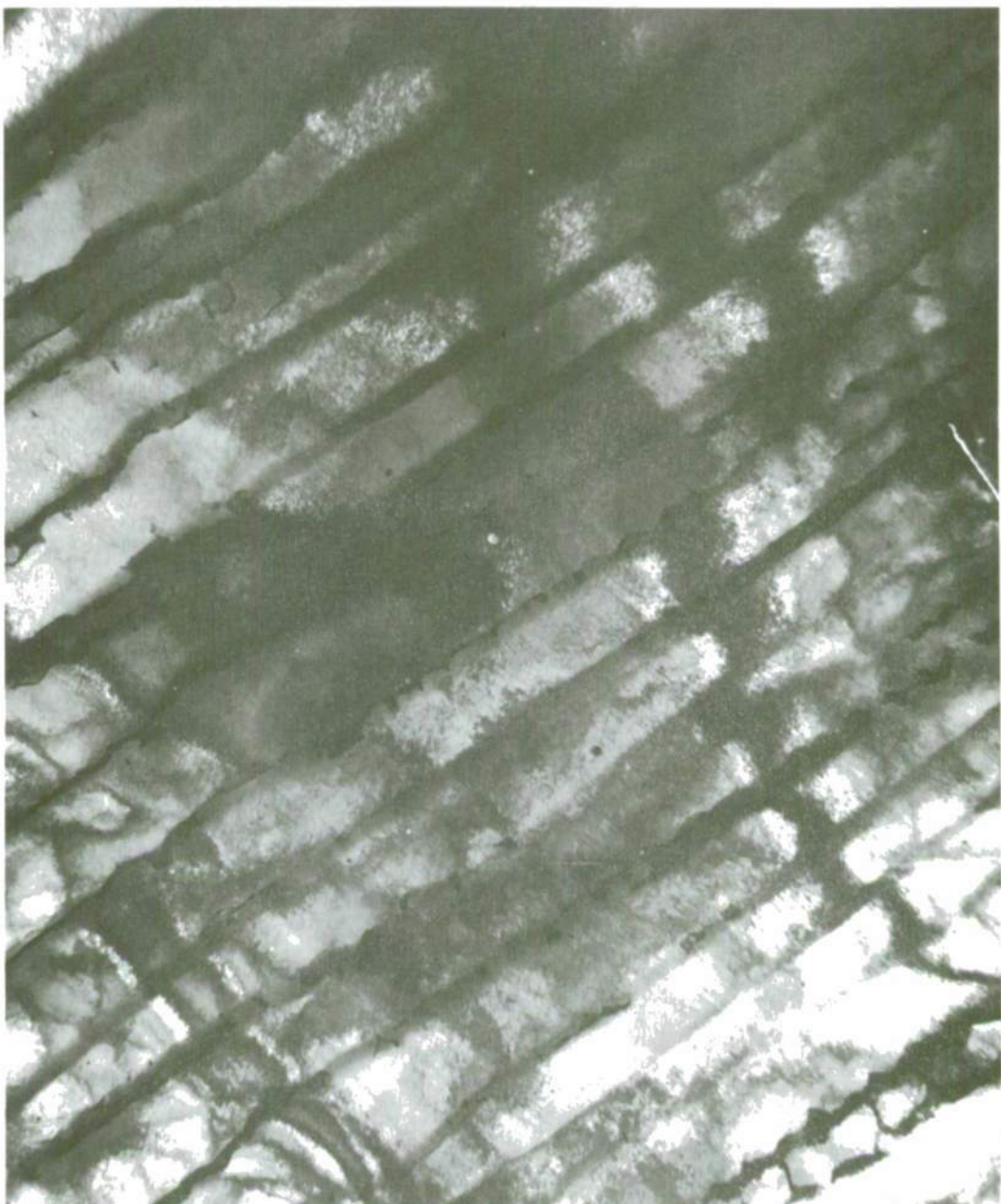
[001] ZONE AXIS

**AS-LAYERGLAZED MICROSTRUCTURE, DISK 9-4, ALLOY 11-12-0-0-5**

DARK FIELD,  $g = 200, \gamma + \gamma'$   
FINE CUBOIDAL  $\gamma'$  IN BRIGHT CONTRAST AT (A), BUT PRESENT THROUGHOUT THE FIELD OF  
VIEW EXCEPT WHERE INTERDENDRITIC PRECIPITATES ARE PRESENT (B)



AS-LAYERGLAZED MICROSTRUCTURE OF DISK 9-1, ALLOY 12-15



↙ {111} SLIP TRACES

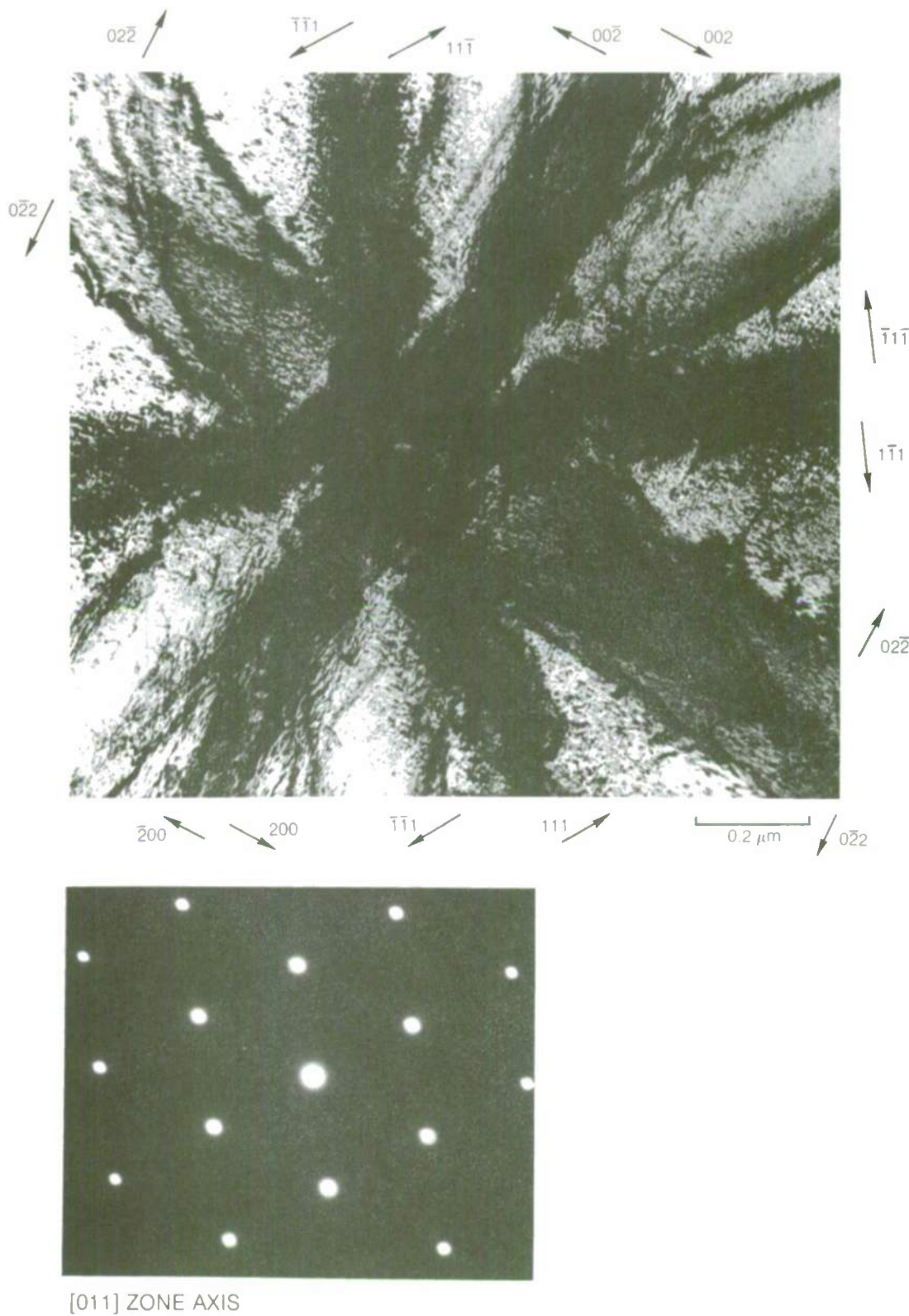
2  $\mu\text{m}$

## AS-LAYERGLAZED MICROSTRUCTURE OF DISK 9-1, ALLOY 12-15



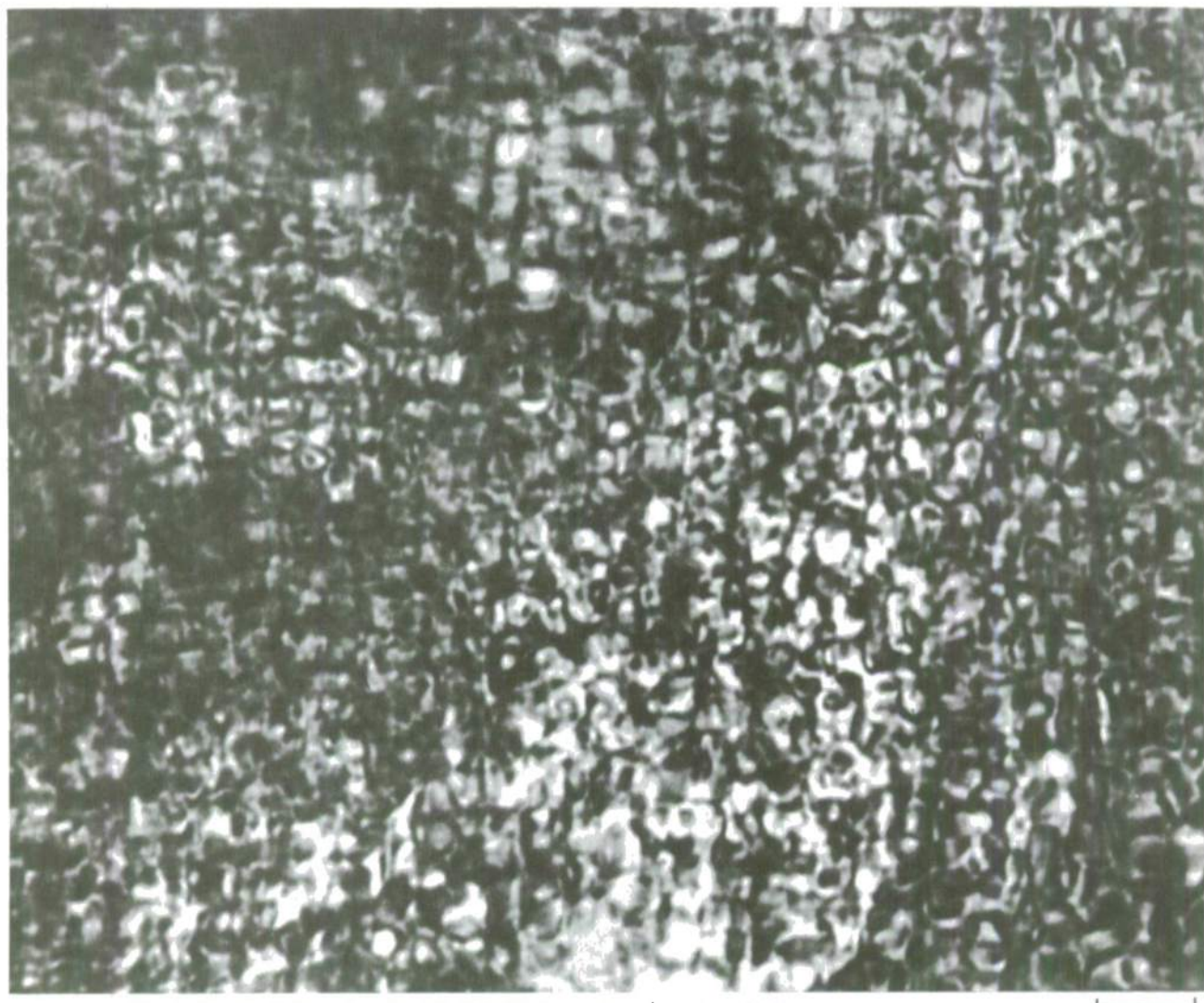
**[011] BEND CENTER IMAGE AND ASSOCIATED DIFFRACTION PATTERN  
IN AS-LAYERGLAZED DISK 9-1, ALLOY 12-15**

DESPITE THE WIDE VARIATION OF  $\gamma'$  IMAGE SHAPE AND CONTRAST WITH OPERATING REFLECTION ILLUSTRATED HERE, THE  $\gamma'$  IS HOMOGENEOUSLY DISTRIBUTED THROUGHOUT THE SPECIMEN

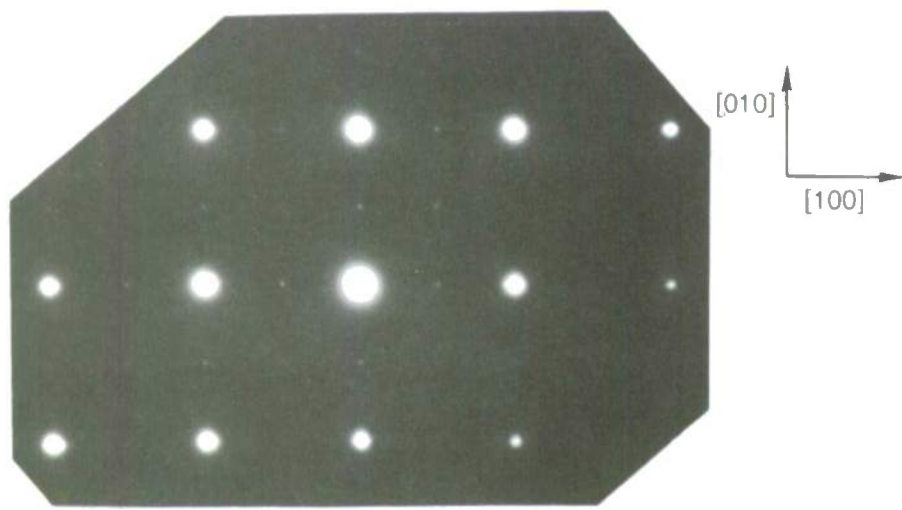


[011] ZONE AXIS

## AS-LAYERGLAZED DISK 9-1, ALLOY 12-15

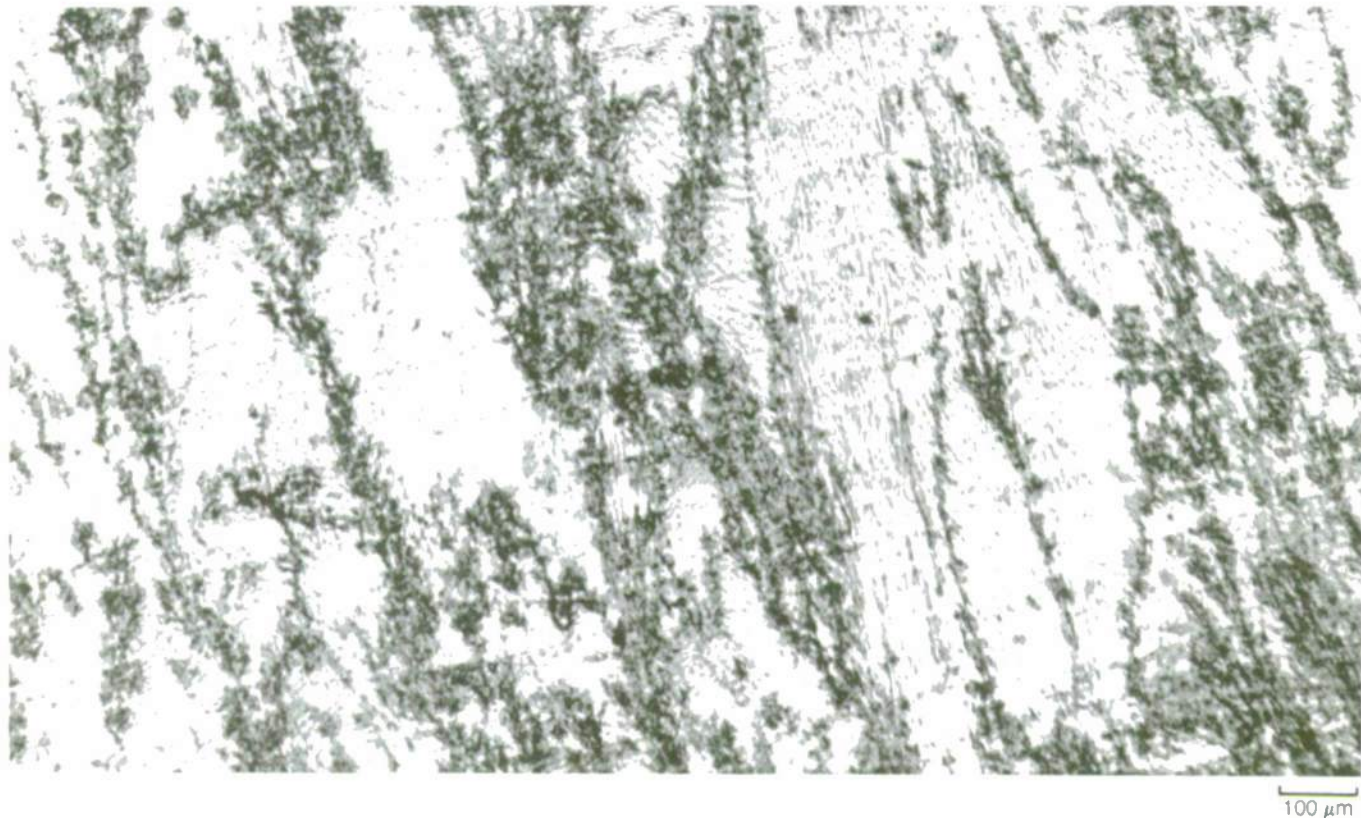
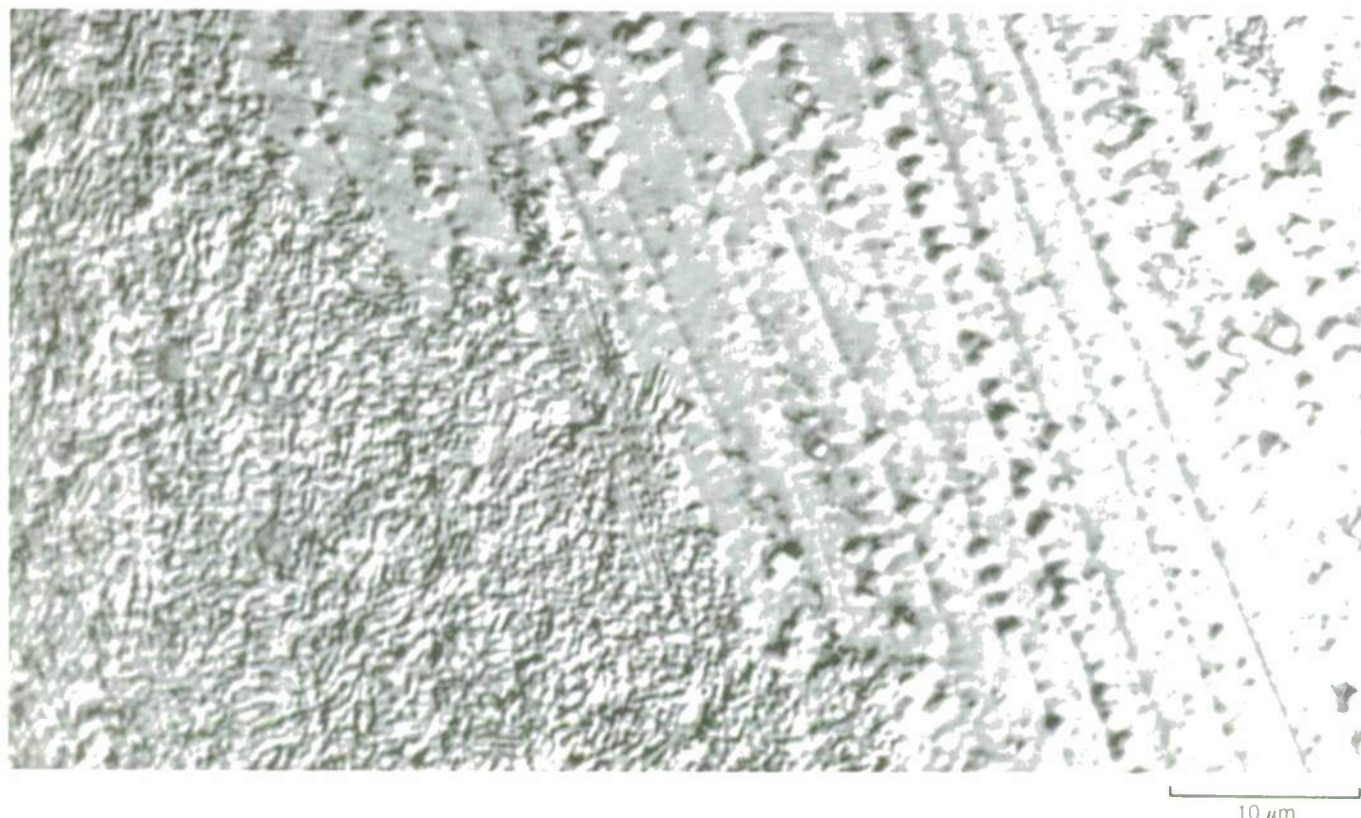
a) MULTI-BEAM BRIGHT FIELD IMAGE OF CUBOIDAL  $\gamma'$  IN  $\gamma$  MATRIX

25 nm

b) ASSOCIATED SELECTED AREA DIFFRACTION  
PATTERN, [001] ZONE AXIS

**CELLULAR TRANSFORMATION IN DISK 1-8, ALLOY 8-12-3**

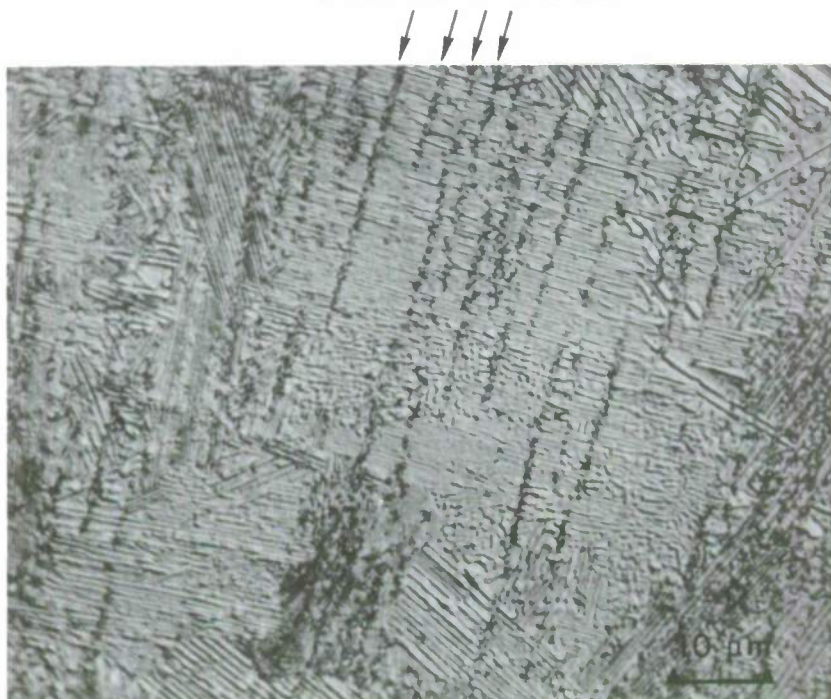
ANNEALED AT 760°C (1400°F) FOR 32 hours, THEN 704°C (1300°F) FOR 6 hours, AIR COOLED

100  $\mu\text{m}$ 10  $\mu\text{m}$

**EXTENSIVE CELLULAR TRANSFORMATION IN DISK 9-1, ALLOY 12-15  
(Ni-12 a/o Al-15 a/o Mo)**

ANNEALED AT 760°C (1400°F) FOR 100 hours AND AIR COOLED

INTERDENDRITIC PRECIPITATES  
FORMED WHEN LAYERGLAZED

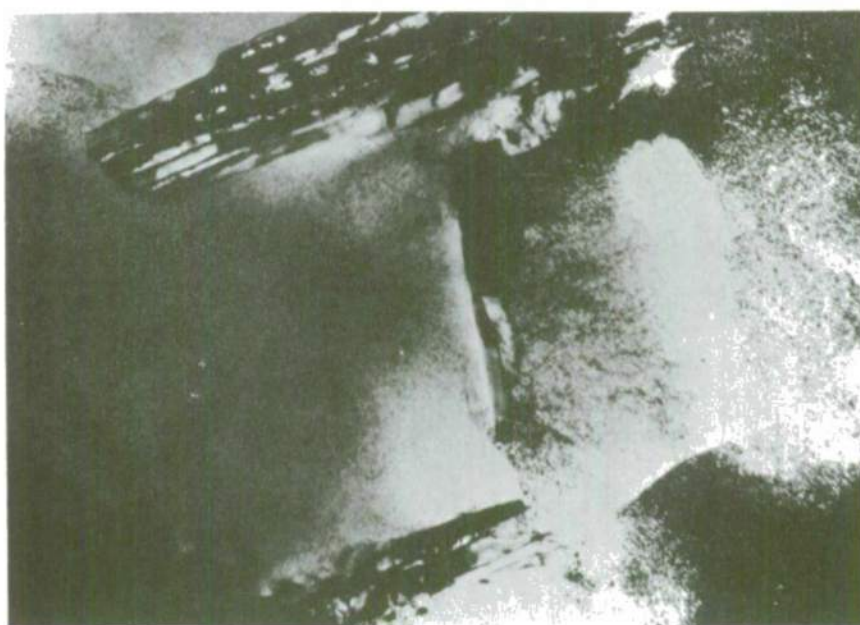


CELLULAR TRANSFORMATION IN DISK 1-8, ALLOY 8-12-3

ANNEALED AT 704 °C (1300 °F) FOR 32 HOURS



(a) NUCLEATION ON INTERDENDRITIC SUBBOUNDARY



(b) ENLARGED VIEW OF REGION IN LEFT-CENTER OF (a)

AREA OF EXTENSIVE CELLULAR PHASE TRANSFORMATION, DISK 1-8, ALLOY 8-12-3

ANNEALED AT 704°C (1300°F) FOR 32 hours

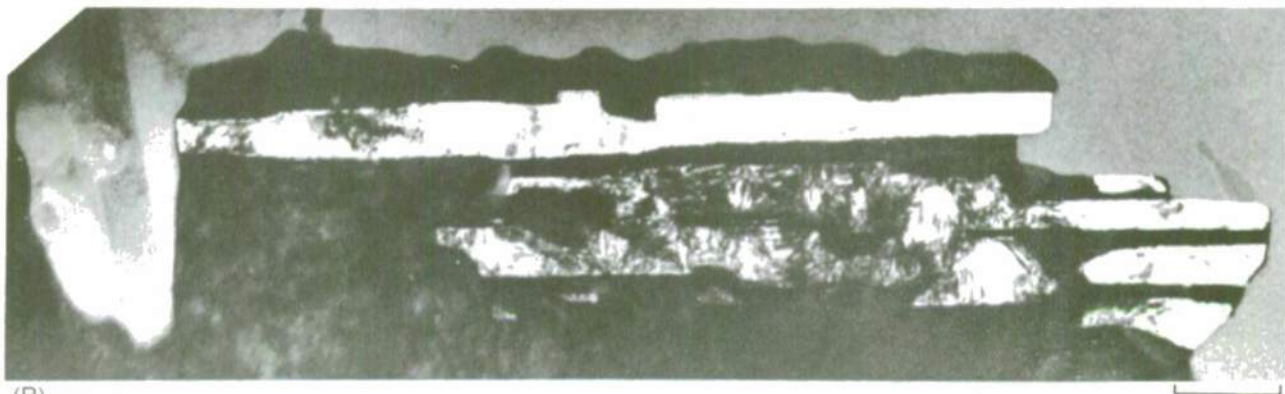


**CELLULAR TRANSFORMATION IN DISK 1-8, ALLOY 8-12-3, ANNEALED AT  
704°C (1300°F) FOR 32 HOURS**

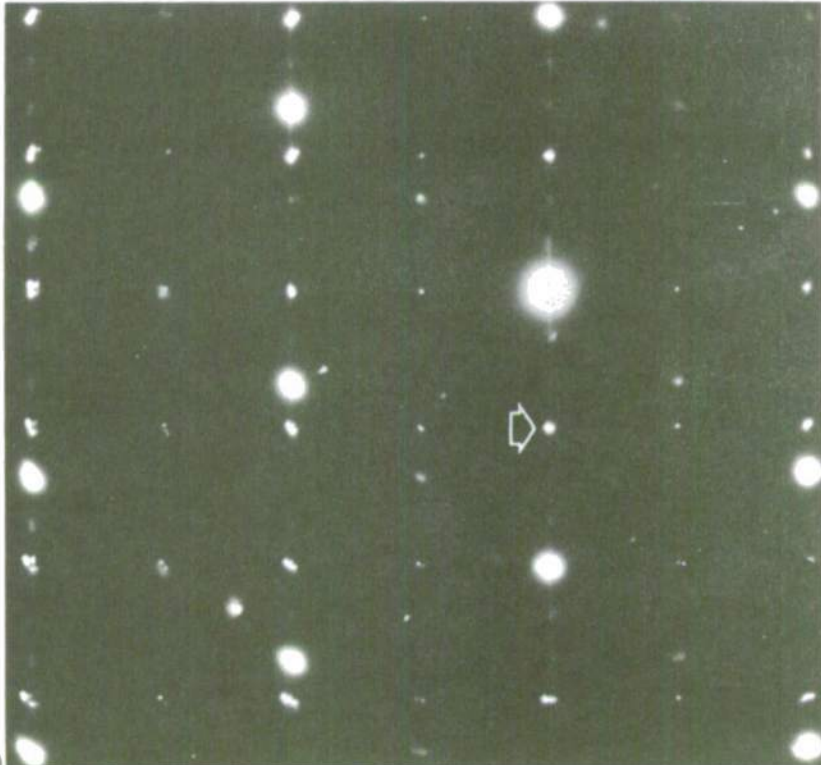
- (A) BRIGHT FIELD OF CELLULAR PACKET AT INTERDENDRITIC SUBBOUNDARY, COMPOSED OF  $\gamma'$  AND ORTHORHOMBIC  $\text{Ni}_3\text{Mo}$ .  
 (B) DARK FIELD OF AREA SHOWN IN (A).  $g = 010$ . ORTHORHOMBIC  $\text{Ni}_3\text{Mo}$   
 (C) SELECTED AREA DIFFRACTION PATTERN FROM CENTER OF (A), 30  $\mu\text{m}$  SELECTED AREA DIFFRACTION APERTURE. ARROW SHOWS SPOT USED TO FORM (B). SUPERIMPOSED PATTERNS. [110] ZONE AXAIS OF  $\gamma'$ . [100] ZONE AXIS OF  $\text{Ni}_3\text{Mo}$ .



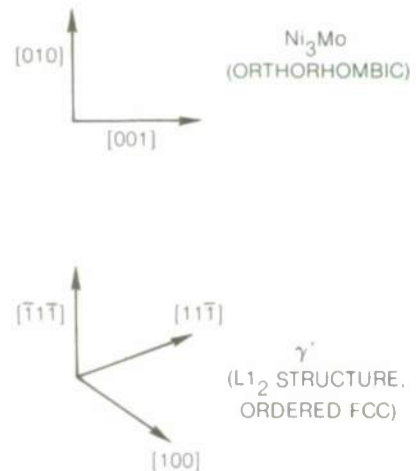
(A)



(B)

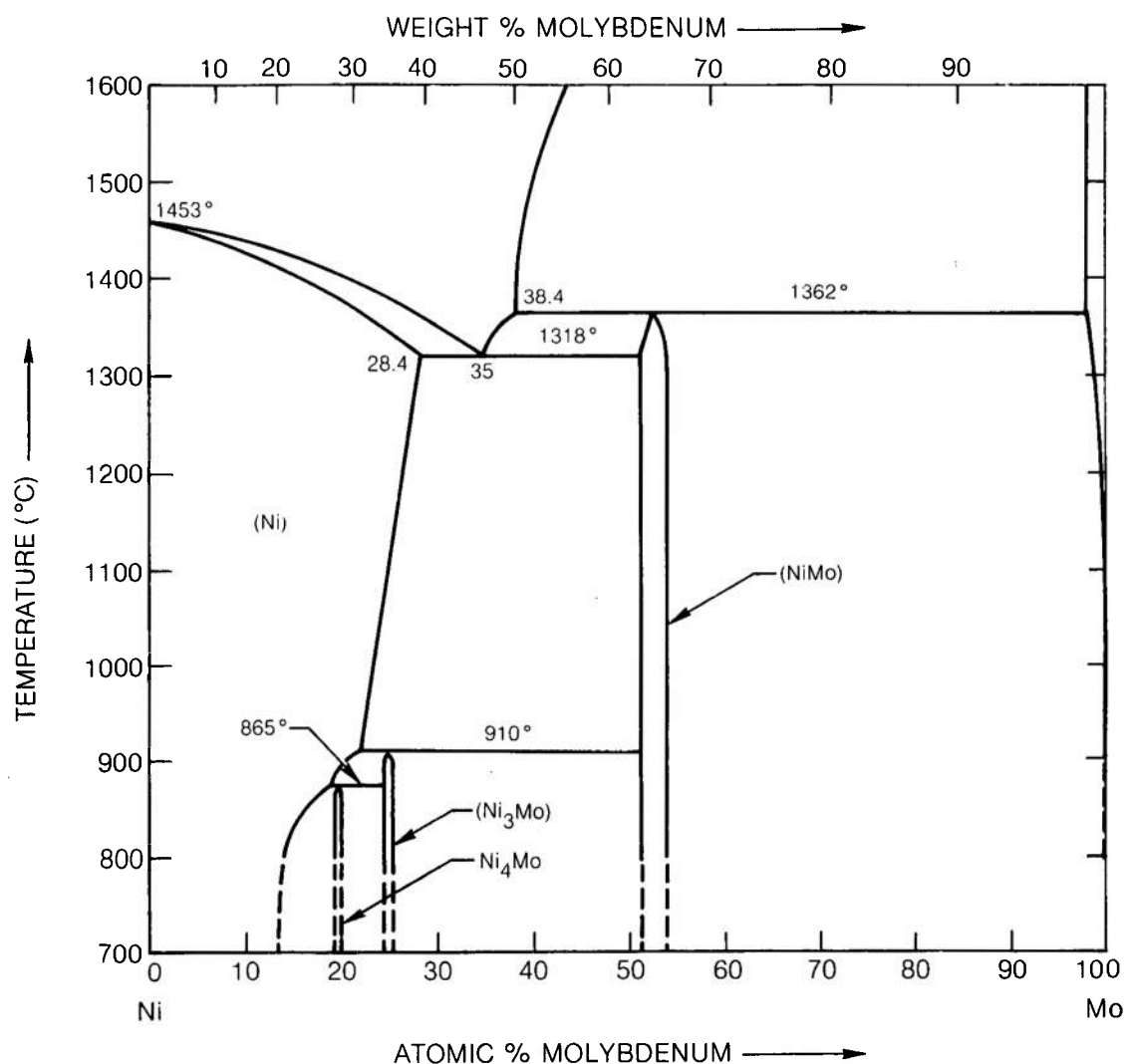
0.2  $\mu\text{m}$ 

(C)



SEE FIG. 76 FOR A MORE COMPLETE  
ANALYSIS OF THIS PATTERN

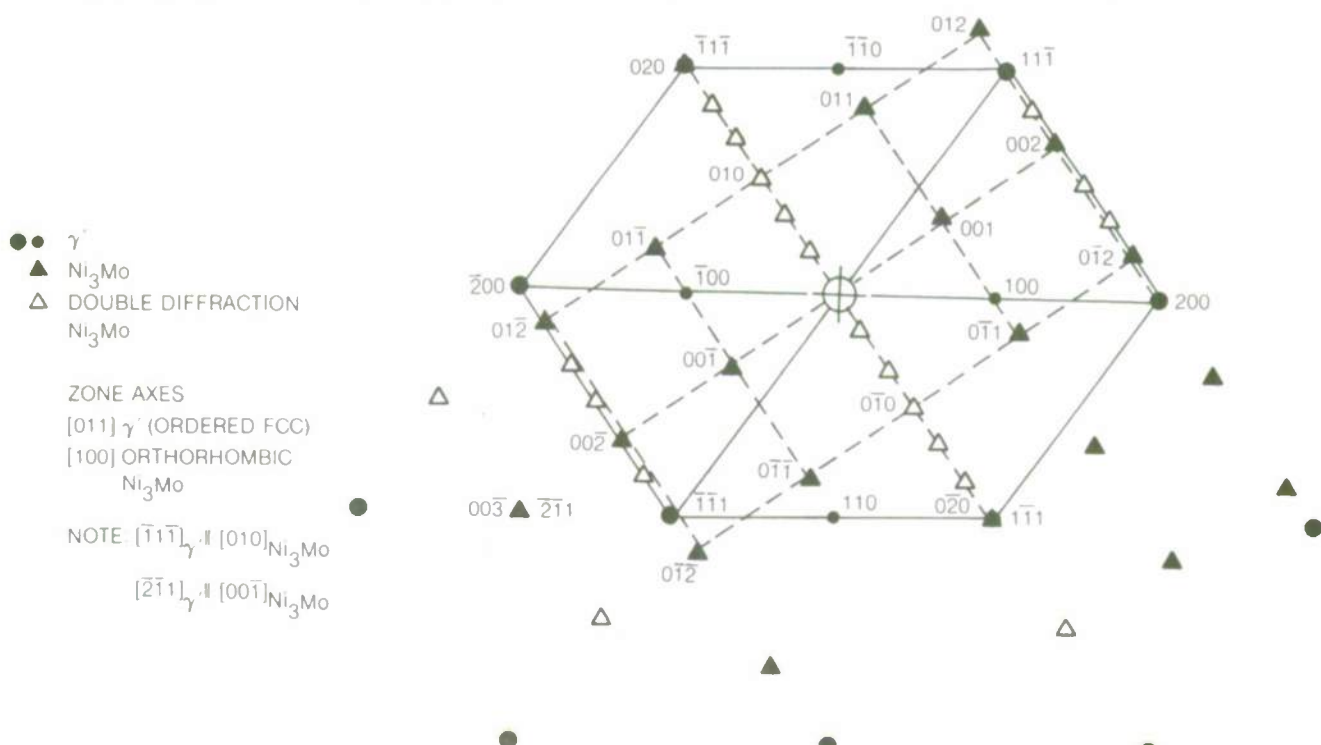
## PARTIAL Ni-Mo PHASE DIAGRAM\*



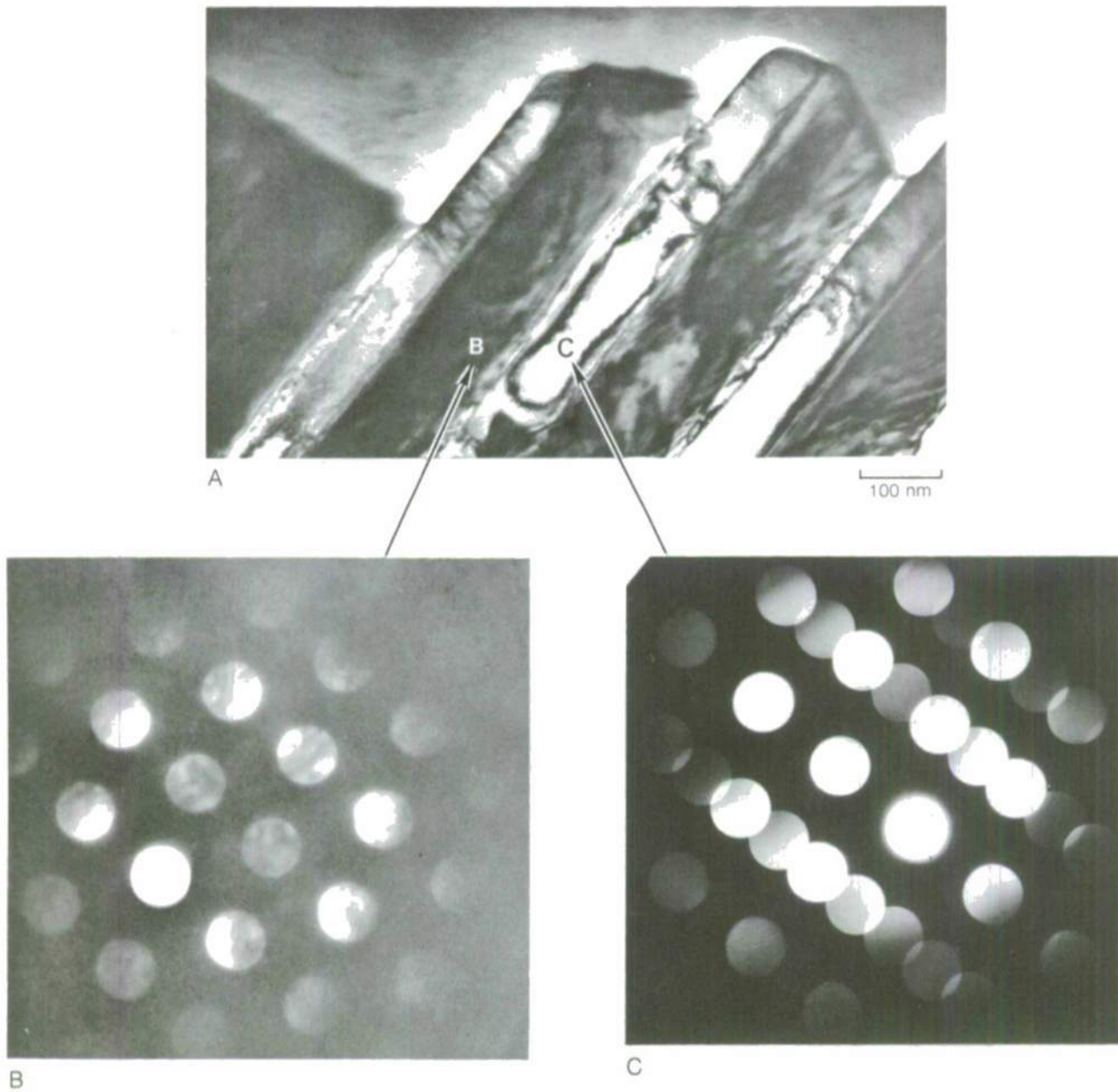
\* AFTER HANSEN (REF. 41) AND ELLIOTT (REF. 42)

**SELECTED AREA DIFFRACTION PATTERN FROM CELLULAR PACKET, DISK 1-8, ALLOY  
8-12-3, ANNEALED AT 704°C (1300°F) FOR 32 HOURS**

AREA GIVING PATTERN IS IN CENTER OF FIG. 74A. 120kV, 30 $\mu$ m SAD APERTURE



## CELLULAR TRANSFORMATION IN DISK 1-8, ALLOY 8-12-3, ANNEALED AT 704°C (1300°F)



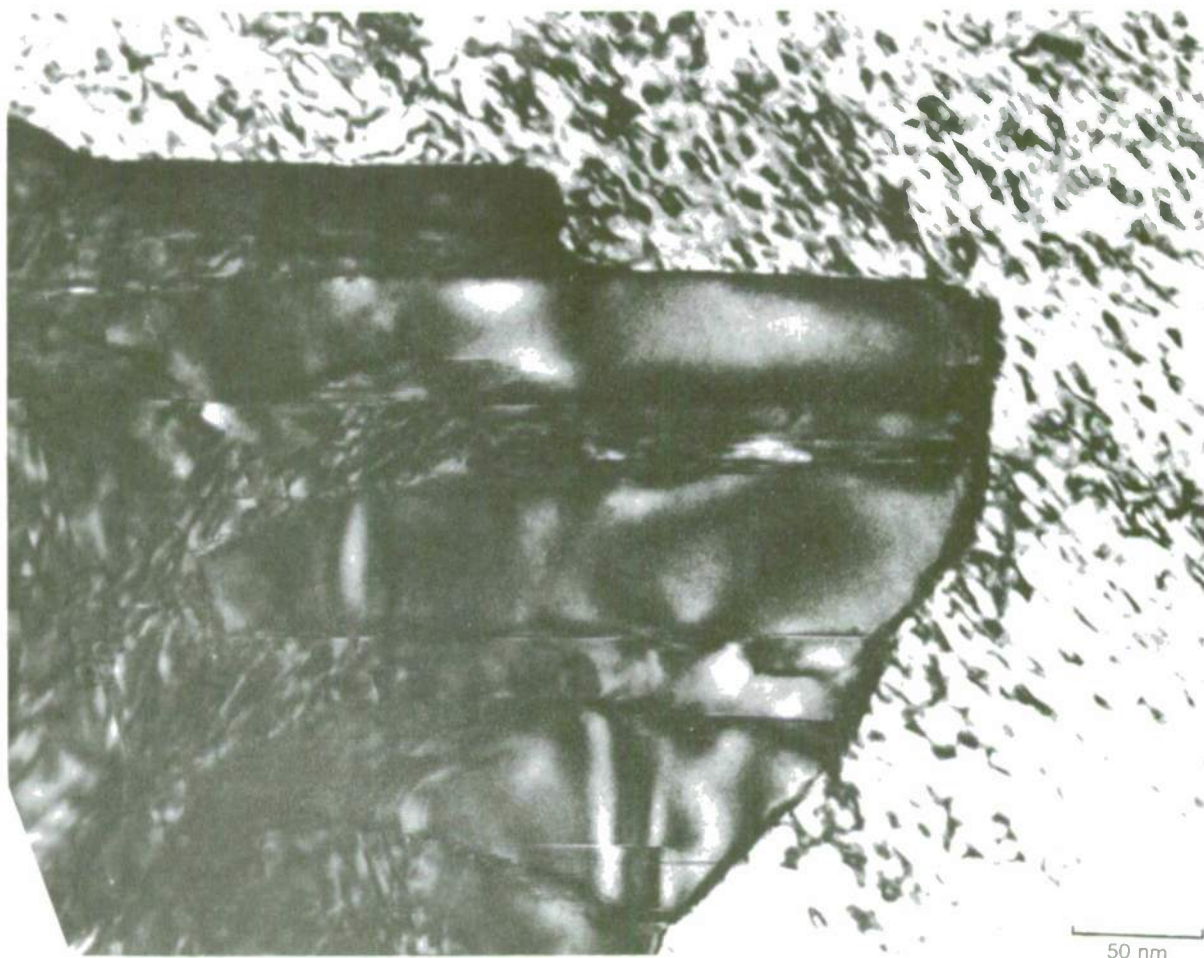
(A) BRIGHT FIELD IMAGE OF CELLULAR PACKET

(B) CONVERGENT BEAM DIFFRACTION PATTERN FROM  $\gamma'$  AT POINT "B". ~ 40 nm SPOT. [011] $\gamma'$  ZONE AXIS. SUPERLATTICE SPOTS ARE TOO FAINT TO APPEAR ON THE PRINT. THE FOIL IS THICKER AT POINT "B" THAN AT POINT "C", DUE TO THE MORE RAPID THINNING OF HIGHER-MOLYBDENUM AREAS.

(C) CONVERGENT BEAM DIFFRACTION PATTERN FROM ORTHORHOMBIC Ni<sub>3</sub>Mo AT POINT "C". ~ 40 nm SPOT. [100] Ni<sub>3</sub>Mo ZONE AXIS. NO DOUBLE DIFFRACTION HAS OCCURRED, SO THE FORBIDDEN REFLECTIONS(010, 030, 013, ETC.) ARE MISSING HERE, WHEREAS IN FIGURE 76 THEY ARE NOT.

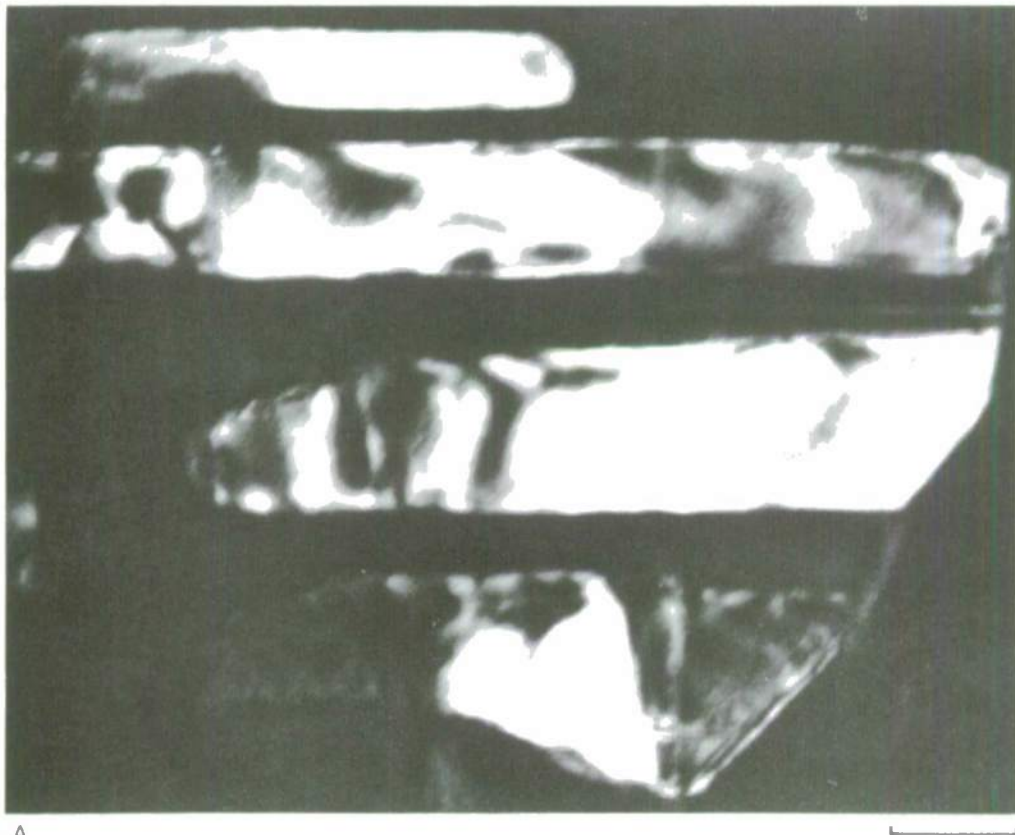
**CELLULAR TRANSFORMATION IN DISK 1-8, ALLOY 8-12-3,  
ANNEALED AT 704°C (1300°F) FOR 32 HOURS**

HIGH MAGNIFICATION BRIGHT FIELD IMAGE OF AREA AT FAR RIGHT OF FIG. 74  
SEE FIGS. 79 AND 80 FOR COMPLIMENTARY DARK FIELD IMAGES



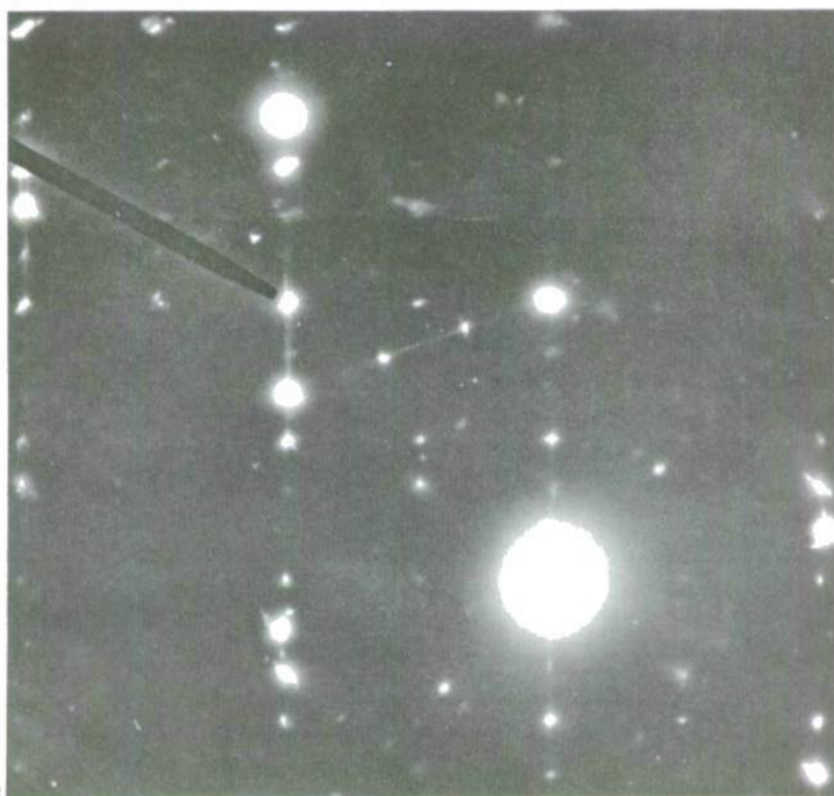
**DARK FIELD IMAGE OF ORTHORHOMBIC Ni<sub>3</sub>Mo COMPONENT,  
CELLULAR TRANSFORMATION, DISK 1-8**

- (A) DARK FIELD,  $g = 02\bar{1}$  Ni<sub>3</sub>Mo, AREA OF FIG. 78  
(B) SELECTED AREA DIFFRACTION PATTERN FROM AREA IN (A). BEAM STOP POINTS TO 02 $\bar{1}$   
Ni<sub>3</sub>Mo REFLECTION USED TO FORM (A).



A

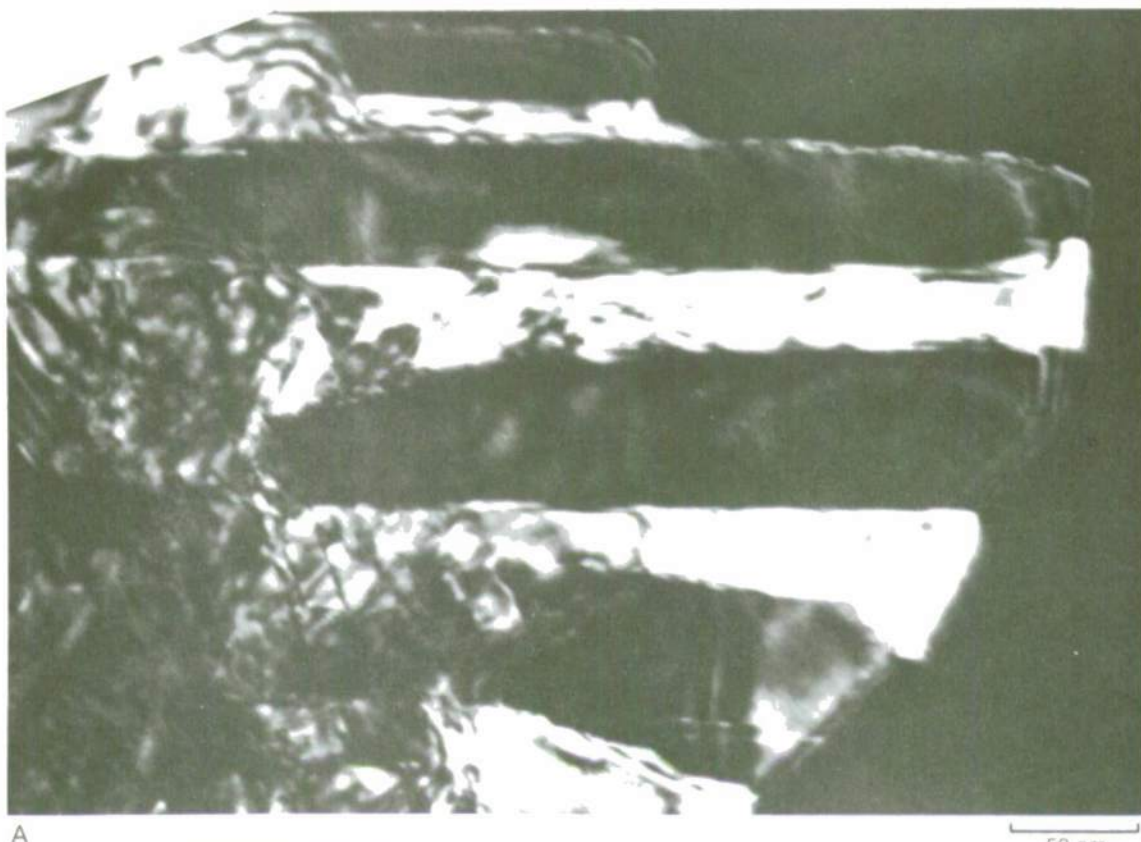
50 nm



B

**DARK FIELD IMAGE OF  $\gamma'$  COMPONENT, CELLULAR TRANSFORMATION, DISK 1-8**

- (A) DARK FIELD.  $g = 200\gamma'$  (ORDERED FCC), AREA OF FIG. 78  
(B) SELECTED AREA DIFFRACTION PATTERN FROM AREA IN (A). ARROW POINTS TO  $200\gamma'$  REFLECTION USED TO FORM (A).



A

50 nm

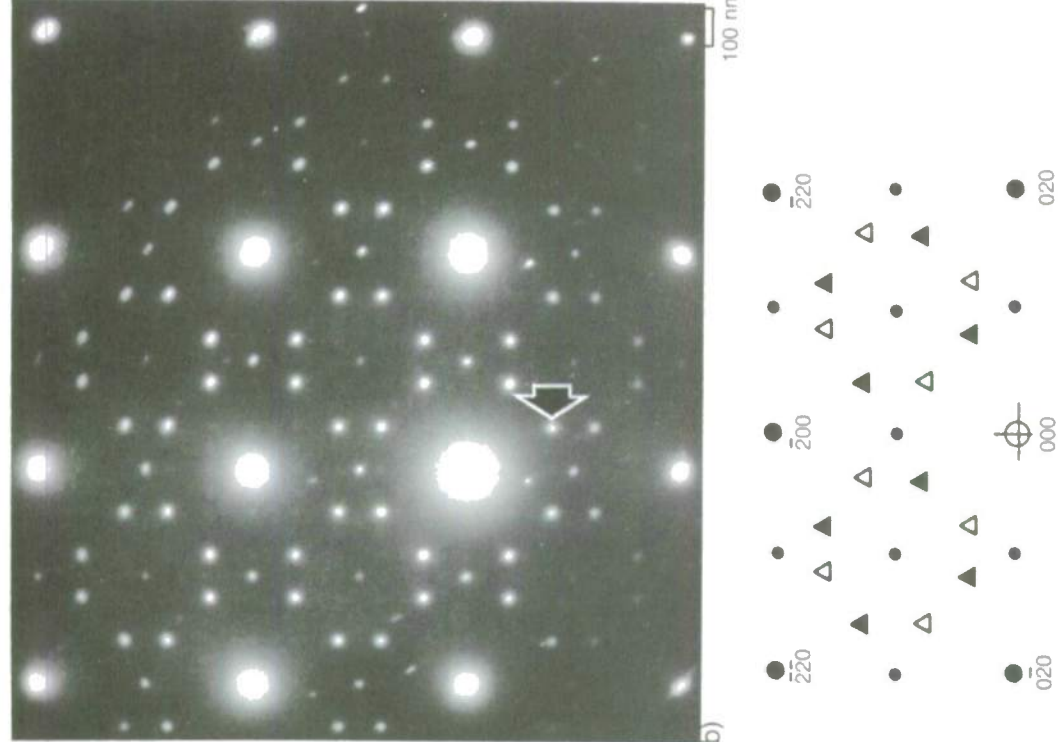


B

PRECIPITATION OF  $\text{Ni}_4\text{Mo}$  IN DISK 1-8, ALLOY 8-12-3,  
ANNEALED AT 704°C (1300°F) FOR 32 HOURS



a) DARK FIELD PHOTOMICROGRAPH OF FINE  $\text{Ni}_4\text{Mo}$  PRECIPITATES  
IN  $\gamma$  NEAR CELLULAR POCKET,  $g = 110 \text{ Ni}_4\text{Mo}$



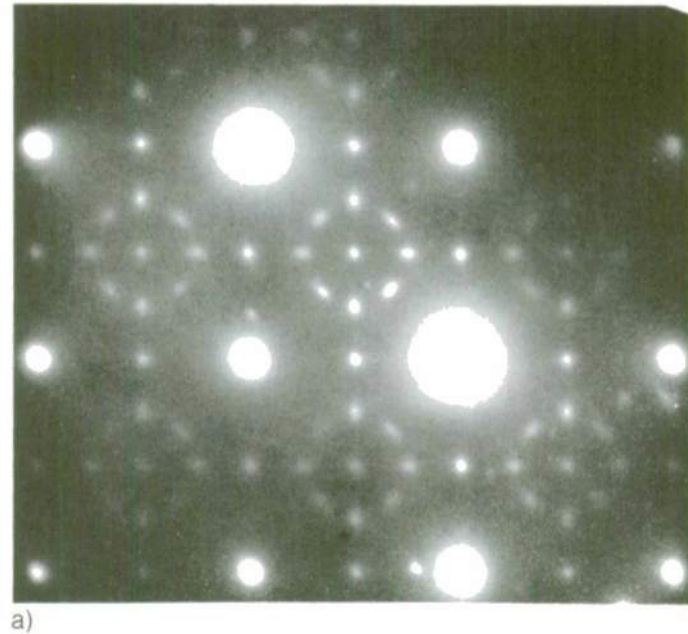
b) SELECTED AREA DIFFRACTION PATTERN FROM AREA OF (a), [001]  
ZONE AXIS, ARROW SHOWS 110 SPOT OF  $\text{Ni}_4\text{Mo}$  USED FOR (a)

c) SCHEMATIC DIAGRAM OF (b) ONLY THE FUNDAMENTAL SPOTS  
ARE INDEXED

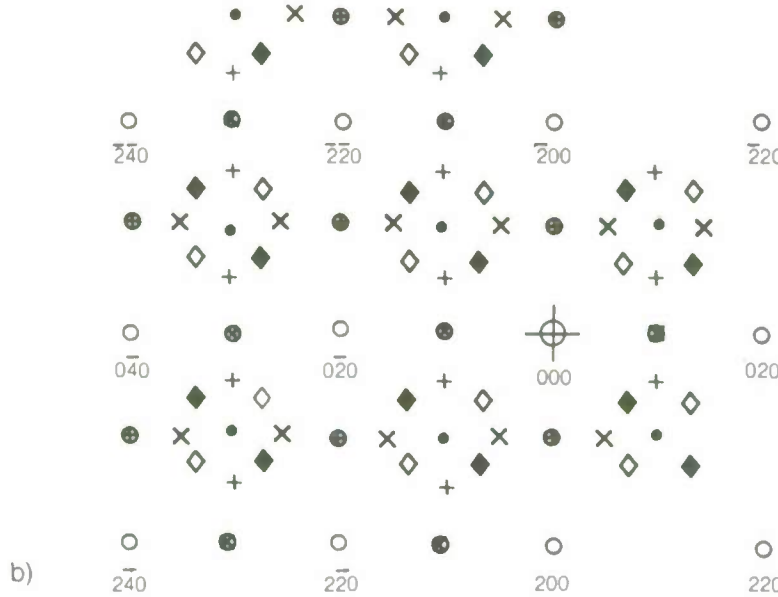
**SELECTED AREA DIFFRACTION PATTERN SHOWING PRECIPITATION OF  $\text{Ni}_2\text{Mo}$  AND  $\text{Ni}_3\text{Mo}$   
IN DISK 1-8, ALLOY 8-12-3, ANNEALED AT 704°C (1300°F) FOR 32 HOURS**

a) [001] ZONE AXIS SADP FROM AREA ADJACENT TO THAT OF FIG. 81a

b) SCHEMATIC DIAGRAM OF (a), ONLY THE FUNDAMENTAL SPOTS ARE INDEXED



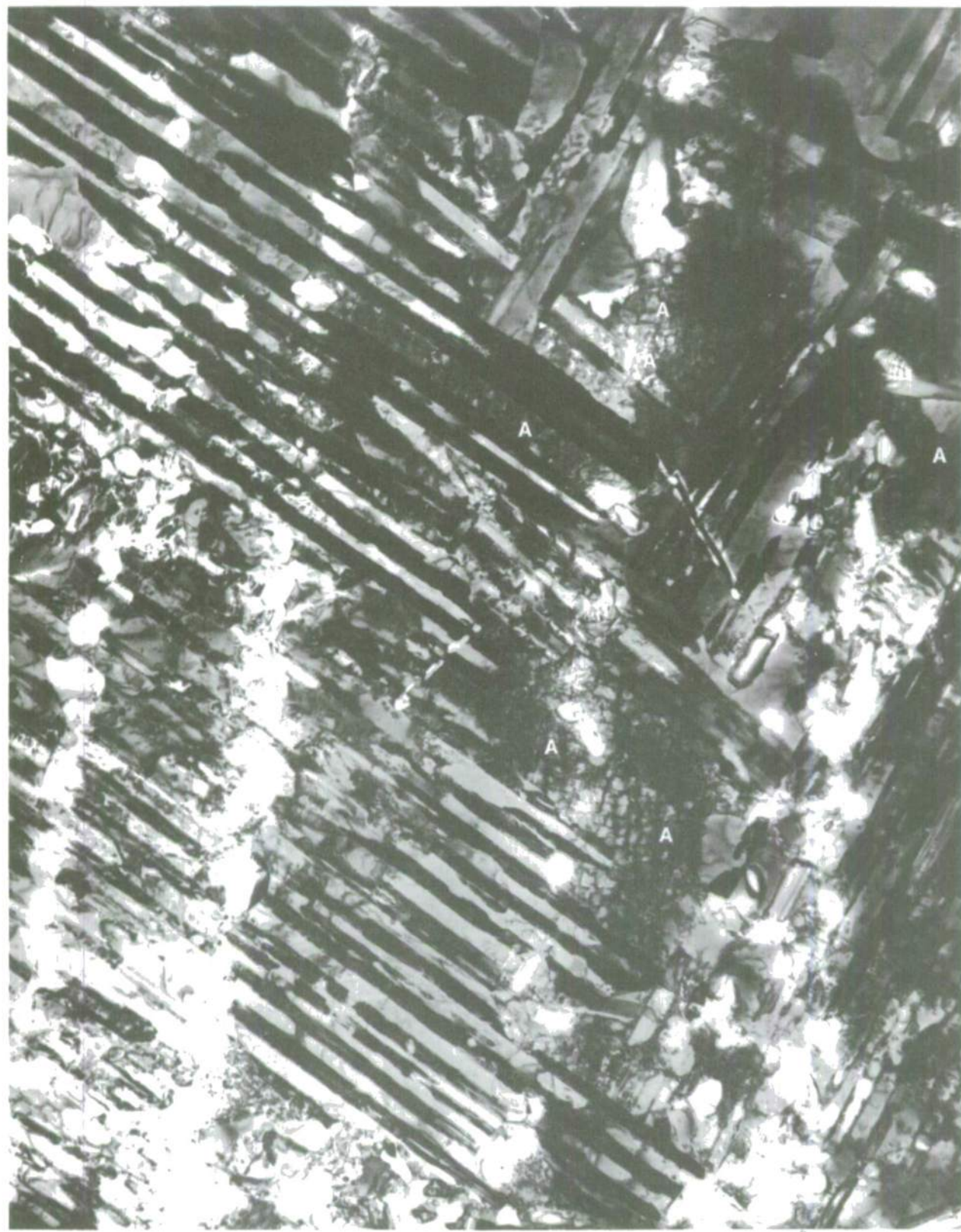
a)



b)

- |   |  |   |   |
|---|--|---|---|
| ○ | $\gamma + \gamma'$   | ● | $\gamma' + \text{THIRD VARIANT, DO}_{22} \text{ STRUCTURE } \text{Ni}_3\text{Mo}$ |
| ● | $\gamma' + \text{FIRST VARIANT, DO}_{22} \text{ STRUCTURE } \text{Ni}_3\text{Mo}$  | × | $\text{THIRD VARIANT, DO}_{22} \text{ STRUCTURE } \text{Ni}_3\text{Mo}$           |
| ● | $\gamma' + \text{SECOND VARIANT, DO}_{22} \text{ STRUCTURE } \text{Ni}_3\text{Mo}$ | ◆ | $\text{FIRST VARIANT, Ni}_2\text{Mo}$   |
| + | $\text{SECOND VARIANT, DO}_{22} \text{ STRUCTURE } \text{Ni}_3\text{Mo}$           | ◊ | $\text{SECOND VARIANT, Ni}_2\text{Mo}$  |

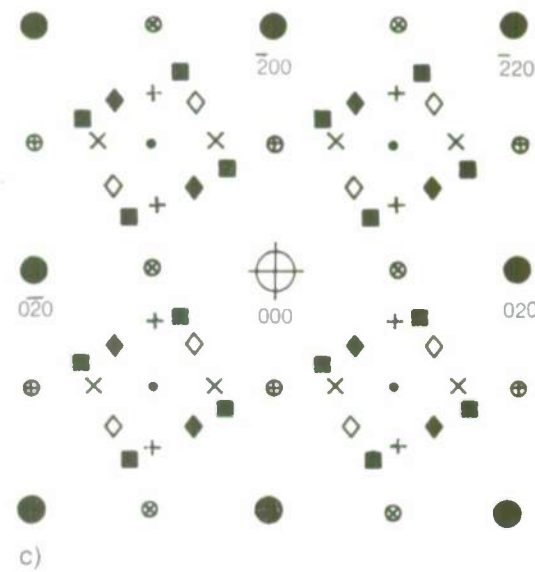
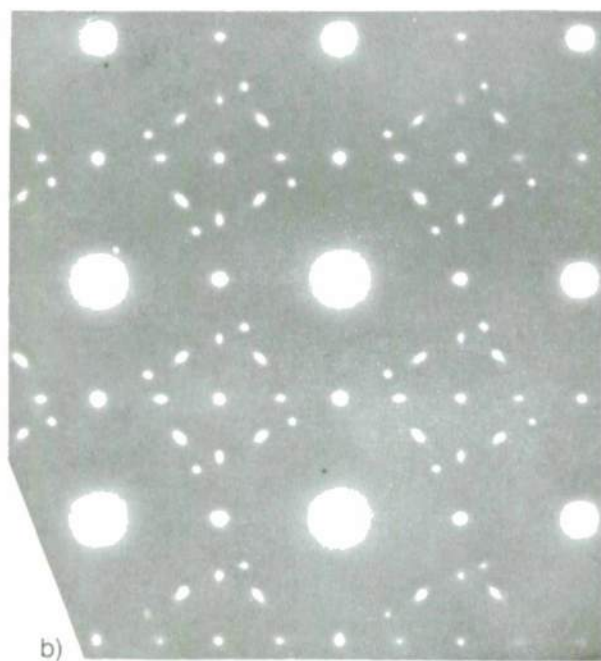
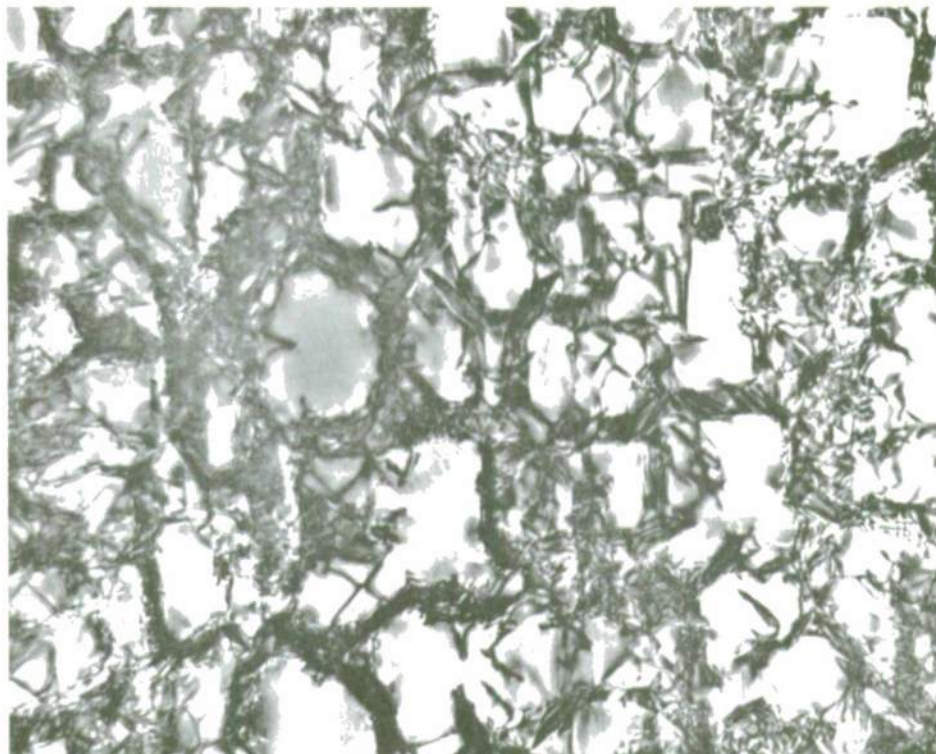
MICROSTRUCTURE OF DISK 9-1, ALLOY 12-15 ANNEALED AT 760°C  
(1400°F) FOR 200 HOURS



LAMELLAR STRUCTURE IS ORTHORHOMBIC  $\text{Ni}_3\text{Mo}$  AND  $\gamma'$   
UNTRANSFORMED AREAS OF  $\gamma + \text{Ni}_x\text{Mo}$  AND CUBOIDAL  $\gamma'$  ARE VISIBLE IN SOME AREAS (A)

1  $\mu\text{m}$

**PRECIPITATION OF  $\text{Ni}_2\text{Mo}$ ,  $\text{Ni}_3\text{Mo}$ , AND  $\text{Ni}_4\text{Mo}$  IN  $\gamma$ , DISK 9-1, ALLOY 12-15, ANNEALED AT 760°C (1400°F) FOR 200 HOURS**



a) BRIGHT FIELD PHOTOMICROGRAPH OF A CUBOIDAL  $\gamma$  SURROUNDED BY  $\gamma + \text{Ni}_x\text{Mo}$  ( $x = 2, 3$ , or 4) (SEE AREA "A", FIG. 83)

b) SELECTED AREA DIFFRACTION PATTERN FROM (a), [001] ZONE AXIS

c) SCHEMATIC DIAGRAM OF (b), ONLY THE FUNDAMENTAL SPOTS ARE INDEXED

- $\gamma + \gamma'$
- $\gamma + \text{FIRST VARIANT, DO}_{22} \text{ STRUCTURE } \text{Ni}_3\text{Mo}$
- ⊕  $\gamma + \text{SECOND VARIANT, DO}_2 \text{ STRUCTURE } \text{Ni}_3\text{Mo}$
- +
- $\gamma + \text{THIRD VARIANT, DO}_{22} \text{ STRUCTURE } \text{Ni}_3\text{Mo}$
- ×
- ◆  $\text{SECOND VARIANT, DO}_{22} \text{ STRUCTURE } \text{Ni}_3\text{Mo}$
- ◊  $\text{FIRST VARIANT, } \text{Ni}_2\text{Mo}$
- ◊  $\text{SECOND VARIANT, } \text{Ni}_2\text{Mo}$
- $\text{Ni}_4\text{Mo}$

CELLULAR TRANSFORMATION IN ALLOY 10-12-3 + 0.1 AT % B,  
ANNEALED AT 1280°C (2336°F) FOR 12 HOURS, THEN 760°C (1400°F) FOR 100 HOURS



**RECRYSTALLIZED GRAIN STRUCTURE OF DISK 1-8, ALLOY 8-12-3  
ANNEALED AT 1240°C (2264°F) FOR 30 MINUTES**



## APPENDIX A

### SUMMARY OF STRESS ANALYSIS CALCULATIONS AND RESULTS (Authored by Brice Cassenti of UTRC)

In order to analyze the stresses incurred in the buildup of a turbine disk, a two dimensional plane stress model was used. It can be shown that the thermal stress experienced by each deposited layer will be greater than the yield stress for the material, and therefore, each deposited layer will plastically yield. Consider the elastic deformation of a deposited layer. The thermal strain is given by

$$\epsilon_{\text{thermal}} = \alpha \Delta T$$

for  $\alpha \sim 10 \times 10^{-6}/^{\circ}\text{F}$  and  $\Delta T \sim -2000^{\circ}\text{F}$

$$\epsilon_{\text{thermal}} = -20 \times 10^{-3}$$

The Total strain can be written as

$$\epsilon_{\text{total}} = \epsilon_{\text{thermal}} + \epsilon_{\text{mechanical}}$$

The relatively thin layer should be almost completely restrained by the bulk material below it and therefore

$$\epsilon_{\text{total}} \approx 0$$

or  $\epsilon_{\text{mechanical}} = -\epsilon_{\text{thermal}} = 20 \times 10^{-3}$

The stress can now be calculated from Hooke's Law as

$$\sigma = E \epsilon_{\text{mechanical}} \text{ if } E \sim 20 \times 10^6 \text{ psi}$$

Then,  $\sigma \sim 400 \text{ ksi}$ , which is well above the yield stress for our materials.

As each layer is deposited on the mandrel, it goes into tension and yields plastically. However, as each subsequent layer is deposited it also goes into tension and thereby applies a compressional hoop stress to the layers beneath it. Plots of the ratio of hoop stress to yield stress versus distance from the center of the mandrel is shown in Figs. A-1 to A-7. Notice that the last layer to be deposited are always at the yield point ( $\sigma_\theta/\sigma_y = 1$ ) and that as more layers are added, the stress on the first layer progresses from a tensile yield point to a compressional yield point.

In order to calculate the radial stress and therefore the pressure exerted on the mandrel, and the melt, one assumes a differential element as in Fig. A-8.

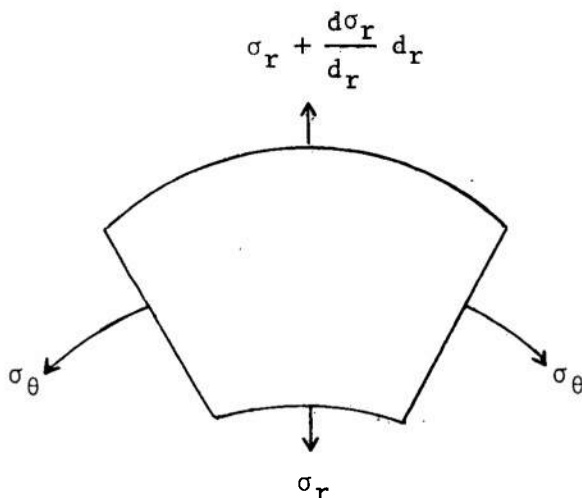


Fig. A-8

At equilibrium the following must be true:  $(\sigma_r + \frac{d\sigma_r}{dr} d\theta)(r+dr)d\theta - \sigma_r(r d\theta) - \sigma_\theta dr d\theta = 0$

$$\text{or } \frac{d\sigma_r}{dr} + \frac{\sigma_r - \sigma_\theta}{r} = 0 \quad (1)$$

Assuming the Tresca yield condition holds at the outside layer

$$\sigma_r - \sigma_\theta = -\sigma_y \quad (2)$$

Substitution of Eq. (2) into Eq. (1) yields

$$\frac{d\sigma_r}{dr} = \frac{\sigma_y}{r} \quad \text{or} \quad \sigma_r = C_1 + \sigma_y \ln r$$

If the outside radius of the outermost layer is denoted as  $r_o$ , then the boundary condition that  $\sigma_r = 0$  at  $r = r_o$  may be imposed.

Therefore,

$$\sigma_r = \sigma_y l_n(r/r_o).$$

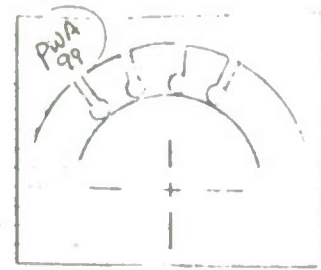
It can clearly be seen that as the number of layers increases, the radial stress approaches the yield stress.

An additional analysis to provide a three dimensional model in which axial stresses may be incorporated has been performed. Using a MARC nonlinear finite element code and analyzing both elastic and plastic material response, a simulation of a deposit of a single layer upon a large mandrel was performed. The result was that high axial tensile stresses, of the order of one-half of the yield stress, were found below and to each side of the deposition. It appears that that after the LAYERGLAZE Process, most conventional superalloys crack because they do not have adequate strain capability to plastically yield to accommodate these high axial stresses. Several alloys developed in this program have shown adequate strain capability.

## **APPENDIX B**

**Model Disk Design  
Spin Arbor Design  
Spin Arbor Assembly/Balance Layout**

## Layered Disk Design



Radius - inches

2.6

2.4

2.2

2.0

1.8

1.6

1.4

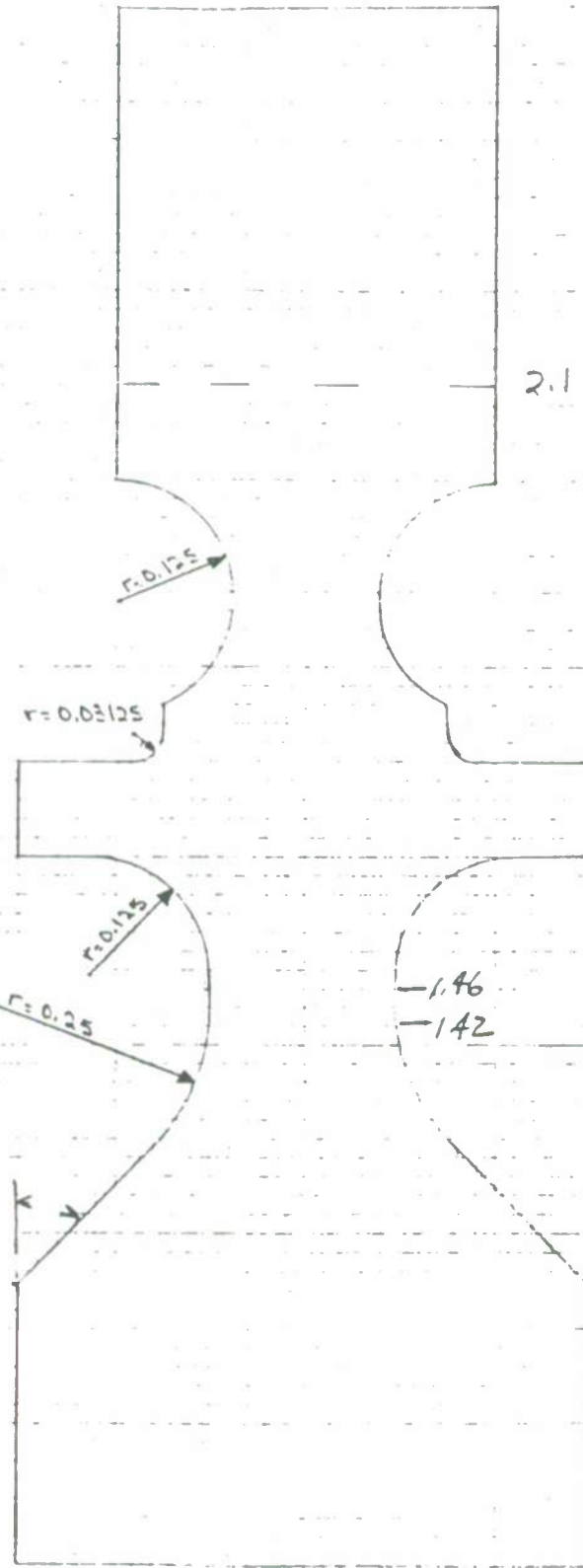
1.2

1.0

1.150

.9

5 x SIZE



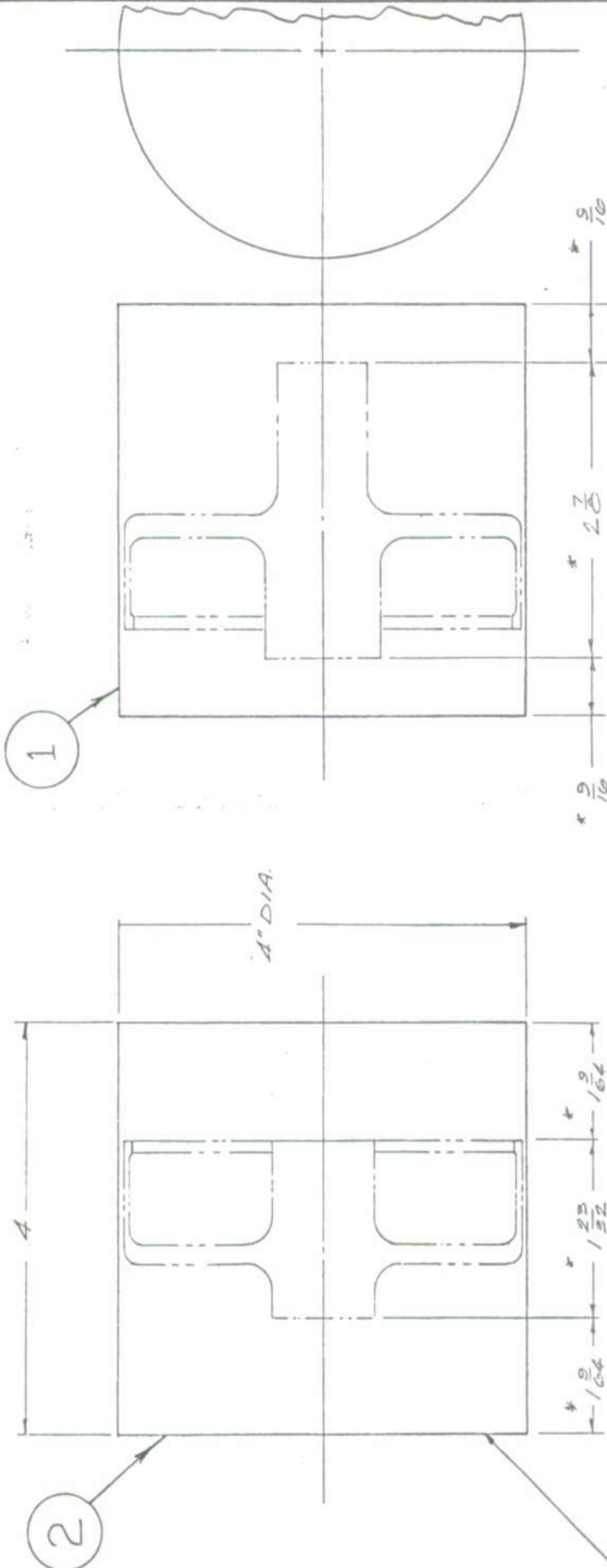
$R_{\text{centr}} = 0.85$  mm 1.29.50

Axial Length - inches

Spin Arbor Design

REF: HALF SCALE  
DETAIL 1/2'  
STK. 43787.

STK 95813



ADVANCE MATER'L LONGS (2) REQ'D  
2" DIA X 4" LONGS  
MATERIAL:

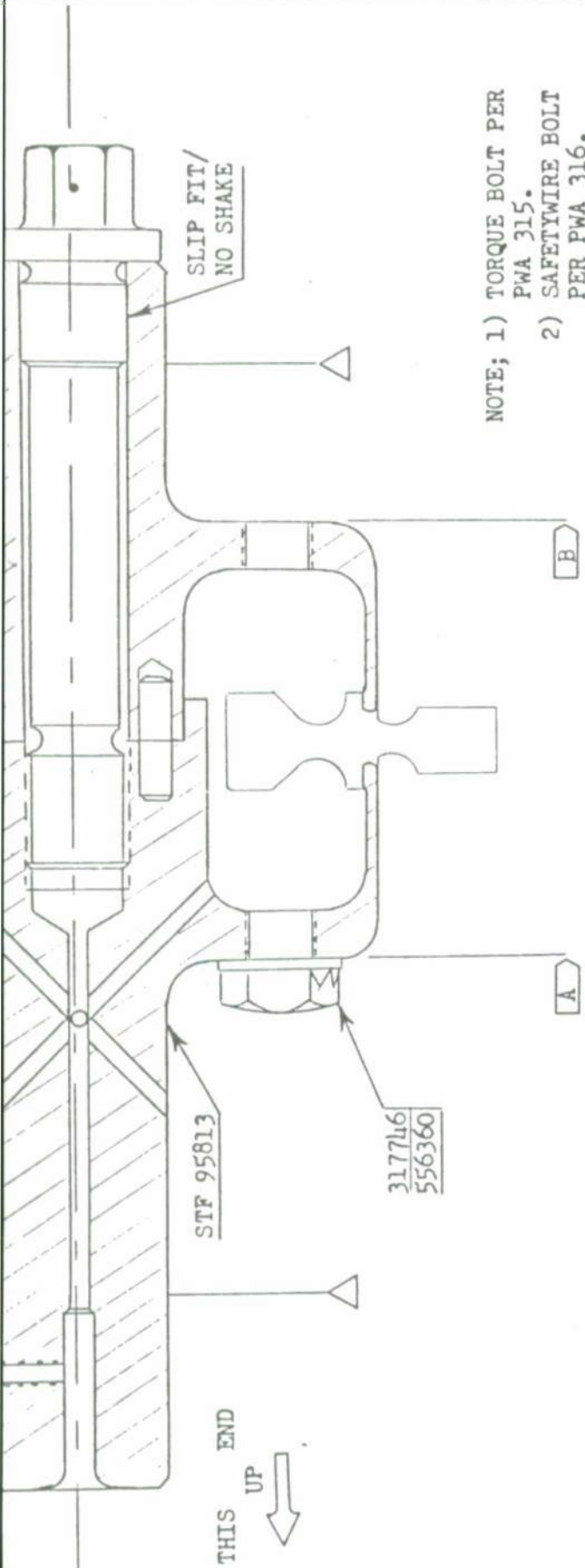
AUA 1003 or  
AUA 1074  
P&W TO FURNISH.  
P&W 300 ALUMINUM  
ALLOY - HOMOGENOUS METALS OR SPECIAL MATERIALS

FULL SCALE

\* REF. DIM. ONLY

MACH	OPEN DISTANCE	MATCH	OPEN DISTANCE	OPEN NO	TOOL NAME
DR. 1/2"	SPIN ARBOR				
1/2"	1/2"	1/2"	1/2"	1/2"	MFG. TOOL DESIGN
DATE 1-13-79	TOOL NO. B				
USE WITH C.P.S.	P&W				

Spin Arbor Assembly/Balance Layout



NOTE; 1) TORQUE BOLT PER

PWA 315.

2) SAFETYWIRE BOLT

PER PWA 316.

3) BALANCE IN PLANES  
 A &  B TO MACHINE  
 LIMITS BY ADDITION  
 OF BALANCE WEIGHTS.

PART NAME: DISK - LAYERGLAZE DESIGN

OPERATION: 1200 F AT 53000 RPM 10 TIMES THEN BURST.

IN THE MM HIGH SPEED RIG.

BAL. MACHINE: GISHOLT 31-S

FULL SCALE B/P AVAIL  YES  NO

ACCOUNT NO. BL6X-51-001-XX

PLANNER: POWELL

DATE: 5-14-80

APPROVED: *T. S. H.*  
 BAL. TOOL LAYOUT

Part &  
 Whitney  
 Aircraft

S.T.L.NO. 209

-TODAY'S DRAWN-

PART NO.	LAYOUT NO.	MODEL NO. I R & D	REVISED DATE	AS RQD QTY
317746				KEYWASHERS
556360				BALANCE WEIGHTS
STF 95813				ARBOR
TOOL NO.				NAME

